GEORG-AUGUST-UNIVERSITÄT GÖTTINGEN

II. Physikalisches Institut

Search for the Associated Production of Charginos and Neutralinos in the Likesign Dimuon Final State with the DØ Experiment

von

Jason Mansour

A search for supersymmetry in the mSUGRA breaking scenario is performed via the associated production of charginos $\tilde{\chi}_1^{\pm}$ and neutralinos $\tilde{\chi}_2^0$ in the likesign dimuon final state. The data used was collected with the DØ experiment in $p\bar{p}$ collisions with $\sqrt{s} = 1.96$ TeV at the Fermilab Tevatron collider. The data, taken in the RunIIb period, corresponds to an integrated luminosity of 4.3 fb^{-1}. The considered final state has a low standard model background and provides sensitivity in the case of nearly degenerate slepton and neutralino masses. Special attention is payed to instrumental backgrounds. The contribution from QCD multijet events and the background due to the mismeasurement of the muon charge is modeled from data. After event selection, 3 events are found in data with a background of $5.4 \pm 4.1(\text{stat}) \pm 0.7(\text{syst})$. Data and background are in good agreement, and as no signs of supersymmetry are seen, limits on the production cross section times branching ratio are set.

Post address:
Friedrich-Hund-Platz 1
37077 Göttingen
Germany

II. Physikalisches Institut
Georg-August-Universität Göttingen

Juni 2010

GEORG-AUGUST-UNIVERSITÄT

GÖTTINGEN

II. Physikalisches Institut

Search for the Associated Production of Charginos and Neutralinos in the Likesign Dimuon Final State with the DØ Experiment

von

Jason Mansour

Dieser Forschungsbericht wurde als Diplomarbeit von der Fakultät für Physik der Georg-August-Universität zu Göttingen angenommen.

Angenommen am:	01. Juni 2010
Referent:	Prof. Arnulf Quadt
Koreferent:	Dr. Carsten Hensel

Contents

1 Introduction

The standard model of particle physics is a remarkably successful theory, which describes three of the four fundamental forces of nature: electromagnetism, the strong and the weak interaction. It has been tested to a very high precision. The prediction of the anomalous magnetic moment of the electron agrees with experimental data in ten significant digits, making this the most accurately verified prediction in physics. Yet, the standard model is known to be incomplete. The now well-established fact that neutrinos have a (albeit very small) mass is not included in the theory. Also, a recent measurement of the dimuon charge asymmetry [1] shows interesting evidence of physics beyond the standard model.

The standard model can be considered an effective low energy approximation of a more fundamental theory, just like classical (Newtonian) mechanics can be obtained in a low-energy limit of special relativity. A promising candidate for such a theory is supersymmetry. Supersymmetry is a symmetry between Bosons and Fermions. For each particle, a new superpartner is introduced, with its spin differing by 1/2. While it might seem a big step to double the number of particles, this is not without precedent. In 1928, Paul Dirac postulated the existence of antimatter to solve the problem of negative energy states in relativistic quantum mechanics. Four years later, the positron was discovered by Carl Anderson, and nowadays, the existence of antiparticles is common knowledge.

With predicted masses of around several hundred GeV, it might be possible to find evidence of supersymmetric particles at the Tevatron or the LHC. The considered likesign dimuon channel provides a very good compromise between a small standard model background on the one hand, and a high sensitivity in previously unprobed regions of the parameter space on the other hand.

This thesis is organized as follows: Chapter 2 gives an overview of the theoretical background, the standard model and supersymmetry. Chapters 3 and 4 describe the DØ experiment and how various physical objects are recognized in the detector. In chapter 5, the analyzed samples, and background Monte Carlo simulations are presented. Instrumental backgrounds from QCD multijet events and charge mismeasurement are discussed in chapter 6. In chapter 7, a progression of cuts is applied to data and background samples, and candidate events are selected. In chapter 8 finally, the results are interpreted, and a short outlook is given.

2 Theory

2.1 The Standard Model

The standard model reflects our current knowledge of the subatomic world. There are two fundamentally different kinds of particles: fermions are the matter particles and have half-integer spin, whereas bosons are the carriers of fundamental forces, and have integer spin. The standard model has twelve fermions, arranged in three generations of increasing mass (Table 2.1). There are three charged leptons, electron (e), muon (μ) and tau (τ), and three neutrinos (ν_e, ν_μ, ν_τ), which have no electric charge and are assumed to be massless. The up-type quarks, up (u), charm (c) and top (t), have an electric charge of $2/3$, while down-type quarks, down (d), strange (s) and bottom (b), have a charge of $-1/3$. Besides electrical charge, quarks carry an additional quantum number, called color, which can take one of three values. For every of the above particles, there exists an antiparticle with the same properties, but opposite charge and helicity.

				Charge	EM	Weak	Strong
Leptons	e	μ	τ	-1	✓	✓	
	ν_e	ν_μ	ν_τ	0		✓	
Quarks	u	c	t	$+2/3$	✓	✓	✓
	d	s	b	$-1/3$	✓	✓	✓
	$\xrightarrow{\text{Generation}}$						

Table 2.1: Fermions of the standard model

Forces are mediated by the exchange of gauge bosons (Table 2.2). For the electromagnetic force, this is the photon. The weak force only acts over very short distances, because its carriers, the W and Z bosons, are massive and short-lived. It plays a role in nuclear decay, and in transitions between fermion generations (flavor-changing currents).

The strong force acts between all colored particles, however its carriers, the gluons, have color charge themselves. This causes the strength of the force to increase rapidly with distance. When differently colored particles are separated, their potential energy becomes eventually large enough to create a new pair of particles from the vacuum, forming hadrons (hadronization). The phenomenon that objects with net color charge (such as single quarks) cannot exist as free particles is called confinement. A notable exception is the top quark, which decays much faster than the hadronization time scale. On the other hand, the strength of the strong force decreases at higher energies or shorter distances. This asymptotic freedom makes it possible to treat partons in hard interactions as free particles, and to use perturbation theory in QCD.

As a gauge theory, the standard model is described in terms of symmetries, which translate into conservation laws. The symmetries of space are given by the Poincaré group, which includes translations, rotations and Lorentz boosts. This leads to the conservation of energy and

Force	Particle	Mass [GeV]
Electromagnetic	γ (photon)	–
Weak	$W^{\pm}$	80.425
	Z^0	91.187
Strong	g (8 gluons)	–

Table 2.2: Gauge bosons of the standard model

momentum, among others. Additionally, an internal gauge symmetry is imposed:

$$\mathrm{SU(3)_C} \times \mathrm{SU(2)_L} \times \mathrm{U(1)_Y}$$

The indicies point to the conserved charges resulting from the symmetries. The group $\mathrm{SU(3)_C}$ gives rise to the color charge. Asymptotic freedom and confinement result from it being a non-Abelian group. $\mathrm{SU(2)_L}$ leads to the conservation of the third isospin component (I_3) for left-handed particles. The conservation of hypercharge Y is caused by $\mathrm{U(3)_Y}$.

The weak and electromagnetic forces are unified in the $\mathrm{SU(2)_L} \times \mathrm{U(3)_Y}$ gauge group [2]. Associated with this group is a triplet field W^i, $i = 1, 2, 3$ and a singlet B. These do not correspond directly to physical particles. Instead, the fields mix quantum-mechanically, to form the $W^{\pm}$ and Z bosons and the photon γ. The contribution of these fields to the physical states is described by a rotation by the Weinberg angle θ_W:

$$\begin{pmatrix} \gamma \\ Z \end{pmatrix} = \begin{pmatrix} \cos\theta_W & \sin\theta_W \\ -\sin\theta_W & \cos\theta_W \end{pmatrix} \begin{pmatrix} B^0 \\ W^0 \end{pmatrix} \tag{2.1}$$

$$W^{\pm} = \frac{1}{\sqrt{2}}(W^1 \pm iW^2) \tag{2.2}$$

The electroweak mixing angle also determines the W and Z boson mass ratio:

$$\cos\theta_W = \frac{M_W}{M_Z} \tag{2.3}$$

To maintain local gauge invariance, gauge bosons may not have explicit mass terms in the Lagrangian. Yet, the W and Z bosons are massive. This is explained by the Higgs mechanism. The Higgs field is a complex doublet, with four degrees of freedom. Three of these are used to couple to $W^{\pm}$ and Z, effectively giving them mass. One degree of freedom remains and manifests itself as a spin-0 particle, the Higgs boson. Masses for fermions are generated by a Yukawa interaction between the Higgs ground state and the fermions. The Higgs boson is the last particle in the standard model which has yet to be found. Its discovery would confirm the Higgs model of electroweak symmetry breaking, and complete the standard model.

2.1.1 Limitations of the Standard Model

Although the standard model has been very successful, both theoretical arguments and experimental evidence point out its limitations. One example is the Higgs fine-tuning problem. The Higgs mass receives corrections from fermion and boson loop diagrams, which diverge quadratically. These terms are proportional to Λ^2, where Λ is the cutoff energy up to which the standard model

is valid. A typical value is the Planck scale, $\Lambda_P = 10^{18}$ GeV. Since the resulting Higgs mass should be of the order of $\mathcal{O}(100\,\text{GeV})$, the bare mass must be fine tuned to cancel the radiative corrections over many orders of magnitude.

The observation of neutrino oscillations also poses a problem for the standard model. Experiments performed to measure the flux of electron neutrinos from the sun [3], count only one third the number of neutrinos expected from solar models. The reason is that neutrinos are emitted as flavor eigenstates (ν_e), not mass eigenstates. The latter propagate as plane waves with a frequency depending on the mass. If neutrinos have different masses, there is interference between the mass eigenstates. In this case, a neutrino created with a certain flavor has a non-zero probability to be measured with a different flavor after propagation. From the observation of neutrino oscillations [4], it can be concluded that they have mass. The upper limit on the neutrino mass is of the order of 2 eV [5].

Further open questions include the origin of the matter/antimatter imbalance in the universe, whether the strong and electroweak forces can be combined into a grand unified theory, and the role of gravity in quantum theory.

2.2 Supersymmetry

Supersymmetry (SUSY) is a theory beyond the standard model, which is a promising candidate to solve some of the problems mentioned in the last section. With supersymmetry, each particle of the standard model gets a superpartner particle with the same quantum numbers, but its spin off by 1/2. Thus the superpartners of fermions are bosons, and vice-versa. However, since these superpartners have not been observed jet, they must be very massive compared to their standard model counterparts. Supersymmetry therefore must be a broken symmetry, if realized in nature.

In this section, observational and theoretical motivation for the introduction of supersymmetry will be presented. Following that is a description of the theory in general, and the minimal supersymmetric standard model (MSSM) in particular. Finally, the particles of interest for this analysis, their production at the Tevatron and their decay modes will be discussed.

2.2.1 Motivation

Supersymmetry provides an elegant solution to the aforementioned Higgs mass problem. Fortunately, the corrections the Higgs mass obtains from virtual particles have the opposite sign for fermions as for bosons. When adding supersymmetry, the terms from standard model particles cancel out naturally with their supersymmetric counterparts. Even in the context of broken supersymmetry, where the cancellations are no longer exact, they do lead to a much smaller total mass correction, and remove the need for excessive fine-tuning.

Another interesting aspect of supersymmetry is that it allows a unification of gauge couplings at high energies. Grand unified theories (GUT) based on the standard model predict that the running coupling constants of the strong, weak, and electromagnetic force almost meet at energies of the GUT scale, which is at around 10^{15} GeV (see Fig. 2.2). However, for the simplicity of the theory, it would be desirable if the running couplings would actually join at the GUT scale. The new particles in supersymmetric extensions of the standard model can appear as virtual particles in Feynman diagrams, and change the energy dependence of the running couplings. It is possible to choose the parameters of the theory such that the couplings unite, making supersymmetry a valuable ingredient for a grand unified theory.

Furthermore, supersymmetry might solve the puzzle of dark matter. From redshift observation of stars, precise measurements of rotational curves of galaxies have been made. It was found

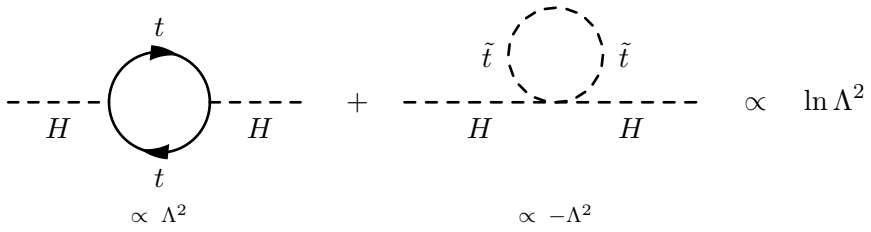

Figure 2.1: Loop level diagrams lead to corrections of the Higgs mass, which are proportional to the cutoff parameter squared ($\propto \Lambda^2$). To have a Higgs mass of $\mathcal{O}(100)$ GeV, these quadratically divergent terms must be canceled by fine-tuning the bare mass. Supersymmetric particles introduce terms of similar magnitude as their standard model counterparts, but with opposite sign. After the cancellation, the total correction is only proportional to $\ln \Lambda^2$.

that the orbital velocity of stars in many galaxies is nearly constant over long distances from the galaxy center. However, given the distribution of visible matter, models predict a more rapidly falling velocity with the radial distance. If the well-tested Newtonian theory of gravitation is to hold on galactic scale, the conclusion is that there is more gravitating mass present in galaxies than visible matter. The missing mass is attributed to dark matter.

There have been many speculations towards the nature of dark matter. "Ordinary" baryonic matter in form of dust, nebulae, or brown dwarfs can be ruled out, since the total amount of baryonic dark matter can be inferred from measurements of the cosmic microwave background, and the result is much less than the total amount of dark matter. Neutrinos make up a part of dark matter, but due to their small mass they are relativistic, and there are cosmological upper bounds on the fraction of relativistic or "hot" dark matter. Supersymmetry could explain the remaining "cold" dark matter (CDM). Under certain circumstances, the lightest supersymmetric particle is stable, and an ideal candidate for CDM (see section 2.2.2 below).

2.2.2 Theory

Formally, supersymmetry can be expressed through the introduction of a superoperator Q, which changes the spin of a state by 1/2:

$$Q\,|S\rangle \propto |S + \tfrac{1}{2}\rangle\,. \tag{2.4}$$

Thus, the superoperator transforms fermions into bosons and vice-versa:

$$\begin{aligned} Q\,|\text{Fermion}\rangle &\propto |\text{Boson}\rangle \\ Q\,|\text{Boson}\rangle &\propto |\text{Fermion}\rangle \end{aligned} \tag{2.5}$$

Since it carries a spin of 1/2, Q is an anti-commuting spinor-valued operator, and satisfies the following anti-commutation relations:

$$\begin{aligned} \{Q_\alpha, Q_\beta\} &= \{\bar{Q}_{\dot{\alpha}}, \bar{Q}_{\dot{\beta}}\} = 0 \\ \{Q_\alpha, P_\mu\} &= \{\bar{Q}_{\dot{\alpha}}, P_\mu\} = 0 \\ \{Q_\alpha, \bar{Q}_{\dot{\beta}}\} &= 2\,\sigma^\mu{}_{\alpha\dot{\beta}}\,P_\mu \end{aligned} \tag{2.6}$$

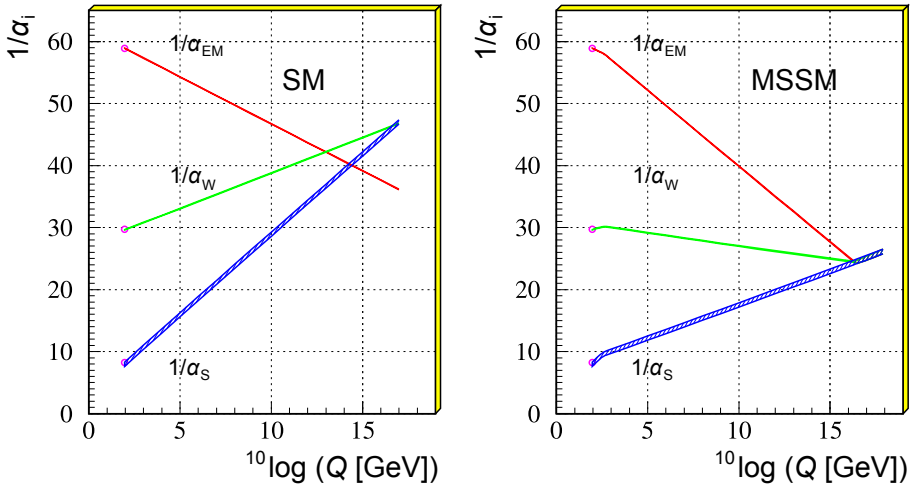

Figure 2.2: Evolution of gauge couplings in the standard model (SM), and in its minimal supersymmetric extension (MSSM). The addition of supersymmetric particles changes the shape of the functions at the TeV scale, and allows for grand unification at the GUT scale. Adapted from [6].

Here, the spinor indices α and β of Q (or $\dot{\alpha}$ and $\dot{\beta}$ of $\bar{Q}$) take the values 1 or 2. P_μ is the translation operator. $\sigma^i, i = 1, 2, 3$ are the Pauli matrices, while $\sigma^0 = \mathbb{1}_2$. The summation convention is applied in the third relation.

R-Parity

R-parity is a multiplicative quantum number, which can be introduced to forbid baryon or lepton number violating processes, such as proton decay. All standard model particles have $R = +1$, while SUSY particles have $R = -1$. A formal definition of R-parity is

$$R = (-1)^{3(B-L)+2S} \,. \tag{2.7}$$

A consequence of R-parity conservation is, that supersymmetric particles are always produced in pairs. Also, the lightest supersymmetric particle cannot decay into lighter standard model particles, making it stable. There are strong cosmological bounds making the existence of undiscovered stable light charged or colored particles unlikely, so the LSP can only interact via gravity or weak interaction. This makes it hard to detect, but also an ideal candidate for cold dark matter. Both R-parity violating (RPV) and R-parity conserving (RPC) models are possible and not experimentally excluded. In this analysis, R-parity is assumed to be conserved.

MSSM

The minimal supersymmetric standard model (MSSM) is the smallest possible extension of the standard model, that is, with the smallest number of new fields. The particle content of the MSSM can be seen in table 2.3. All fermions get spin-0 scalar superpartners, whose names are built from the fermion names by prefixing an “s”. The partners of quarks, leptons and neutrinos are squarks, sleptons, and sneutrinos, respectively. The index R or L on a sfermion indicates the handedness of the standard model partner (since handedness is not defined for spin-0 sfermions

Particle	Symbol	Spin	Particle	Symbol	Spin	
quark	q_R, q_L	1/2	squark	$\tilde{q}_R, \tilde{q}_L$	0	
charged lepton	ℓ_R, ℓ_L	1/2	slepton	$\tilde{\ell}_R, \tilde{\ell}_L$	0	
neutrino	ν_L	1/2	sneutrino	$\tilde{\nu}$	0	
gluon	g	1	gluino	$\tilde{g}$	1/2	
photon	γ	1	photino	$\tilde{\gamma}$	1/2	2 charginos $\tilde{\chi}_i^{\pm}$
W, Z boson	$W^{\pm}, Z$	1	wino, zino	$\tilde{W}^{\pm}, \tilde{Z}$	1/2	4 neutralinos $\tilde{\chi}_i^0$
Higgs	h, H^0	0	Higgsino	$\tilde{h}, \tilde{H}^0$	1/2	
	$h^{\pm}, A$			$\tilde{h}^{\pm}, \tilde{A}$		

Table 2.3: Particles of the minimal supersymmetric standard model (MSSM).

themselves). The partners of the gauge bosons are called gauginos: wino, zino, gluino and photino for W and Z boson, gluon and photon.

In contrast to the standard model, two Higgs doublets are required to cancel gauge anomalies associated with hypercharge, and to give mass to the up and down type quarks. In the two Higgs doublet model (2HDM), there are eight degrees of freedom (two complex doublets $\Rightarrow 2^3 = 8$). Of those, three are consumed in electroweak symmetry breaking, leaving five Higgs bosons: the neutral h and H, the charged H^+ and H^-, and the neutral pseudoscalar A. Each Higgs boson has a Higgsino superpartner.

The gauginos and Higgsinos mentioned above are not the actual physical particles which could be observed, but since they have degenerate quantum numbers, they mix and form different mass eigenstates, similar to the mixing in the electroweak theory, or among neutrinos. The neutral Higgsinos and gauginos mix to neutralinos $\tilde{\chi}_i^0$, where $i = 1, \ldots, 4$. The charged spin-1/2 sparticles mix to charginos $\tilde{\chi}_i^{\pm}$ $(i = 1, 2)$. The charginos and neutralinos are ordered by increasing mass.

The MSSM in its generality has 124 free parameters, and thus not much predictive power. By making some plausible assumptions, it is possible to reduce the number of parameters to 23, of which 18 are the parameters of the standard model, and 5 are new. In the constrained MSSM (cMSSM) it is assumed that the gaugino masses, the masses of the scalar particles, and the trilinear couplings unify at the GUT scale. The five new parameters are:

- Unified gaugino mass: $m_{1/2} = M_i,\ i = 1, 2, 3$
- Unified scalar mass: m_0, where ${m_0}^2 = \tilde{M}^2_{\mathrm{Q,u,d,L,e}}$
- Trilinear coupling: $A_0 = A_u = A_d = A_e$
- Ratio of Higgs vacuum expectation values: $\tan\beta := v_u/v_d$
- Higgs mass parameter: $\mathrm{sign}(\mu)$

The masses of other particles at lower energies can be extrapolated using the renormalization group equations (RGE).

Supersymmetry breaking

While supersymmetry is assumed to be an exact symmetry at high energies, it is spontaneously broken at a lower scale, similar to electroweak symmetry. The breaking occurs in a hidden sector

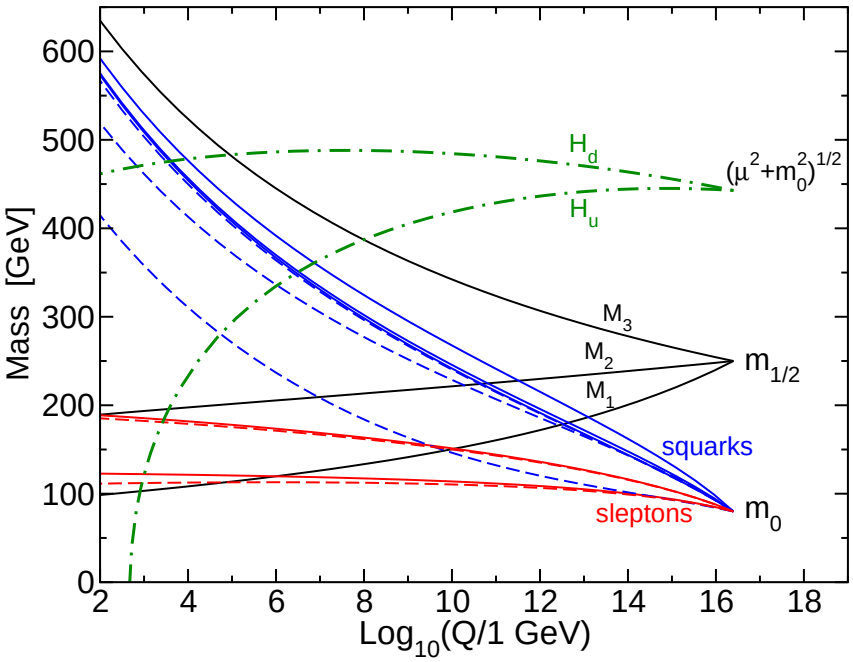

Figure 2.3: Renormalization Group (RG) evolution of the sparticle masses in the constrained MSSM, taken from [7].

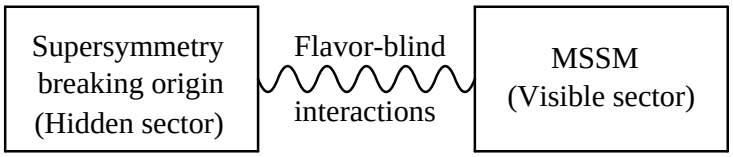

Figure 2.4: Illustration of supersymmetry breaking in a hidden sector, from [7].

of fields which do not interact directly with standard model fields, and affects the visible sector through a messenger field (Fig. 2.4). In the minimal supergravity breaking scenario (mSUGRA), the mediation is done by gravity, since it couples to all massive fields in the hidden and visible sector. Local supersymmetry breaking occurs in the hidden sector at an energy scale $\sqrt{F}$. The mSUGRA model includes a graviton, and its supersymmetric partner, the gravitino, which has a mass of $m_{3/2} = \frac{F}{\sqrt{3}M_P}$, where M_P is the Planck scale. A feature of mSUGRA is that over a large region in the parameter space, the neutralino-2 and chargino-1 masses are approximately twice the mass of the lightest neutralino:

$$2m_{\tilde{\chi}_1^0} \approx m_{\tilde{\chi}_2^0} \approx m_{\tilde{\chi}_1^\pm} .$$

Chargino and Neutralino Production

Supersymmetric particles can be either produced in strong or electroweak interactions. Colored particles like squarks and gluinos are predominantly produced via the strong force, but can also be created via pair production in an electroweak process. Charginos, neutralinos and sleptons are produced via the electroweak interaction. The cross section of supersymmetric particles is comparable to the cross section of their standard model partners at the same Q^2, since the couplings are identical.

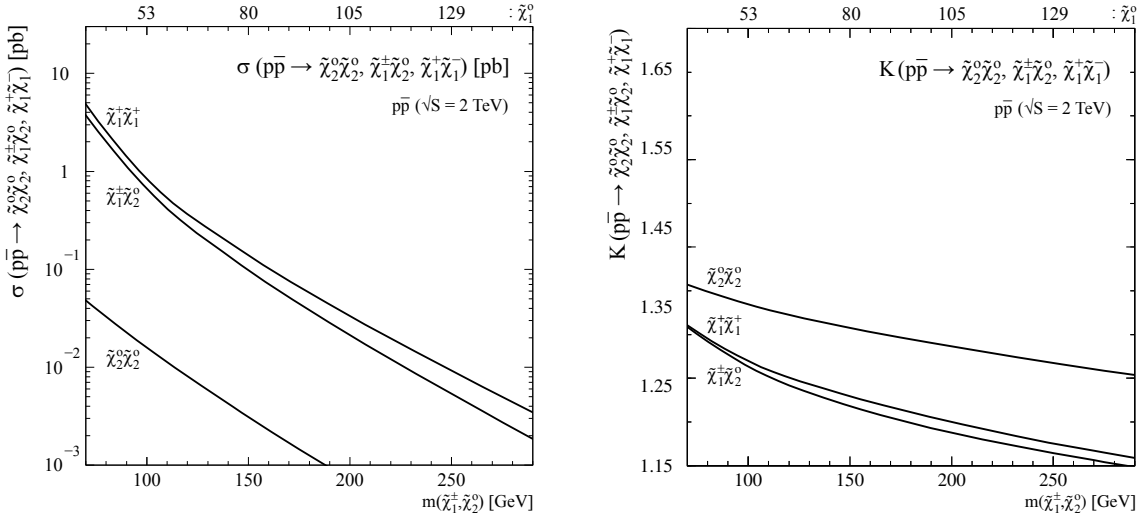

Figure 2.5: Left: Next-to-leading order (NLO) production cross sections of chargino/neutralino pairs at 2 TeV. Right: The K-factor is defined as the ratio between NLO and leading order cross sections. It can give a rough estimate of the accuracy of the NLO cross section, since higher order corrections (NNLO) generally are smaller than the NLO corrections. Adapted from [8].

In this analysis, it will be assumed that R-parity is conserved, and that the lightest supersymmetric particle (LSP) is a neutralino ($\tilde{\chi}_1^0$).

There are two main tree-level processes via which charginos and neutralinos can be produced in this context. Either through the annihilation of a $q\bar{q}$ pair over an intermediate off-shell vector boson (s-channel), or through the exchange of an squark (t-channel). The t-channel production mode however is suppressed because of the large squark mass. The relative contribution of both channels depends on the field makeups of the charginos and neutralinos, and the squark masses. While the squark mainly couples to the gaugino components, the W couples to the gaugino and Higgsino fields.

The processes of interest at the Tevatron are pair production of either charginos ($\tilde{\chi}_1^+, \tilde{\chi}_1^-$) or neutralinos ($\tilde{\chi}_2^0, \tilde{\chi}_2^0$), or the associated production of both ($\tilde{\chi}_1^+, \tilde{\chi}_2^0$). Other channels are either rare, or inseparable from backgrounds. Fig. 2.5 shows the next-to-leading order (NLO) cross sections as a function of the gaugino masses. The pair production of next-to-lightest neutralinos has a cross section which is two orders of magnitude lower than the other production modes. Since the opposite sign chargino production would be difficult to separate from backgrounds, this analysis will focus on the associated production of lightest charginos $\tilde{\chi}_1^+$ and second-lightest neutralinos $\tilde{\chi}_2^0$, as shown in Fig. 2.6.

Decay of charginos and neutralinos

The leptonic decay modes of the lightest chargino and the next-to lightest neutralino are shown in Fig. 2.7 and Fig. 2.8 respectively. The chargino can convert into a neutralino under emission of a W boson, which decays leptonically. This channel is dominant if the mass difference between the $\tilde{\chi}_1^\pm$ and the $\tilde{\chi}_1^0$ is large enough to produce a real W boson. Alternatively, the chargino may decay into a neutrino and a slepton, which itself decays into a chargino and a lepton. This is possible if the slepton is light enough. In both cases, the result is a lepton, a neutrino of the

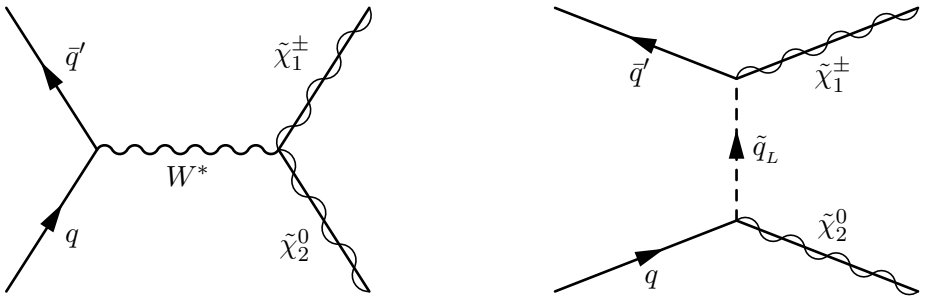

Figure 2.6: Associated production of a chargino $\tilde{\chi}_1^\pm$ with a neutralino $\tilde{\chi}_2^0$. Left: s-channel production via an off-shell W boson. Right: t-channel production via exchange of a slepton $\tilde{q}_L$

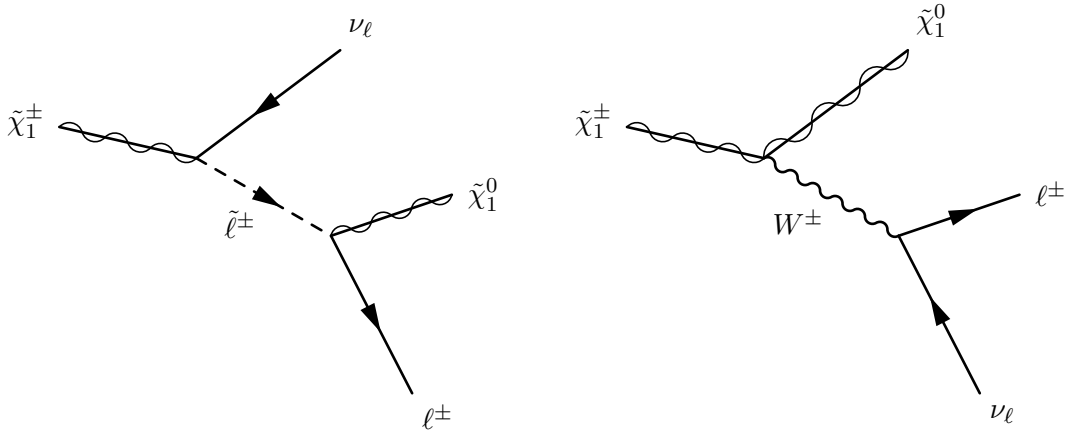

Figure 2.7: Chargino decay modes

same flavor, and an LSP ($\tilde{\chi}_1^0$).

The neutralino-2 can decay into a neutralino-1 under emission of a Z boson, which can then decay into opposite-sign leptons. Again, this channel is dominant if the mass difference between the neutralinos is large enough for a real Z boson. If there is a light enough slepton, the chargino can decay into a lepton and an opposite-signed slepton. The slepton then decays into a lepton of same sign and a neutralino $\tilde{\chi}_1^0$. Both decay modes of the neutralino $\tilde{\chi}_2^0$ lead to an opposite-sign lepton pair and an LSP ($\tilde{\chi}_1^0$).

In general, the branching ratios are determined by the field content of the charginos/neutralinos and the sfermion masses and chirality.

- If the $\tilde{\chi}_2^0$, $\tilde{\chi}_1^\pm$ have a high wino/zino content, the coupling to left-handed fermions and sfermions is favored.
- In case of a high Higgsino content, the coupling to massive particles is enhanced.
- If the chargino and neutralino fields have a high photino content, the decay into electromagnetically charged particles is favored.
- The decay into real gauge bosons/sfermions is dominating if kinematically allowed.

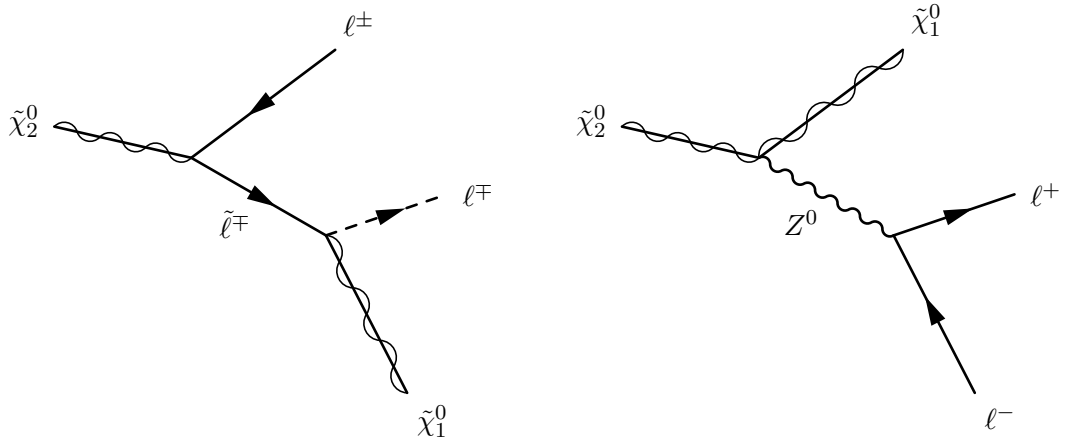

Figure 2.8: Neutralino decay modes

The net result of the $\tilde{\chi}_2^0$ and $\tilde{\chi}_1^{\pm}$ decays is three leptons (of which two have the same flavor and opposite sign), one neutrino, and two LSPs. This trilepton channel has the benefit of a very low standard model background, and has been considered a golden channel for the search for supersymmetry at the Tevatron. A previous analysis has been performed in this channel with 2.3 fb^{-1} [9]. The excluded areas in the $m_0/m_{1/2}$ plane are shown in Fig. 2.9.

The drawback of this approach is a low sensitivity near the line of $m(\tilde{\ell}) \approx m(\tilde{\chi}_2^0)$. When the next-to lightest neutralino decays into a slepton of slightly lower mass and a lepton (Fig. 2.8, left), the lepton will be very soft (low p_T), and might escape detection.

If the selection criteria is loosened to two leptons, this problem does not occur, but this is not feasible due to large backgrounds, especially from $Z \to \ell^+\ell^-$. A compromise is the search for two leptons of same sign (likesign dimuon). Because of the high efficiency and accuracy of muon detection, the scope of this analysis will be the likesign dimuon channel.

Backgrounds of the Likesign Dimuon Channel

Although the likesign dimuon channel is fairly clean, there are various standard model backgrounds that have to be considered. These can be broadly categorized as follows:

- Direct (electroweak) production of likesign dimuons. An example for this is diboson production via $W^+Z \to \mu^+\nu + \mu^+\mu^-$ or $ZZ \to \mu^+\mu^- + \mu^+\mu^-$.
- A standard model process producing one muon, and one muon of same sign from a jet of initial/final state radiation (ISR/FSR) or an underlying event. Examples of this are $Z + \text{jets} \to \mu^+\mu^- + \mu + X$ or $W + \text{jets} \to \mu\nu + \mu + X$.
- An opposite sign dimuon pair, where the charge of one muon gets mismeasured. The single largest contribution to this charge flip background comes from $Z \to \mu\mu$.
- QCD multijet. Events with multiple jets from ISR/FSR, the underlying event, or proton remnants. The jets can radiate muons, which might not be recognized as part of the jet, and contribute to the background.

All backgrounds are simulated with Monte Carlo, except for the QCD multijet background, which is determined from data.

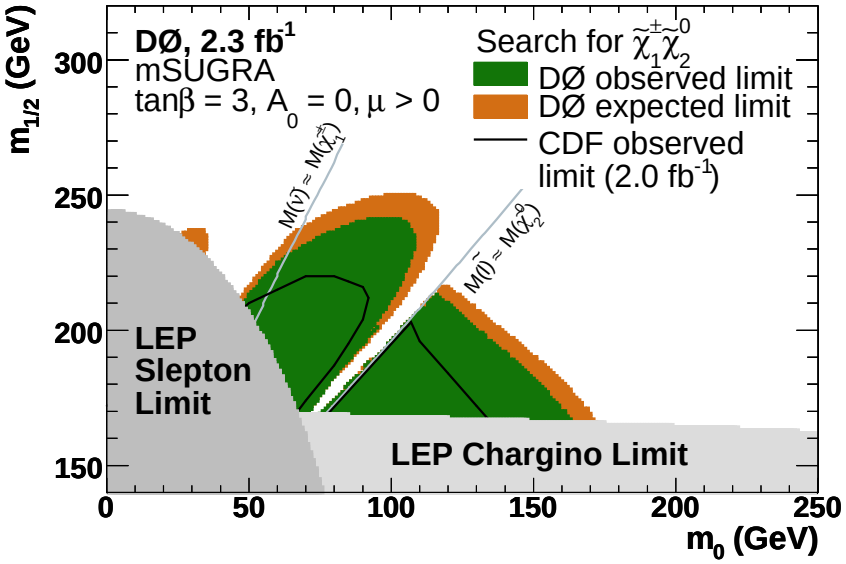

Figure 2.9: Region of the $m_0/m_{1/2}$ plane excluded by the DØ trilepton search, LEP searches for sleptons and charginos, and CDF. From [9].

3 Experimental Setup

The Tevatron is a proton-antiproton collider located at the Fermi National Accelerator Laboratory, in the vicinity of Chicago, Illinois, USA. It has a circumference of 6 km and features two general purpose detectors, CDF (Collider Detector Facility) and DØ. Completed in 1992, the Tevatron originally had a center-of-mass-energy of 1.8 TeV. During its first run (Run I), which continued until 1996, a total integrated Luminosity of $\int \mathcal{L}\, dt = 125$ pb^{-1} has been delivered. An important achievement of this period was the discovery of the top quark in 1995.

After Run I, the Tevatron and its detectors have undergone a major upgrade to 1.96 TeV and higher luminosity, and resumed operations in 2001. Since then, 8 fb^{-1} of integrated luminosity have been recorded per experiment.

In the following, the Tevatron and its pre-accelerators will be described, followed by a discussion of the DØ detector.

3.1 The Tevatron Accelerator Complex

The energy of the protons and antiprotons is increased in several stages before they reach 960 GeV and are brought to collision [11]. The process begins with H^- ions, which are accelerated by a Cockroft-Walton generator to 750 keV (3.7% of light speed). A linear accelerator (LINAC) raises their energy to 400 MeV (71% of light speed), in which the negative ions pass a thin graphite window and get their electrons stripped off. This makes it possible to use the same voltage difference twice. After the LINAC, the protons are fed into a synchrotron, the booster, and are brought to 8 GeV.

The next step is the main injector, where the protons reach 150 GeV, and are grouped into bunches. The time between the passing of two bunches is 396 ns. Twelve such bunches are combined into one superbunch. The whole beam structure consists of three superbunches, separated by 2 µs each. The timings are chosen such that the length of one full cycle equals the circumference of the Tevatron.

The protons are now ready to be injected into the Tevatron. To create antiprotons, a beam from the main injector is transferred to the antiproton source. There, it passes the debuncher, before it hits a nickel-copper-target. Every 2–4 seconds, 7×10^{12} protons of 120 GeV collide with the target, and produce in the order of 10^8 8 GeV antiprotons [12]. The antiprotons are separated from the beam and focused by a lithium solenoid coil (∼650 kA). Then they are "stacked" in the accumulator, until enough are collected ($\sim 10^{12}$). The antiproton beam is then transferred into the main injector, where it circulates in the opposite direction of the protons.

When enough protons and antiprotons are available, they are injected bunchwise into the Tevatron. Both beams share the same beampipe (possible due to their opposite charge), and follow a double-helix orbit around the center of the pipe. The beams are accelerated to the final 960 GeV, after which they are brought to collision in six interaction points distributed evenly around the ring (A0-F0). In a last step, the beams are collimated, and the beam halo is reduced, to maximize luminosity and minimize undesired stray interactions.

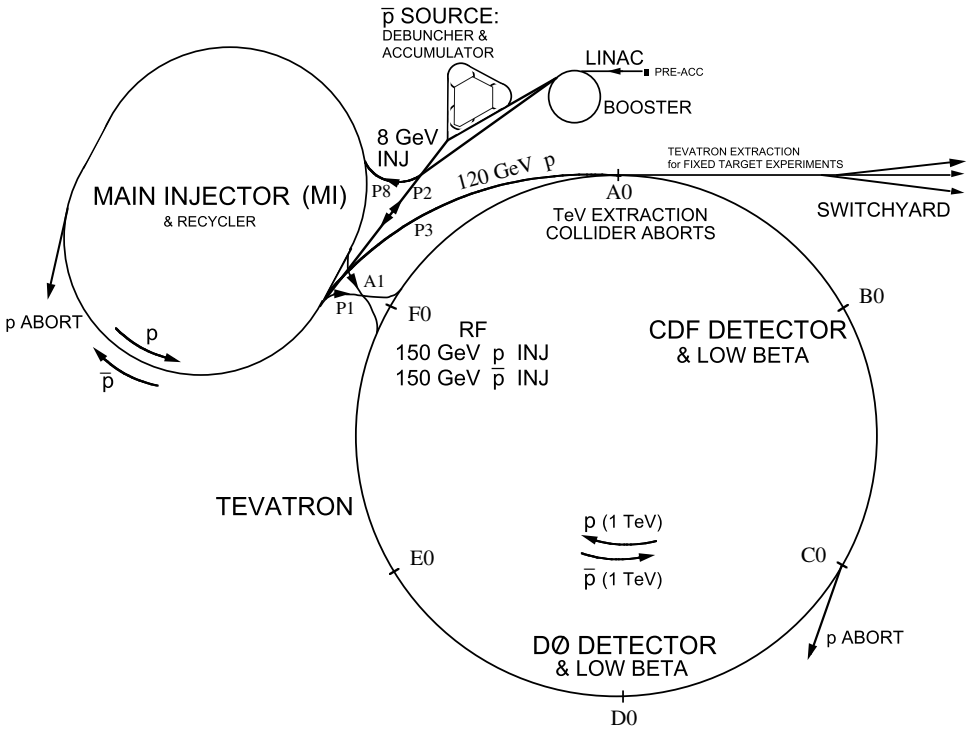

Figure 3.1: Schematic of the Tevatron and its pre-accelerators (from [10]). The acceleration of protons begins with a Cockroft-Walton generator (top center, "PRE-ACC"). The next stages are the LINAC, booster, main injector and finally the Tevatron. To create antiprotons, a proton beam is fed from the main injector into the $\bar{p}$ source. The antiprotons are then also accelerated in the main injector and in the Tevatron. Detectors are at the interaction points B0 (CDF) and D0 (DØ), and protons can be extracted at A0 for fixed target experiments.

3.2 The DØ Detector

The DØ detector, located around the interaction point of the same name, is a general purpose detector, suited for many different kinds of physics analyses. It is nearly hermetic, meaning that it has an almost 4π solid angle coverage. An overview is shown in Fig. 3.2. Its components are from the inside to the outside:

- A tracking system, consisting of the Silicon Microstrip Tracker (SMT) and the Central Fiber Tracker (CFT)
- A 2 Tesla solenoid magnet to curve the trajectories in the tracker
- The central and forward preshower detectors
- A liquid argon based sampling calorimeter, which is split in central (CC) and endcap (EC) regions.
- A 2 Tesla toroid magnet
- The muon system, containing trigger chambers, and track chambers.

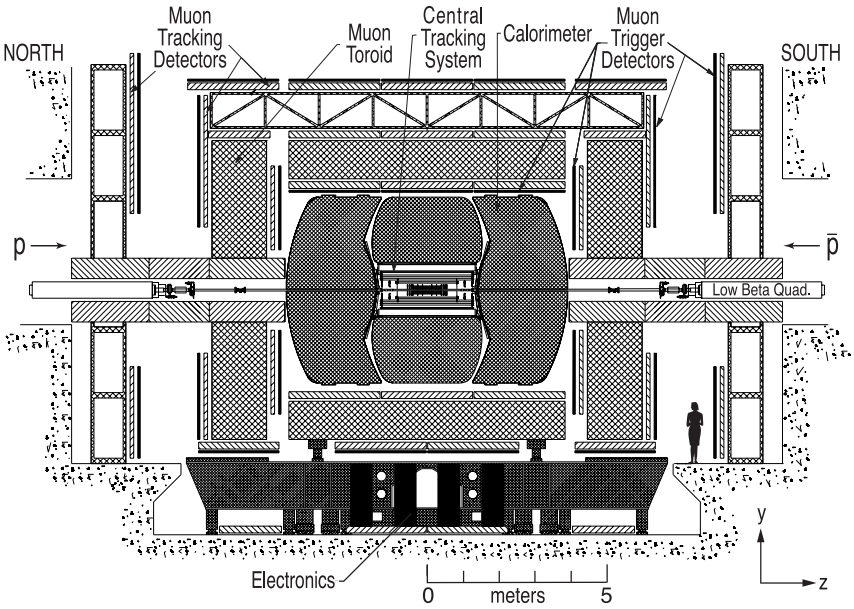

Figure 3.2: Cross sectional schematic of the Run II DØ detector, from [13].

The DØ experiment uses a right-handed coordinate system, with the z axis pointing in the direction of the proton beam, the y axis pointing upwards, and the x axis away from the center of the Tevatron. The origin is in the center of the detector. In the following, also polar coordinates will be used, where r is the radial distance to the center of the beampipe, φ is the azimuthal angle, and θ is the inclination. The relations between the coordinate systems are given by

$$r = \sqrt{x^2 + y^2} \qquad \varphi = \arctan \frac{y}{x} \qquad \theta = \arctan \frac{r}{z}\,, \tag{3.1}$$

where $\varphi, \theta \in [0, 2\pi[$. Instead of the inclination θ, it is convenient to use the pseudorapidity η, defined by

$$\eta = -\ln \tan \frac{\theta}{2}\,. \tag{3.2}$$

In the limit of low particle masses or high energies, $m/E \to 0$, the pseudorapidity approximates the rapidity in z direction, ϑ_z, since

$$\eta = \frac{1}{2} \ln \frac{p + p_z}{p - p_z} \qquad \text{and} \qquad \vartheta_z = \frac{1}{2} \ln \frac{E/c + p_z}{E/c - p_z}\,. \tag{3.3}$$

Here, p is the momentum, and E is the total energy of the particle. Differences in rapidity $\Delta\vartheta_z$, and rapidity distributions $\frac{dN}{d\vartheta_z}$, are invariant under boosts along the z axis. In inclusive QCD processes, rapidity distributions are flat (rapidity plateau), except for acceptance effects. Since same rapidity intervals receive the same rates, but rapidity lines grow closer in the forward region (Fig. 3.8), the detector has a finer granularity there. The position of particles can be given either in physics coordinates, relative to the primary vertex, or detector coordinates, relative to the detector center. An example for detector coordinates is the "detector eta" η_{det}, which is useful when discussing detector coverage.

3.2.1 Tracking System

The innermost component of the detector is the tracker. Its purpose is the measurement of charged particle tracks and vertices. The tracking system is contained in a 2 Tesla magnetic

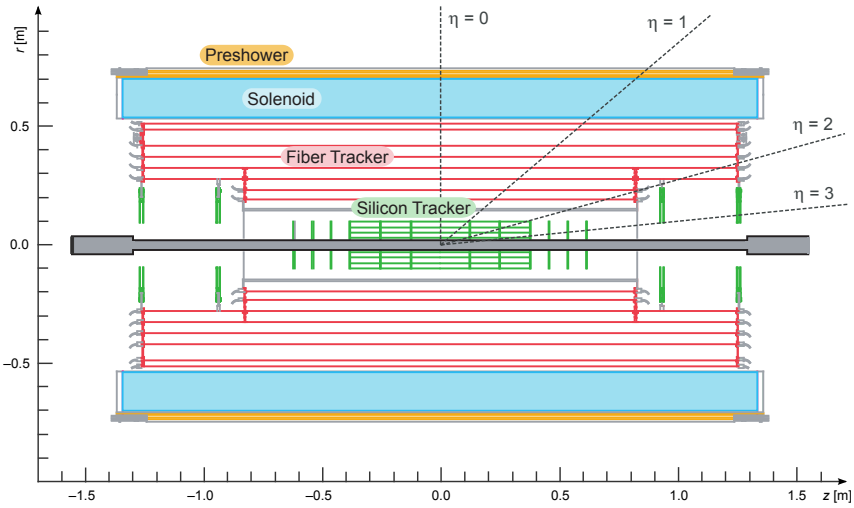

Figure 3.3: Schematic of the inner detector parts. From inside out: Silicon Microstrip Tracker (SMT), Central Fiber Tracker (CFT), Solenoid, Central Preshower Detector (CPS)

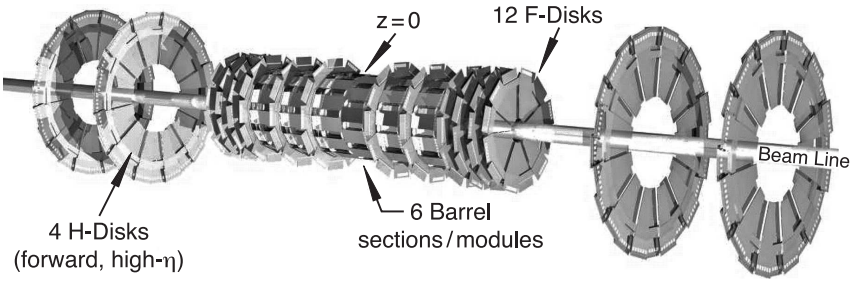

Figure 3.4: Illustration of the Silicon Microstrip Tracker (SMT).

field, created by the solenoid magnet, which curves the trajectories of charged particles. The momentum of a particle is inversely proportional to the curvature of the track. For details of track reconstruction and momentum measurement, see section 4.1.

A schematic of the tracking system can be seen in Fig. 3.3. The tracker begins right outside the beryllium beam pipe, which has a radius of 38.1 mm, and extends radially up to 52 cm; the total length of the tracker, containing SMT and CFT, is 2.52 m.

Silicon Microstrip Tracker

The Silicon Microstrip Tracker allows reconstruction of tracks and vertices in an η-region covering nearly the whole calorimeter and muon system, up to $|\eta_{\text{det}}| = 3$. As can be seen in Fig. 3.4, the SMT consists of a series of barrel and disk shaped sections. This is to maximize the detector surfaces perpendicular to the particle trajectories, since particles flying parallel to the surfaces cannot be detected. In the disc and barrel layout, forward (high η) particles will be detected by the discs, and central particles will mainly hit the barrels.

There are six barrels, which cover a region of up to $|\eta_{\text{det}}| = 3$. Each barrel has four layers (Fig. 3.5). The innermost layers, 1 and 2, contain 12 silicon modules each, which are called ladders. Layers 3 and 4 contain both 24 ladders per barrel, which gives a total of 432 ladder modules. The ladders are aligned axially, which means that the barrels can mainly measure r and ϕ.

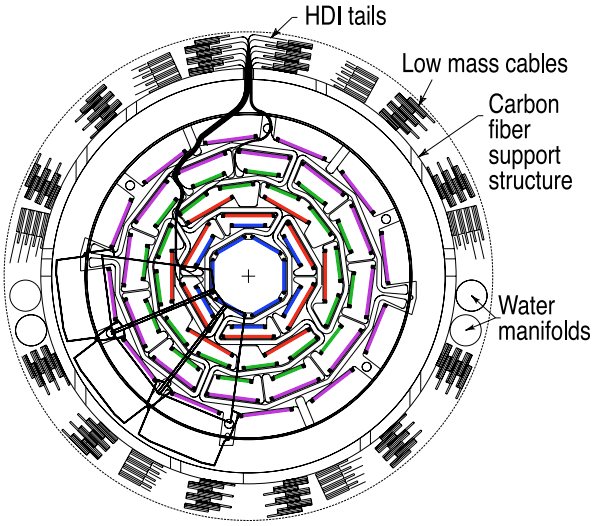

Figure 3.5: An SMT barrel in cross section view. There are four layers, each consisting of two sublayers which are rotated wrt. each other to provide full φ coverage. The two inner layers (blue and red) have 12 silicon modules each, the outer two (green and purple) have 24.

Between and on the caps of the barrels are the 12 F-discs, which are each built of 12 double-sided stereo wedges. Further from the center are four discs called H-discs, which consist of 24 pairs of single-sided wedges. As opposed to the barrels, the discs also provide a good measurement in the r, z-plane, and thus of the inclination of tracks.

During a shutdown in April 2006, the SMT was upgraded with the insertion of "layer 0". Layer 0 consists of 48 silicon strip sensors, mounted in six facets on a carbon fiber support structure. The structure is 1.68 m long and 1.6 cm in radius. Layer 0 has several purposes [14]:

- It improves the resolution of the impact parameter by a factor of two, which is beneficial for example for b-tagging.
- By providing an extra track point closer to the beam, it increases the lever arm of the track. This leads to a better momentum resolution, and a reduced fake rate.
- Furthermore, layer 0 is designed to maintain the functionality of the SMT by compensating for radiation damage to the silicon detector.

Central Fiber Tracker

Surrounding the SMT is the Central Fiber Tracker, CFT. It consists of 76 800 scintillating fibers, cylindrically mounted on 8 support cylinders (see Fig. 3.3). It spans a radial area from $r = 20$ cm up to $r = 52$ cm. The two inner cylinders, which fit between the H-Discs of the SMT, are 1.66 m long, the outer ones are 2.52 m long. The CFT provides tracking in the area of $|\eta_{det}| < 1.6$.

Each of the eight cylinders supports two doublet layers, making a total of 32 single layers. The fibers of half of the doublet layers are laid out axially (parallel to the beam pipe). In every second doublet layer, the fibers are rotated by a stereo angle of $\pm 3°$, permitting a measurement of the z coordinate.

The fibers have a diameter of 835 µm, and the resolution of a doublet layer is approximately 100 µm. The scintillating material radiates at a wavelength around 530 nm, which corresponds to a yellow-green color. The photons are led through clear fiber light guides of 8-12 m length into visible light photon counter modules (VLPCs). These have a high quantum efficiency of more than 75%. Tests with cosmic rays have determined that minimum ionizing particles yield an average of eight photoelectrons per layer in the VLPCs [15].

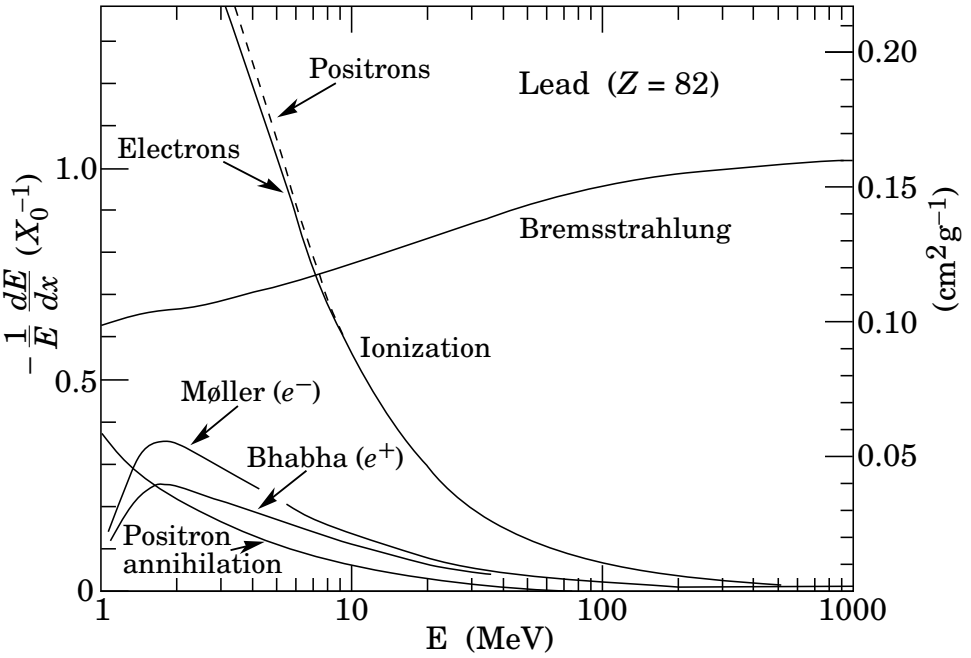

Figure 3.6: Contributions to the energy loss of electrons going through material (here lead). The left axis indicates the fraction of energy lost per radiation length. From [5].

Solenoid Magnet

A solenoidal magnet surrounding the inner tracking system provides a homogeneous magnetic field of 1.92 T. Since the solenoid was added after Run I, its size was restricted by the available space. It is 2.73 m long and 1.42 m in diameter. In the central region, around $|\eta_{\text{det}}| = 0$, this amounts to 0.87 radiation lengths (X_0). The properties of the solenoid were chosen to optimize momentum resolution $\Delta p_T/p_T$ and track recognition. The magnet operates at a temperature of 10 K. It was designed for a current of $I = 4749$ A, which corresponds to a magnetic field of 2 T, and a stored energy of 5.3 MJ. After a shutdown in fall 2004, the magnet could not be ramped to full current due to a defective solder joint. Since then, the current has been reduced to 4550 A, yielding the current field strength of 1.92 T.

3.2.2 Calorimeter System

The calorimeter system consists of the preshower detector, a uranium/liquid argon sampling calorimeter, and the intercryostat detector (ICD). It measures the energies of particles and jets. Since different particles leave different signatures in the calorimeter, they can be distinguished.

Above a certain threshold, electrons lose their energy primarily through bremsstrahlung (Fig. 3.6). Electrons emit photons when deaccellerated in the field of a nucleus. These photons can produce additional electrons and positrons through pair production. The average distance over which an electron loses $1/e$ of its energy is called the radiation length X_0, which is material dependent. Below the mentioned threshold, electrons mainly loose energy via ionization.

Hadronic particles, which participate in the strong interaction, produce pions and nucleons by scattering inelastically with nuclei. The secondary particles can interact themselves with nuclei, forming hadronic showers. The length scale of these showers is determined by the nuclear interaction length λ_I, which also depends on the material.

Neutrinos leave no signal in the calorimeter, but their presence can be inferred from missing transverse energy (MET, $\not\!\!E_T$, see Sec. 4.7). Neutrinos leave no signal in the calorimeter, but their presence can be inferred from the energy imbalance of an event in the transverse plane. The quantity $\not\!\!E_T = |\sum \vec{E}_T|$ is called missing transverse energy (MET). At typical energies, muons are minimally ionizing particles (MIPs), which loose only a small fraction of their energy in the calorimeter, and pass through to the muon chambers. Thus, the missing transverse energy has to be corrected in the presence of muons.

Preshower Detector

The main purpose of the preshower detector is to restore the EM energy resolution which is degraded by the presence of the solenoid. It does so by finding showers that start before the calorimeter. It also helps identifying electrons and correcting calorimeter shower energies. The preshower detector is divided into two regions:

Central Preshower Detector (CPS) The central preshower detector lies in a cylindrical 5 cm gap between the solenoid and the calorimeter. Its radial extent is from 71.8 cm to 74.2 cm, and it covers a pseudorapidity region up to $|\eta_{\text{det}}| < 1.3$. It is made of three layers of triangular scintillator strips, which are connected via clear optical fibers to VLPCs. The strips of the inner layer are laid out axially, whereas the two outer layers are stereo. In front of the CPS is a lead radiator of 0.56 cm or one radiation length thickness. Together with the solenoid, it presents 2–4 X_0 of material, depending on the angle. This material initiates the showering of electrons and photons, to help distinguish them from pions.

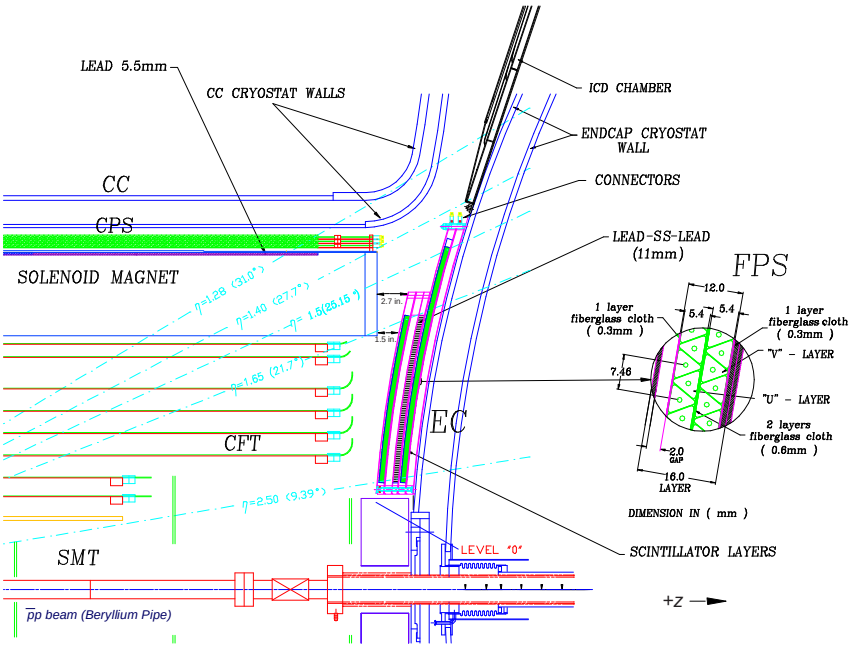

Figure 3.7: The central and forward preshower detectors.

Forward Preshower Detector (FPS) The forward preshower detectors (Fig. 3.7) consist of two layers of scintillators, one in front of and one behind a 2 X_0 stainless steel absorber. Each layer is made of two planes of scintillating fibers, which are, as in the CPS, connected to VLPCs.

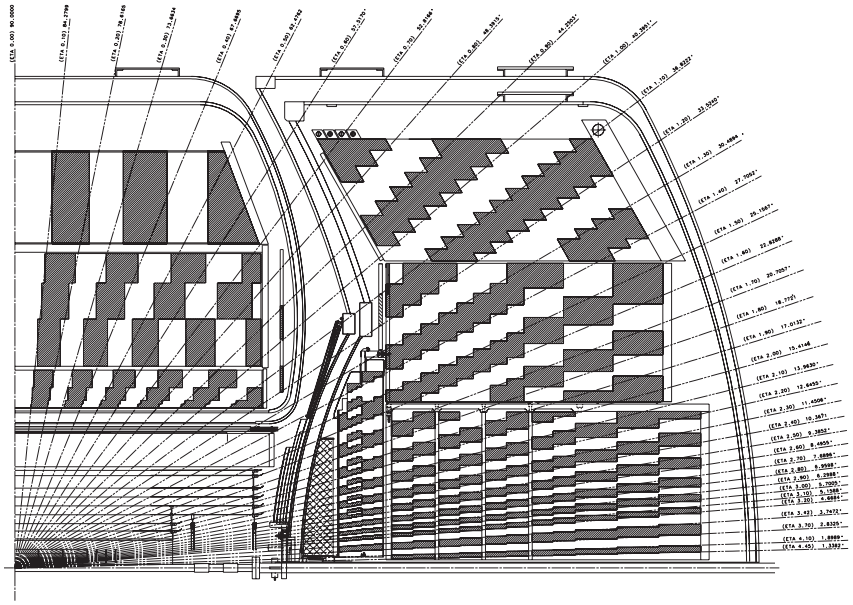

Figure 3.8: A cross-sectional view of the central and endcap calorimeter.

The inner layer is called the "MIP" layer. Charged particles leave minimum ionizing signals here, whereas photons do not tend to interact. Both electrons and photons shower in the absorber, producing a signal in the outer "shower" layer. By matching the two layers, electrons and photons can be distinguished. Heavier charged particles, such as muons, also leave a minimum ionizing signal in the second layer. The MIP layer goes from $|\eta_{\text{det}}| = 1.65$ to 2.5, the shower layer covers $|\eta_{\text{det}}| = 1.5 \ldots 2.5$.

Calorimeter

The calorimeter, which has been part of the detector since Run I, is divided in a central region (CC, $|\eta_{\text{det}}| \lesssim 1$) and two endcaps (EC, $|\eta_{\text{det}}| \approx 1 \ldots 4$, Fig. 3.8). The calorimeter is further divided in an electromagnetic calorimeter (ECal), and fine and coarse hadronic calorimeters (HCal) further away from the interaction point. This is because the maximum in hadronic showers tends to be at a greater depth than in EM showers. The CC and both ECs are in separate cryostats, immersed in liquid argon at 90 K, which also serves as active material.

The smallest unit of the system is a calorimeter cell (Fig. 3.9), consisting of an absorber plate, the liquid filled gap, and a pad. Showers develop in the absorber and deposit energy, causing ionization in the gap. A potential of about 2 kV between the absorber plate and the pad collects the produced charge. In the ECal, there are 3 and 4 mm thick absorber plates made of depleted uranium. The plates in the fine hadronic calorimeter are 6 mm thick, and consist of a uranium alloy with 2% niobium. The coarse HCal uses 46.5 mm absorbers, which are made of copper in the CC, and stainless steel in the EC. The fraction of energy deposited in a calorimeter differs for electromagnetic and hadronic jets, however, for the DØ calorimeter the ratio of EM to hadronic response is in the range 1.02–1.09, making it an almost compensating calorimeter.

The ECal has four layers, and is designed such that the EM shower maximum tends to lie in the third layer. The thickness of the layers are 1.4, 2.0, 6.8 and 9.8 X_0 in the CC, and 1.6, 2.6, 7.9 and 9.3 X_0 in the EC. The granularity of the calorimeter is $\Delta\eta \times \Delta\varphi \approx 0.1 \times 2\pi/64 \approx 0.1 \times 0.1$, except in the 3rd layer of the ECal, where it is enhanced to 0.05×0.05. Altogether, the calorimeter cells have 55.000 readout channels.

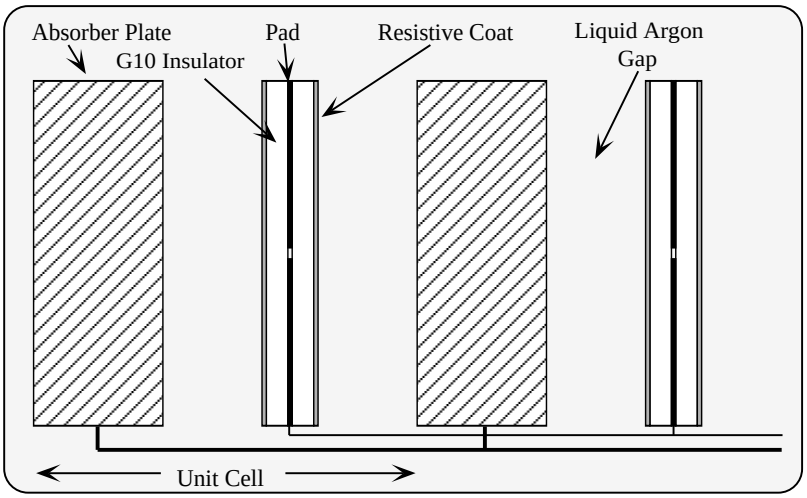

Figure 3.9: Schematic drawing of a calorimeter unit cell.

Particle	A	B	C
e	$0.0115^{+0.0027}_{-0.0036}$	$0.135 \pm 0.005\sqrt{\text{GeV}}$	0.43 GeV
π	0.032 ± 0.004	$0.45 \pm 0.004\sqrt{\text{GeV}}$	0.975 GeV

Table 3.1: Calorimeter resolution for electrons and pions.

Since the deposited energy is proportional to the number of charges produced, there is a Poissonian error $\Delta E \propto \sqrt{E}$ on the energy measurement. The complete uncertainty can be parametrized as follows:

$$\Delta E = \sqrt{(A \cdot E)^2 + (B \cdot \sqrt{E})^2 + (C)^2}\,, \tag{3.4}$$

where the term proportional to the energy comes from calibration uncertainties, the second term is the Poissonian term, and the constant term is due to noise. The values in Tab. 3.1 for the parameters A, B and C have been determined with a test beam [16].

Due to gaps between the central and endcap cryostats, there is a reduced acceptance in the region $|\eta_{\text{det}}| = 0.8 \ldots 1.4$. The intercryostat detector sits in these gaps, attached to the endcaps. It is made of layers of scintillating tiles, covering the region $|\eta_{\text{det}}| = 0.8 \ldots 1.4$. Furthermore, there are additional calorimeter cells called "massless gaps" added in front of the first layer of uranium to improve the sampling of showers.

3.2.3 Muon System

The muon system, which surrounds the calorimeter, consists of toroidal magnets, and a central and forward muon detector. The only particles that can reach it with a high probability are muons, because they are minimum ionizing particles. The muon detectors are made of drift tubes (or wire chambers) and scintillators. Furthermore, they are divided into three layers, A, B and C. The wire chambers are gas filled, rectangular boxes, containing wires under high voltage. When a charged particle passes through the chamber, it ionizes the gas, and the ions and electrons drift to the wires or walls. The hit position along the wire can be determined from vernier cathode

pads on the walls, and the difference in signal times from neighboring wires. The scintillators emit photons when hit by a muon, which are registered by photomultiplier tubes (PMTs). The scintillators fire muon triggers and signal that a muon track is in a certain part of the detector. The drift tubes fire triggers as well, but also measure the position of muons. From these hits, the trajectories of muons can be reconstructed, and their momentum and charge can be determined. Also, the signals in the muon system are matched to tracks in the central tracker, which provide a more accurate momentum measurement.

Toroid Magnets

The toroid was already part of the Run I detector. It has a magnetic field of 1.8 T and a current of 1500 A [13]. The toroid magnets lie between the A and B layers of the muon system, starting at a radius of $r = 317.5$ cm. There are three parts, forming a square annulus 109 cm thick. The total weight is 1973 (metric) tons. The central part is made of two C-shaped sections, installed at $z = \pm 454 \ldots 610$ cm. The magnetic field circles around the detector, so that the field is in x-direction on the top and bottom, and in y direction on the sides. The Lorentz force acts in the plane spanned by $\vec{r}$ and $\vec{z}$, where $\vec{r}$ is pointing to the radial position of the muon. If the particle originates from the center of the detector and passes the magnetic field perpendicularly, it is deflected towards z, in the direction of the beam pipe.

Central Muon Detector

The central muon detector covers up to $|\eta_{\text{det}}| \lesssim 1.0$. Its wire chambers are called proportional drift tubes (PDTs), and have an area of about $2.8 \times 5.6\,\text{m}^2$ facing the center of the detector. A single cell is $10.1 \times 5.5\,\text{cm}^2$ in size. The PDTs are filled with a gas mixture of 84% argon, 8% methane (CH_4), and 8% CF_4. The electrons and ions have a drift velocity of about 10 cm/μs and a maximum drift time of 500 ns. The wires are laid out parallel to the magnetic field. The scintillators of the A-layer surround the central calorimeter, and are called the A-φ scintillation counters. The scintillators of the C-layer on the top and on the sides are called "cosmic caps", whereas those below the detector are called "bottom counters".

Forward Muon Detector

The forward muon detector was added for Run II, and extends the coverage of the muon system up to $|\eta_{\text{det}}| \lesssim 2.0$. It features smaller drift chambers, called mini drift tubes (MDTs). Each MDT consists of 8 cells, $9.4 \times 9.4\,\text{mm}^2$ in area. They are filled with 90% CF_4 and 10% methane. The drift time is 60 ns, and the accuracy of the track measurement is approximately 0.7 mm.

3.2.4 Luminosity Monitor

The luminosity monitor (LM) measures the instantaneous luminosity at the interaction point by detecting inelastic $p\bar{p}$ collisions. It also provides information on the beam halo, and a fast measurement of the z position of the beam spot. The LM has two parts (north and south), positioned in front of the endcap calorimeters at $z = \pm 140$ cm, between the beam pipe and the forward preshower detector (Fig. 3.10). It covers the region $|\eta_{\text{det}}| = 2.7 \ldots 4.4$. Both parts are made of 24 plastic scintillator counters, connected to PMTs. The counters are arranged radially and are 15 cm long.

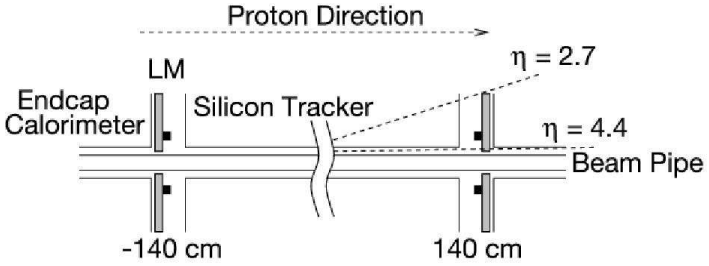

Figure 3.10: Position of the luminosity monitor in the DØ detector.

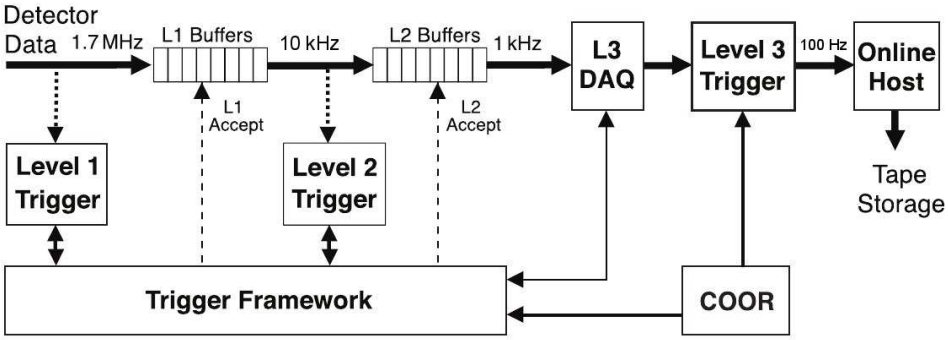

Figure 3.11: An overview of the DØ data acquisition and trigger system.

From the measured rate of inelastic $p\bar{p}$ events dN/dt, the instantaneous luminosity $\mathcal{L}$ can be determined:

$$\mathcal{L} = \frac{1}{\varepsilon \cdot A \cdot \sigma_{p\bar{p}}} \cdot \frac{dN}{dt} ,$$

where ε and A are efficiency and acceptance of the luminosity monitor, and $\sigma_{p\bar{p}}$ is the inelastic $p\bar{p}$ cross-section. To distinguish signals from $p\bar{p}$ scattering from beam halo background, time-of-flight measurements are made. The z-coordinate of the interaction vertex z_v can be determined from the difference in time-of-flight of the two LM detectors. Beam halo particles will appear to have $z_v \approx 140$ cm, and can be eliminated with a cut of $|z_v| < 100$ cm.

The recording time of the DØ detector is divided into so called luminosity blocks, or lumi blocks. For each lumi block, the instantaneous luminosity is averaged, and assumed constant. The duration of one block is 60 seconds or less, to satisfy this assumption. Lumi blocks are referenced by their luminosity block number, or LBN, which is incremented for each new block.

3.2.5 Triggers

With a bunch crossing every 396 ns, the event rate of the detector is 2.5 MHz. However, only 50 events can be stored per second. The purpose of the trigger system is to select interesting events and to reduce the data rate. The trigger system is composed of three layers. In the following, the general function of the trigger system will be explained. The specific triggers used for this analysis will be presented in a later chapter.

Level 1

The level 1 trigger is implemented completely in hardware and operates on simple objects to obtain maximal speed. For example, a trigger fires when a calorimeter tower of $\Delta\eta \times \Delta\varphi = 0.2 \times 0.2$

(at L1) measures energy above a given threshold. Tracks are reconstructed from hits in the preshower detector, the CFT, and the muon system. These have to exceed certain minimum transverse momentum to cause the event to pass. Level 1 triggers on electrons up to $|\eta_{\text{det}}| = 2.5$ and on muons up to $|\eta_{\text{det}}| = 2.0$. The L1 trigger can issue a decision in 3.5 µs and passes data on to Level 2 at a rate of 10 kHz.

Level 2

The level 2 trigger operates in two stages. First, in the preprocessor stage it collects information from various subsystems to build objects like energy clusters or tracks. The systems taken into account are the calorimeter, the preshower detector, the CFT, SMT and the muon chambers. In the second (global-processor) stage, these pieces of information are combined into candidates for physical objects (such as muons and electrons), and trigger decisions are issued. The L2 trigger has a 5% downtime at highest rates, and takes less than 100 µs for a decision. It reduces the data rate to about 1 kHz.

Level 3

While the L2 trigger operates on single objects, the L3 trigger works on event level. Each event is delegated to a farm node, where a simplified event reconstruction is performed. The level 3 trigger reduced the rate to about 100 Hz, which is then written to disk. The average size of an event is 250 kB.

4 Object Identification

4.1 Tracks

Charged particles move along curved paths in the magnetic field of the detector. When passing surfaces of the tracking system, they leave hits, from which the tracks can be reconstructed.

4.1.1 Finding Tracks

A combination of several algorithms is used to reconstruct tracks from hits in the tracking system. The histogram track finder (HTF) and the alternative algorithm (AA) find candidate tracks, which are used as input for the global track reconstruction (GTR).

The **histogram track finder (HTF)** [17] is an algorithm which finds tracks efficiently even in presence of a very large number of hits N_{H}. The method is based on the Hough transform, and was already used to find tracks in pictures from bubble chambers [18]. The HTF operates in the transverse plane, and assumes the impact parameter d_0 to be negligible. In this case, a track is characterized by its direction ϕ and radius of curvature ρ. A simple method to find tracks would be the following: For each pair of hits, a track candidate is constructed, which connects the hits with the origin. The parameters ϕ and ρ of the track are then filled into a two-dimensional histogram. Since all pieces of a track have the same curvature and a similar direction, actual tracks appear as concentrations in the histogram. However, since all pairs of hits have to be considered, this algorithm has a complexity of $\mathcal{O}({N_{\mathrm{H}}}^2)$, and does not scale well with the number of hits. An improvement can be made by using the Hough transform. Each single hit in the detector corresponds to several possible ϕ, ρ values, or a line in ϕ, ρ space. The actual algorithm loops over all hits, and over all ρ bins, calculates ϕ for the current hit and ρ, and increments the corresponding bin. This needs just $\mathcal{O}(N_{\mathrm{H}} \times N_\rho)$ calculations (where N_ρ is the number of ρ bins).

Both the alternative algorithm and general track reconstruction are examples for road-following methods. The **alternative algorithm (AA)** [19] starts from a group of three hits in the SMT and extrapolates outwards. It adds additional hits on its "road" to the track, if the total χ^2 the track fit remains below a certain threshold. The algorithm ends when it reaches the outside of the CFT, or when three layers without hit are encountered.

The **GTR method** ([20]) starts with candidate tracks in the center of the detector and propagates them outwards, simulating the magnetic field and the interaction of particles with matter. As the tracks cross detector surfaces, new hits are added and the track parameters are updated. The basic elements of the algorithm are described in the following.

- GTR maintains a model of the detector as simple geometric **surfaces**. Hits are described as intersections of tracks with these surfaces. The CFT is modeled by cylinders, the SMT by planes perpendicular to the z-axis (for the discs) or parallel to the z-axis (x-y planes, for the barrels).

- A list of surfaces an outwards moving particle could cross is called a **path**. The first few surfaces of a path are used to build a seed track to start the algorithm.

- **Propagators** extrapolate a given track to the remaining surfaces. The propagator simulates the motion of the charged particle in the magnetic field of the detector. The track errors are updated when the track crosses material to account for multiple scattering and energy loss.
- When the propagated track reaches a new detector surface, a **fitter** attempts to add new clusters of hits to the track. For each possible combination of track and cluster, it calculates a χ^2, and rejects the combination if it is too high. If the cluster is added, the track parameters and errors are updated. It is possible that the track has no matched cluster on the surface, due to acceptance gaps and inefficiencies. In this case, the probability for a missing hit is recorded, and the algorithm continues.
- After processing all surfaces in a path, a series of **filters** clean the list of track candidates. Tracks are rejected based on their χ^2 value, and the number of missed surfaces (with regard to the miss probability). Tracks can also be rejected when they share 4 or more clusters with another track. In this case, the track with the best χ^2 is kept.

The output of the algorithm is a list of tracks. In principle, these tracks could be used as seeds for another round of the algorithm, extending them into other parts of the detector.

4.1.2 Track Parametrization

A general helical track going through a point has six parameters: three to define the point, two for the direction, and one for the curvature of the path. If the point along the track is not needed to be known, the curve can be described by five parameters. Conventionally, the TRF parameter set is used (named after the track finding software TRF):

- d_0 describes the distance of closest approach (dca) of the track to the z axis.
- ϕ is the angle of the track in the transversal plane at the point of closest approach.
- ρ is the radius of curvature of the track when projected into the transversal plane.
- d_0 gives the position of the point of closest approach along the z axis.
- $\tan\lambda$ describes the inclination of the track, or how fast it progresses in z direction while moving around the circle in the transverse plane (Fig. 4.1).

Note that the first three variables already describe the transverse projection of the track (Fig. 4.2). Through d_0, the point of closest approach is fixed to a circle around the origin. The angle ϕ defines a tangential vector to the track. Since the shortest line connecting a circle and a point is perpendicular to the tangent of the circle, $\vec{dca}$, the vector to the point of closest approach, must be perpendicular to ϕ. This fixes $\vec{dca}$ to two possible points. Also, the curvature can be clockwise or counterclockwise. This fourfold ambiguity is resolved by allowing d_0 and ρ to have signs.

Additional parametrizations are used by the GTR algorithm to describe the intersection of tracks with certain detector surfaces (Fig. 4.3). Given a fixed surface, the track and the intersection point can be specified with five free parameters. Surfaces of the central fiber tracker are described by cylinders of radius r centered around the z axis. (Deviations from the ideal form due to mis-alignment are negligible for purposes of parametrization.) The position of a hit on the cylinder is given in cylinder coordinates, z and $\phi = \arctan(y/x)$. The direction of the track in the intersection point is given by the angles α and λ. $\alpha = \phi_{\text{position}} - \phi_{\text{direction}}$ is the track

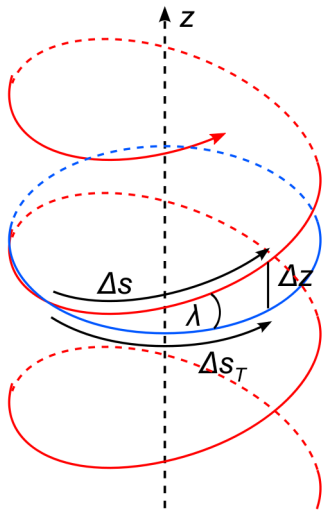

Figure 4.1: The parameter $\tan\lambda$ describes how fast the track advances in z direction. Let s be the position along the track and s_T the projection of s to the transverse plane, then $\tan\lambda = \partial z/\partial s_T$.

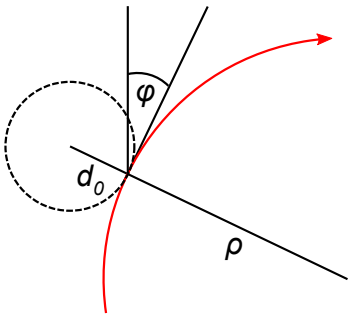

Figure 4.2: Track parameters in the transverse plane. The z axis is in the center of the dotted circle. The red circle is the track. d_0 is the distance of closest approach (dca), ρ the radius of curvature, and ϕ the polar angle of the track at the point of closest approach.

direction in the transverse plane, relative to ϕ. $\tan\lambda$ is defined as in the TRK parametrization above.

4.1.3 Momentum measurement

Given the track's radius of curvature r, measured in the transverse (r, φ) plane, the transverse momentum $p_T = \sqrt{{p_x}^2 + {p_y}^2}$ can be determined:

$$p_T = r \cdot B \cdot 0.3 \frac{\mathrm{GeV/c}}{\mathrm{m \cdot T}},$$

where B is the magnetic flux density. The uncertainty on the p_T measurement is given by the Glückstern formula:

$$\frac{\sigma(p_T)}{p_T} = \frac{\sigma(x) \cdot p_T}{0.2 \cdot BL^2} \cdot \sqrt{\frac{720}{N+4}}. \tag{4.1}$$

Here, L is the chord length of the track, and N is the number of sampling points (hits) used to construct the track (see Fig. 4.4). An alternative expression for the transverse momentum, using the sagitta s, is

$$p_T = \frac{0.3}{8} \frac{BL^2}{s} \tag{4.2}$$

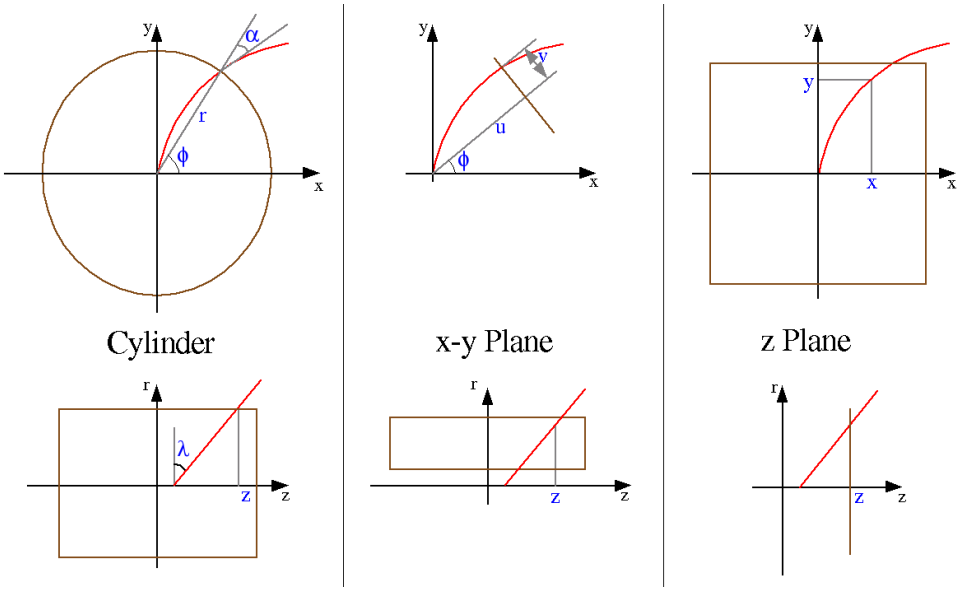

Figure 4.3: Track parametrizations used in GTR, from [20]. The track is shown in red, the surface is brown, and the track parameters are blue.

with the uncertainty

$$\frac{\sigma(p_T)}{p_T} = \frac{\sigma(s)}{s} = \frac{\sqrt{\frac{3}{2}}\sigma(x) \cdot 8p_T}{0.3 \cdot BL^2} \,. \tag{4.3}$$

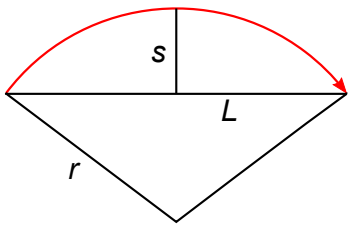

Figure 4.4: Visualization of the sagitta. The red curve is the track. The radius is r, the chord length is L and the sagitta is s.

An additional contribution to the uncertainty of the momentum measurement comes from multiple scattering [21]:

$$\frac{\sigma(p_T)}{p_T} = \frac{0.05}{BL}\sqrt{\frac{1.43L}{X_0}} \,. \tag{4.4}$$

4.2 Primary Vertex

The sites of interactions, from which tracks originate, are called vertices. The primary vertex (PV) is defined as the location of the $p\bar{p}$ collision. It is important to know which tracks come from the primary vertex, and which from secondary vertices, e.g. from decays of heavy quarks or from additional interactions. The reconstruction of the primary vertex is done with the Adaptive Vertex Reconstruction (APV) algorithm.

First, all tracks with $p_T > 0.5$ GeV – and if they are in the SMT acceptance region, at least 2 SMT hits – are considered. A z-clustering algorithm groups tracks within 2 cm in beam direction from each other together, assuming they belong to the same interaction. For each cluster, tracks

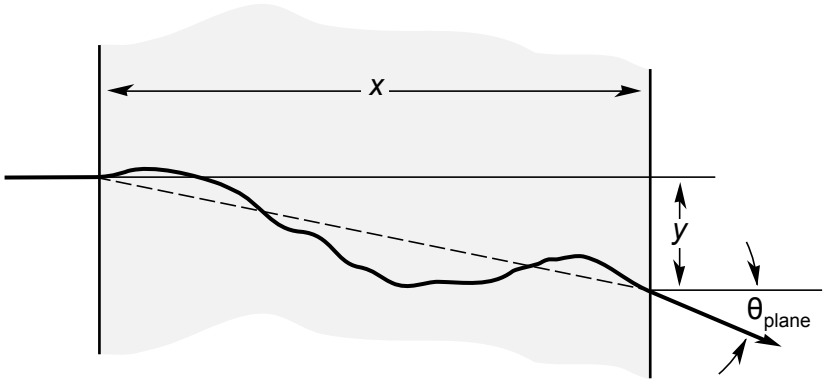

Figure 4.5: Illustration of multiple scattering, adapted from [20]. A particle passes through a piece of material of thickness x. The deflection in the transverse plane is given by y, the angle of deflection by θ_{plane}.

are preselected based on their χ^2 in a Kalman fitter vertex-fitting algorithm and on their distance to closest approach to the beam spot (dca). Then the APV algorithm is applied to the preselected tracks. In an iterative procedure, each track is reweighted based on the tracks contribution to the χ^2 of an attempted fit to the vertex. When the fit converges, the vertex is stored.

Now the primary vertex is chosen from the list of found vertices. It is assumed that most other vertices are from minimum bias events (MBE), which tend to have lower p_T tracks. Each vertex is assigned a probability to be a MBE, based on the p_T of its tracks. The vertex with the lowest probability is chosen as the primary vertex.

In this analysis, the following requirements are made to the primary vertex:

- The z-position of the primary vertex must be at most 60 cm from the center of the detector ($|z_{\text{PV}}| < 60$ cm).
- There must be at least three tracks matched to the primary vertex.

4.3 Muons

Muon identification in the DØ detector involves the muon system, the tracking system, and the calorimeter. The muon system, which has an angular acceptance of 90%, can detect muons unambiguously. The DØ reconstruction software combines hits in the three layers of the muon system to local muon segments (either A or BC). A and BC segments can be combined, forming a local muon track, with a momentum measurement. A muon signature in the muon system is called a *local muon*.

The central tracker (SMT and CFT) finds charged tracks, and provides an accurate momentum measurement in the whole acceptance region of the muon system. A muon identified in the muon system that can be matched to a central track is called a *central track-matched muon*. In case a local track could not be fitted, a central track can be used as a starting point and matched to hits in the muon system.

A further way to identify muons is to look for MIP signatures in the calorimeter. Due to the fine granularity of the calorimeter, it is possible to build tracks of calorimeter cells. An energy deposition of about 3 GeV is indicative of a minimum ionizing particle such as a muon. This method, muon tracking in the calorimeter (MTC), has an efficiency of about 50%, much less

than the other methods. Its benefit is that it provides an independent measurement, and that the calorimeter has a higher angular acceptance than the muon system.

4.3.1 Muon type (nseg)

Reconstructed muons are classified by two variables: muon type (nseg) and muon quality. The possible values for nseg are given in Tab. 4.1. nseg = 3 means that a local muon with A and BC segments was matched to central track, or if the fitting of the local muon track did not converge, a central track was matched to the local muon segments. A nseg = 2 (1) muon is a central track matched to a BC (A) segment. If nseg = 0, either a central track is matched to hits in the muon system (no segment), or to a muon track in the calorimeter (MTC). Negative values of nseg indicate the absence of a central track.

nseg	Muon Type	Matching
3	central track + muon track (A and BC)	*if muon track fit converged:* muon → central *else:* central → muon
2	central track + BC only	central → muon
1	central track + A only	central → muon
0	central track + muon hits	central → muon
	central track + MTC	central → calorimeter

Table 4.1: Definition of muon types (nseg). A negative value for nseg means there is no matched central track.

4.3.2 Muon quality

The other variable used to classify muons is the muon quality, which can be either "loose" or "medium" (the previously used "tight" quality has been dropped in p20) [22]. The requirements for muon quality depend on the nseg variable:

|nseg| = 3: A muon with |nseg| = 3 has medium quality, if it has:

- At least 2 A layer wire hits
- At least 1 A layer scintillator hits
- At least 2 BC layer wire hits
- At least 1 BC layer scintillator hit (not required for central muons with less than four BC wire hits)

A |nseg| = 3 loose muon is allowed to fail one of these tests, where the A layer wire and scintillator hit requirements are counted as one test. Furthermore, there has to be at least one scintillator hit at all.

nseg = +2: Muons with |nseg| < 3 can only be loose or medium, if matched to a central track (positive nseg). An nseg = 2 muon is loose if it has

- At least 2 BC layer wire hits
- At least 1 BC layer scintillator hits.

It is medium, if it fulfills the criteria for loose, and is in the bottom part of the detector (fifth or sixth octant), and has $|\eta_{\text{det}}| < 1.6$.

nseg = +1: The requirements are the same as for nseg = 2, but with the A layer replacing the BC layers. Additionally, low momentum nseg = 1 can be marked as medium. A muon is defined as low momentum in this sense if its probability to reach the BC layer is less than 0.7. The probability is calculated as a function of muon $|\eta|$ and momentum using a GEANT simulation. Details can be found in [23].

4.3.3 Muon isolation

An important quantity to distinguish muons originating from different physical processes is muon isolation. For example, a muon from the semileptonic decay of a B meson will be accompanied by a b jet, and will be (in average) less isolated than a muon from a leptonic Z decay. There are two commonly used definitions for muon isolation at DØ:

$$\text{etHalo} := \sum_{0.1<\Delta R<0.4} E_T \qquad \text{and} \qquad \text{etTrkCone5} := \sum_{\Delta R<0.5} p_T \tag{4.5}$$

etHalo is the sum of the calorimeter transverse energy in a hollow cone from $\Delta R = 0.1$ to 0.4 around the muon. Energy deposited in coarse hadronic cells is not included in the calculation. etTrkCone5 is the sum of transverse momenta of all central tracks in the cone $\Delta R < 0.5$ around the muon, excluding the track of the muon itself. Only tracks whose origin on the z axis is within 2 cm of the muon origin are included in the sum. Further details can be found in [23].

4.3.4 Cosmic veto

A veto is normally applied to reject cosmic ray muons. All hits in the A and BC layers have to fall within a ±10 ns window around the expected hit times (assuming the muon originates near the center of the detector and propagates outwards), otherwise the muon is marked as cosmic.

4.4 Electrons

Electrons are reconstructed using the calorimeter and the tracking system. The calorimeter measures the energy of electrons, whereas the tracking system provides a better angle measurement when the calorimeter signal can be matched to a track.

The identification of electrons starts with electromagnetic (EM) clusters in the calorimeter. A cluster in the central calorimeter is defined as a group of towers adjacent to the tower with the highest energy of the cluster. All towers must lie within $\Delta R = \sqrt{\Delta\varphi^2 + \Delta\eta_{\text{det}}^2} < 0.2$ of the highest energy tower. In the endcap, a cluster is formed around a cell with a local maximum of energy. All adjacent cells within a transverse distance of 10 cm belong to the cluster. Additionally, the following criteria have to be met:

- The transverse momentum p_T of the EM cluster has to be greater than 1.5 GeV.
- An electron as opposed to a hadronic particle leaves most of its energy in the electromagnetic calorimeter. Thus, a high EM fraction is needed:
$$f_{\mathrm{EM}} = \frac{E_{\mathrm{EM}}}{E_{\mathrm{tot}}} > 0.9\,.$$
- An isolation cut is applied. The energy deposited in the area around the EM cluster has to be significantly lower than the energy of the cluster itself. This is ensured by the following cut:
$$f_{\mathrm{iso}} = \frac{E_{\mathrm{tot}}(\Delta R < 0.4) - E_{\mathrm{EM}}(\Delta R < 0.2)}{E_{\mathrm{EM}}(\Delta R < 0.2)} < 0.2\,.$$

The main backgrounds to electron identification are from charged and neutral pions, η mesons and photons. Through demanding a central track in the direction of the EM cluster, the background from uncharged particles can be greatly reduced. Further details on electron identification can be found in [24] and [25].

4.5 Jets

Quarks and gluons hadronize and form showers in the calorimeter, which can be recognized as jets. Which jets are found is dependent on the algorithm used. A good jet algorithm should be infrared safe, that is it should produce the same results in the presence of soft gluon radiation (Fig. 4.6(a)). It should also be collinear safe, which means the results should be not affected if the energy is split between adjacent cells due to collinear radiation (Fig. 4.6(b)).

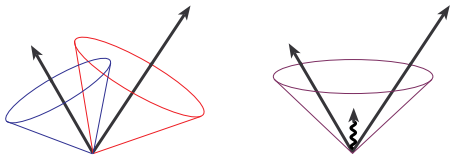

(a) Infrared safety: In this example, jet reconstruction starts around seed particles, drawn as arrows. The energy is proportional to the arrow length. Note how a small energy deposition from soft radiation may cause merging of the jets.

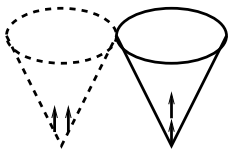

(b) Collinear safety: In the left image, an unsafe algorithm would fail to find a seed, because the energy is split between two calorimeter towers. In the case on the right side, a seed is produced because the energy is more narrowly distributed.

Figure 4.6: Demonstration of infrared and collinear safety. Images taken from [26].

The method used to find jets at DØ is called the Run II Improved Legacy Cone Algorithm (ILCA). First, preclusters are formed using the "simple cone algorithm". It starts with the tower with the highest measured p_T, which must have at least $p_T > 0.5$ GeV. Then, all towers within a range of $\Delta R < 0.3$ with $p_T > 1$ MeV are added to the precluster. The algorithm continues with the next highest p_T tower left, until there are no more towers above the threshold. The found preclusters and certain midpoints between preclusters are used as seeds to form "proto-jets". These have a cone size of either $\Delta R = 0.7$ (JCCA) or 0.5 (JCCB), however in this analysis only the JCCB algorithm is used. The proto-jets are allowed to overlap initially. Jet splitting and merging is performed to avoid double counting of energy. Afterwards, all jet candidates with $E_T > 6$ GeV are kept.

Among the jet candidates, there can still be fakes from electrons, photons, or noise. To reduce this, additional cuts are applied:

- Single noisy calorimeter cells are called "hot cells". Jets which are dominated by a hot cell can be removed via the cut

$$\text{HotF} = \frac{E_T(\text{leading } E_T \text{ cell})}{E_T(\text{second } E_T \text{ cell})} < 10\,.$$

- Jets are removed when more than 90% of the energy comes from a single tower (n90 > 1).
- A cut to the electromagnetic fraction is applied to separate jets from EM objects ($f_{\text{EM}} < 0.95$). There is also a minimal f_{EM} value to reject noise from the electromagnetic calorimeter. It is η_{det} dependent, due to the intercryostat gap. The cut in the central region is $f_{\text{EM}} > 0.05$, or lower in other regions.
- Due to strong noise in the coarse hadronic calorimeter, the fraction of jet energy deposited there is restricted to $f_{\text{CH}} < 0.4$, or depending on η_{det}, a higher value.
- The energy measured in the constructed jet (the precision readout) should match the energy visible in the L1 trigger readout. This is expressed by

$$\text{L1}_{\text{ratio}} := \frac{p_T(\text{L1 readout})}{p_T(\text{prec. readout})} > 0.5\,.$$

  Again, depending on η_{det}, the lower bound may be smaller.

4.6 Jet Energy Scale

Figure 4.7 shows the typical evolution of a jet, starting with a parton jet coming from the hard scattering. The partons hadronize and form a particle jet. The particle jet then showers in the calorimeter and deposits its energy. However, the measured energy of a calorimeter jet does not necessarily equal the energy of an outgoing parton from the hard scattering, nor the sum of all particle energies. This is due to various reasons: dead material in front of the calorimeter, where energy depositions are not registered, non-linearities in the calorimeter response, or electronic noise.

Jet energy scale (JES) is a correction of measured jet energies to energies of stable-particle jets, before interactions with the detector. It includes corrections for energy losses due to muons or neutrinos in the final state, out of cone showering, and other effects [27]. JES however does not account for hard gluon emission, which can radiate energy at large angles from partons. The correction formula is:

$$E_{\text{jet}}^{\text{corr}} = \frac{E_{\text{jet}}^{\text{obs}} - O}{F_\eta \cdot R \cdot S}\,. \tag{4.6}$$

Here, O is an energy offset, F_η is an η_{det} dependent response function, and R is a correction for the absolute calorimeter response, depending on the jet energy. The factor S is a correction for shower development.

4.7 Missing Transverse Energy

Neutrinos and other possibly existing, only weakly interacting particles like the supersymmetric LSP leave no tracks in the detector and deposit no energy in the calorimeter. Their presence can only be inferred from an energy or momentum imbalance in the event. At a hadron collider like

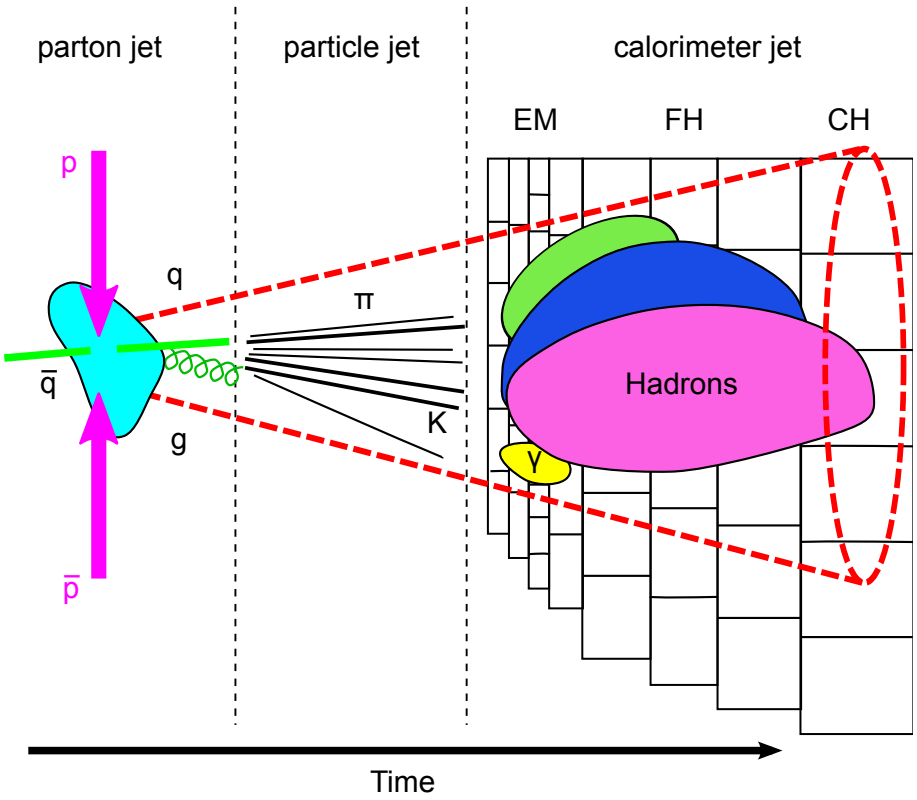

Figure 4.7: Evolution of a jet in the detector. Jets start as parton jets. The partons hadronize and form a particle jet, containing mesons and hadrons. When these pass through material such as the calorimeter, they start showers (calorimeter jets).

the Tevatron, the initial momentum of the $q\bar{q}$ system in z direction is not known. Since the total energy and momentum in the transverse plane is zero, it is useful to work with transverse energy E_T and momentum p_T.

To determine the missing transverse energy, the vectorial sum in the transverse plane of the energy deposited in all calorimeter cells is calculated. Cells with less than 100 MeV are left out, as well as cells of the coarse hadronic calorimeter, if they are not part of a jet. This is to reduce contributions from noise. The vector opposite to the resulting vector is the uncorrected missing transverse energy, $\not\!\!E_T^{\text{uncorr}}$. Symbolically, it is given by

$$\vec{\not\!\!E}_T^{\,\text{uncorr}} = -\sum \vec{E}_T \qquad \text{or} \qquad \not\!\!E_T^{\text{uncorr}} = \left|\sum \vec{E}_T\right| \tag{4.7}$$

where the vectors are in the transverse plane, and the summation is over all included cells as mentioned above. In the next step, the energy of all jets and EM objects is corrected, and these corrections are also applied to $\not\!\!E_T^{\text{uncorr}}$, resulting in the calorimeter missing transverse energy, $\not\!\!E_T^{\text{cal}}$. Finally, muon corrections are applied. As minimal ionizing particles, muons leave only about 3 GeV in the calorimeter – essentially independent of their actual energy. The real transverse energy of the muon is determined using the p_T of a matched track, and $\not\!\!E_T^{\text{cal}}$ is adjusted accordingly. The result is the fully corrected $\not\!\!E_T$.

5 Event samples and processing

5.1 Data

The data used in this analysis was taken during the RunIIb period of the DØ experiment, between June 2006 and June 2009, and has an integrated luminosity 4.3 fb^{-1}. It is divided into two epochs:

- Run2b-1 (formerly RunIIb preshutdown-2006), from June 9, 2006 until Aug. 4, 2007.
- Run2b-2 (formerly RunIIb postshutdown-2006), from Oct. 28,2007 - Jun. 13, 2009.

This corresponds to the following skims:

Run2b-1:

- CSG_CAF_MUinclusive_PASS2_p21.10.00

Run2b-2:

- CSG_CAF_MUinclusive_PASS4_p21.10.00_p20.12.00
- CSG_CAF_MUinclusive_PASS4_p21.10.00_p20.12.01
- CSG_CAF_MUinclusive_PASS4_p21.10.00_p20.12.02
- CSG_CAF_MUinclusive_PASS4_p21.10.00_p20.12.04
- CSG_CAF_MUinclusive_PASS4_p21.12.00_p20.12.05_allfix

All events which pass the `MU_MegaOR` trigger list are considered. Data quality definitions version v2010-03-11 are used. All runs which were marked as bad for calorimeter, SMT, CFT and muon system are removed, as well as events with bad luminosity blocks. Also, all events with flags `cal_empty_crate`, `cal_noon_noise`, `cal_coherent_noise` or `cal_ring_of_fire` have been removed.

5.2 Software

This analysis is performed using the DØ common analysis framework (CAF) release p21.18.00. Data has been brought into TMBTree format using `tmb_analyze` p21.11.00 for all data and background MC samples. The package `vjets_cafe` v5.3 prepared by the V+jets group has been used for selections and to apply standard corrections to Monte Carlo and data. These include the application of the jet energy scale and the recalculation of MET. For Monte Carlo, corrections are applied for object identification efficiencies, as well as an additional muon p_T smearing. The likesign selection and the treatment of QCD multijet and charge flip backgrounds has been done with the package `np_lsdimuon`, which has been developed for this analysis. The versions of all used packages are displayed in Tab. 5.1.

Package	Version	Package	Version
cafe_sam	p21-br-06	tmb_tree	p21-br-71
caf_util	p21-br-129	dq_defs	v2010-03-11
caf_mc_util	p21-br-152	emid_eff	v8-preliminary-01
caf_trigger	p21-br-88	jetid_eff	v04-01-01
dq_util	p21-br-05	lumi_profiles	v2010-05-11
caf_dq	p21-br-04	muid_eff	v05-01-02
emid_cuts	p21-br-25	beamposition	v2010-04-14
eff_utils	p21-br-26	vjets_cafe	v05-03-01
caf_eff_utils	p21-br-18	np_lsdimuon	v00-00-03
cafe	p21-br-38		

Table 5.1: Versions of the `cafe` packages used in this analysis.

5.3 Signal Monte Carlo

Monte Carlo for the signal has been generated by PYTHIA 6.310, using Les Houches Accord (LHA) input from SOFTSUSY 1.9.1. The samples were generated using (CTEQ6L1) parton distribution functions (PDFs), and processed with full detector simulation using reconstruction software version p20.08.02. Zero bias events were produced with software version p20.08.01 and overlaid over the signal MC events. Finally, CAF trees were produced with p21.08.01.

Events were generated for 17 SUSY points, close to the $\tilde{\ell}_R = \tilde{\chi}_2^0$ line. The masses m_0 and $m_{1/2}$ were varied, while the other mSUGRA parameters were fixed to $A_0 = 0$, $\tan\beta = 3$ and $\mu > 0$. The list of points is given in Tab. 5.2. The cross sections have been calculated with PROSPINO 2, the SUSY spectra determined by SOFTSUSY 2.0.14. The branching ratios were calculated by PYTHIA 6.323.

5.4 Background Monte Carlo

The Monte Carlo processes included in the background model are listed in Tab. 5.3, the corresponding dataset definition names can be found in Tab. 5.4. All samples have been generated using ALPGEN+PYTHIA, except for the diboson and upsilon samples, which are PYTHIA only. Duplicate events, and events with zero luminosity information are removed.

Since the Monte Carlo does note take all physics and detector effects into account, some corrections have to be applied to make it consistent with data:

Luminosity Reweighting Data and MC have different luminosity profiles, that is different amounts of events collected/generated at certain instantaneous luminosities. To correctly deal with luminosity effects, a reweighting as a function of the instantaneous luminosity is applied to MC. The maximum weight factor applied is 3.0. The reweightings are provided by the `lumiprofiles` package.

***Z* and *W* p_T reweighting** The shapes of the transverse momentum distributions are slightly off in the W and Z Boson Monte Carlo, and are corrected by applying a reweighting to the MC.

Point	m_0 [GeV]	$m_{1/2}$ [GeV]	$m(\tilde{\chi}_2^0)$ [GeV]	$m(\tilde{\chi}_1^\pm)$ [GeV]	$m(\tilde{\ell}_R)$ [GeV]	$\sigma \times BR(3\ell)$ [pb]
1	77	183	119	116	111	0.4891
2	78	182	118	115	111	0.4800
3	79	181	117	115	111	0.4590
4	80	180	116	114	112	0.4232
5	81	180	116	114	113	0.3917
6	82	179	116	113	113	0.3458
7	83	178	115	112	114	0.2826
8	102	211	143	142	135	0.1714
9	103	210	142	141	136	0.1637
10	104	210	142	141	136	0.1556
11	105	209	141	140	137	0.1441
12	106	208	140	139	137	0.1283
13	108	206	139	138	139	0.0245
14	126	240	168	168	160	0.0567
15	128	239	167	167	161	0.0517
16	129	238	166	166	162	0.0482
17	131	236	164	164	163	0.0277

Table 5.2: Properties of the generated signal Monte Carlo samples. For all points, $A_0 = 0$, $\tan\beta = 3$ and $\mu > 0$.

Muon p_T smearing Detector effects on the resolution of the muon p_T measurement are underestimated in Monte Carlo. To fix this, a random smearing is applied to $1/p_T$:

$$\frac{1}{p_T} \to \frac{1}{p_T} + aG_1 + \frac{b\sqrt{\cosh(\eta)}}{p_T}G_2\,, \tag{5.1}$$

where G_1 and G_2 are Gaussian distributed with a mean of 0 and a width of 1.

Muon ID and track matching efficiencies The efficiencies of muon and track identification as well as track matching are different in Monte Carlo and in data, and have to be corrected in Monte Carlo.

JES Jets are corrected by the jet energy scale (JES), and jet shifting, smearing and removal (JSSR) is applied.

5.4.1 Normalization of Monte Carlo

After all corrections are applied, the overall normalization of the Monte Carlo samples is adjusted to correspond to the luminosity of the data sample. Since the trigger efficiencies for the `MU_MegaOR` trigger list are not known, a scale factor is derived from comparing data to Monte Carlo in an opposite sign selection around the Z-peak. The S selection (as defined in the next section) is applied, but with an opposite sign instead of a likesign requirement. The

Process	N_{evts}	$\sigma\times$ BR [fb]
$\gamma^*/Z \to \mu\mu$		
15–75 GeV	3.2M	188.5
75–130 GeV	2.8M	394.7
130–250 GeV	0.9M	1.378
250–1960 GeV	1.8M	0.119
$\gamma^*/Z \to \tau\tau$		
15–75 GeV	2.9M	389.7
75–130 GeV	2.7M	185.1
130–250 GeV	0.9M	1.431
250–1960 GeV	1.6M	0.118
$\gamma^*/Z + b\bar{b}$		
15–75 GeV	0.37M	7.858×10^{-3}
75–130 GeV	0.36M	7.185×10^{-3}
130–250 GeV	0.18M	6.129×10^{-3}
250–1960 GeV	0.55M	0.620×10^{-3}
$\gamma^*/Z + c\bar{c}$		
15–75 GeV	0.37M	5.440
75–130 GeV	0.17M	1.761
130–250 GeV	0.34M	14.77×10^{-3}
250–1960 GeV	0.55M	1.324×10^{-3}
$W \to \ell\nu$	60.5M	6214
$W + b\bar{b} + n\text{lp}$	3.0M	16.02
$W + c\bar{c} + n\text{lp}$	2.7M	46.0
Diboson (WW, WZ, ZZ)	1.89M	16.2
$t\bar{t} \to b\bar{b} + 4\text{lpc}$	1.53M	2.43
$t\bar{t} \to b\bar{b} + 2\ell\nu$	1.49M	2.45
$t\bar{t} \to b\bar{b} + \ell\nu + 2\text{lpc}$	1.56M	0.62

Table 5.3: List of all Monte Carlo samples included in the background model. The Z and W samples are composed of subsamples with different numbers of light partons. The listed number of events is the sum of all subsamples, $\sigma \times BR$ is the total NLO cross section times the branching ratio into the final state given in the first column.

Process	Dataset definition
$\gamma^*/Z \to \mu\mu$	
15–75 GeV	CSG_alpgenpythia_gamz_mumu_15_75_p211100_v3
75–130 GeV	CSG_alpgenpythia_gamz_mumu_75_130_p211100_v3
130–250 GeV	CSG_alpgenpythia_gamz_mumu_130_250_p211100_v3
250–1960 GeV	CSG_alpgenpythia_gamz_mumu_250_1960_p211100_v3
$\gamma^*/Z \to \tau\tau$	
15–75 GeV	CSG_alpgenpythia_gamz_tautau_15_75_p211100_v3
75–130 GeV	CSG_alpgenpythia_gamz_tautau_75_130_p211100_v3
130–250 GeV	CSG_alpgenpythia_gamz_tautau_130_250_p211100_v3
250–1960 GeV	CSG_alpgenpythia_gamz_tautau_250_1960_p211100_v3
$\gamma^*/Z + b\bar{b}$	
15–75 GeV	CSG_alpgenpythia_gamz+2b_mumu+2b_15_75_p211100_v3
75–130 GeV	CSG_alpgenpythia_gamz+2b_mumu+2b_75_130_p211100_v3
130–250 GeV	CSG_alpgenpythia_gamz+2b_mumu+2b_130_250_p211100_v3
250–1960 GeV	CSG_alpgenpythia_gamz+2b_mumu+2b_250_1960_p211100_v3
$\gamma^*/Z + c\bar{c}$	
15–75 GeV	CSG_alpgenpythia_gamz+2c_mumu+2c_15_75_p211100_v3
75–130 GeV	CSG_alpgenpythia_gamz+2c_mumu+2c_75_130_p211100_v3
130–250 GeV	CSG_alpgenpythia_gamz+2c_mumu+2c_130_250_p211100_v3
250–1960 GeV	CSG_alpgenpythia_gamz+2c_mumu+2c_250_1960_p211100_v3
$W \to \mu\nu$	CSG_alpgenpythia_w_lnu_p211100_v3
$W + b\bar{b} + n\text{lp}$	CSG_alpgenpythia_w+2b_lnu+2b_p211100_v3
$W + c\bar{c} + n\text{lp}$	CSG_alpgenpythia_w+2c_lnu+2c_p211100_v3
Diboson (WW, WZ, ZZ)	CSG_pythia_diboson_incl_p211100_v3
$t\bar{t} \to b\bar{b} + 4\text{lpc}$	CSG_alpgenpythia_t+t_2b+4lpc_m172_p211100_v3
$t\bar{t} \to b\bar{b} + 2\ell\nu$	CSG_alpgenpythia_t+t_2l+2nu+2b_m172_p211100_v3
$t\bar{t} \to b\bar{b} + \ell\nu + 2\text{lpc}$	CSG_alpgenpythia_t+t_lnu+2b+2lpc_m172_p211100_v3

Table 5.4: List of all background Monte Carlo samples, with SAM dataset names.

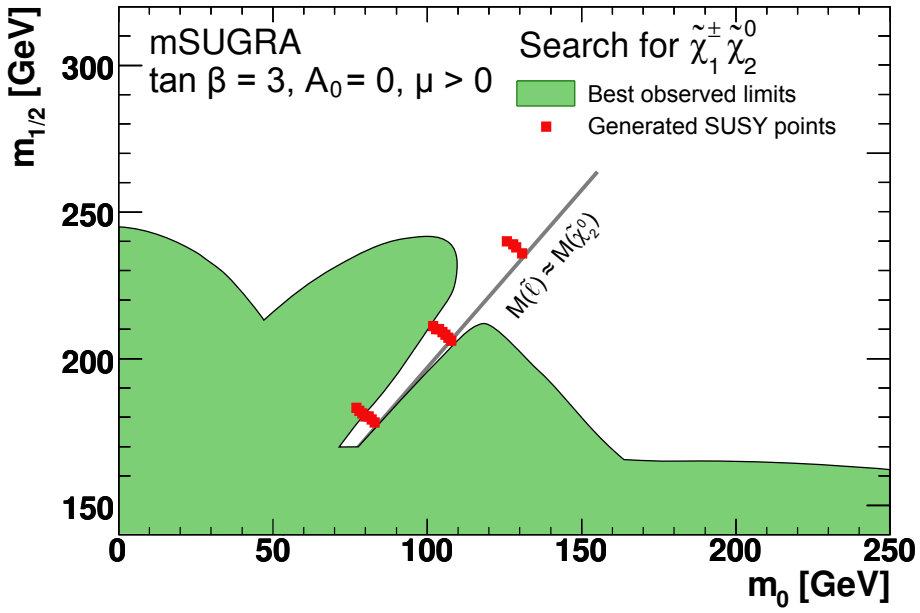

Figure 5.1: Location of the generated SUSY points in the $m_0/m_{1/2}$ plane, in comparison with the previous best observed limits. All points are near the line of $M(\tilde{\ell}) = M(\tilde{\chi}_2^0)$, where the analyses using the trilepton final state have a reduced sensitivity, because the third lepton can be very soft.

cuts 75 GeV $< M_{\mu\mu} <$ 130 GeV and $p_{T1} > 15$ GeV $\wedge$ $p_{T2} > 10$ GeV are added to increase the fraction of $Z \to \mu\mu$ events, and to suppress the multijet background. The result is shown in Fig. 5.2. The ratio of data and MC distributions is flat, and the fitted value is 0.9421 ± 0.0038.

5.5 Event Selection

First, a common set of criteria is applied to all muons. A "good" muon is defined as:

- Transverse momentum $p_T > 5$ GeV.
- Must be in the acceptance range of the muon system $|\eta_{\text{det}}|, 2.0$.
- Muon quality: loose.
- Track quality: trackmedium.
  - Muon must have a matched central track with $\chi^2 < 4$.
  - Distance of closest approach to primary vertex < 0.2 cm (0.02 cm if there is an SMT hit).
- Muon must pass anti-cosmic cuts (time between scintillator hits must be in a ± 10 ns window around the predicted times).
- $|\Delta z|$ between muon and primary vertex < 1 cm.
- Number of CFT hits on matched track $N_{\text{CFT}} \geq 7$

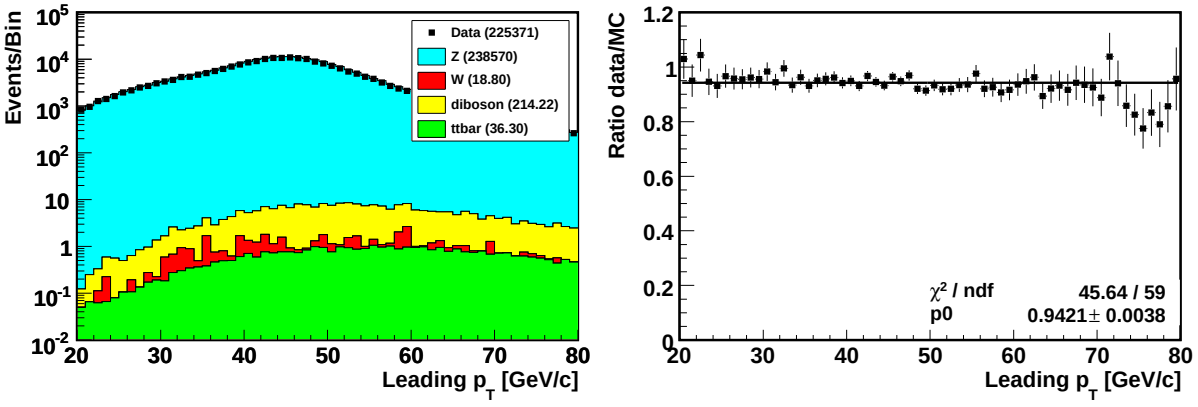

Figure 5.2: Determination of the relative Monte Carlo normalization. Left: Comparison of data and Monte Carlo (unscaled), opposite-sign sample, using the selection S. Right: Ratio of data and Monte Carlo in the opposite sign sample. A constant of 0.9421 ± 0.0038 is fit to the ratio.

All events which are considered must have at least two muons fulfilling this criteria. Muons are further classified by their isolation:

- A tightly isolated muon satisfies etTrkCone5<2.5 GeV/c and etHalo<2.5 GeV.
- A loosely isolated muon is not tight, and has etTrkCone5<4.0 GeV.
- If a muon fails both the loose and tight criteria, it is called non-isolated.

The definitions of etTrkCone5 and etHalo are given in section 4.3.3. Events with one tightly isolated muon, and one loose or tight muon of same sign are in selection S. Events with one tightly isolated muon, and one likesign muon failing loose isolation are in the selection Q.

The determination of the QCD reweighting function $R(p_T)$ is done in the region $p_T < 8$ GeV, where the QCD multijet background is dominating.

The search is performed in the S sample, in the region $p_{T1} > 15$ GeV and $p_{T2} > 10$ GeV. Here, p_{T1} is the leading (highest) p_T muon of the pair, and p_{T2} is the second muon. This selection is called the preselection in the following.

6 Background estimation

6.1 QCD Multijet Background

While most other standard model backgrounds are modeled with Monte Carlo simulations, a data-driven approach is used to estimate the QCD multijet background. This is due to a number of inherent difficulties in simulating QCD with Monte Carlo:

- Since the coupling constant of QCD α_s becomes large at low energies, it is not possible to treat QCD fully perturbatively. Heuristic models exist for the non-perturbative part (hadronisation), but these typically don't reproduce higher-order effects. This is especially the case when the perturbative calculations are only done in leading order (LO).

- In particular, data and MC disagree in angular distributions such as $\Delta\phi$ between jets. This is, among other reasons, due to the process $g \to b\bar{b}$ not being simulated properly.

- Also, the uncertainties on the $b\bar{b}$ cross section – and thus on the normalization of multijet Monte Carlo – are quite large, due to a difference between theoretical predictions and experimental results.

- Because $b\bar{b}$ has a large cross section, it is important to have a large number of simulated likesign dimuon events from that process. However, the small branching ratio to the final state makes it computationally very expensive to generate enough events.

In this section, the method for modeling the QCD multijet background from data will be presented.

6.1.1 Properties of the QCD Multijet Background

Multijet events can be distinguished from signal and other background events by their different event topology. While muons in multijet events are emitted from jets, signal muons come from slepton and gauge boson decays. This leads to the following characteristics:

- Multijet muons tend to be non-isolated, and are usually found inside the accompanying jet. However, the muon can radiate a photon and be recoiled out of the jet. The probability for this is higher, the lower the muon momentum is. Signal muons on the other hand tend to be isolated, unless an jet from a different process accidentally lies in the same area (see Fig. 6.1(a)).

- The angles of the likesign muons are correlated. The muons tend to be back-to-back. The angles of signal muons are not correlated, since both come from different branches of the decay cascade (Fig. 6.2).

- The p_T spectrum of multijet muons peaks at low values (Fig. 6.1(b), right).

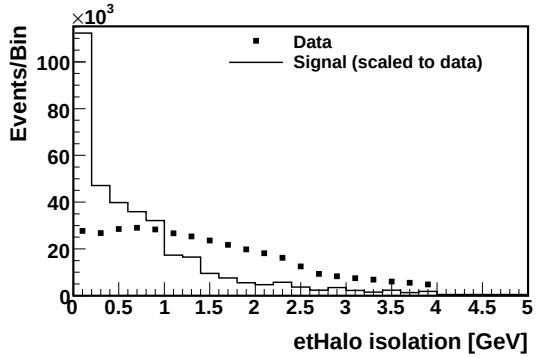

(a) Isolation properties of signal vs. overall data, S selection. The signal has been scaled to have the same integral as data. etHalo is defined as the energy deposited in a hollow cone of $\Delta R = 0.1 \ldots 0.5$ around the muon.

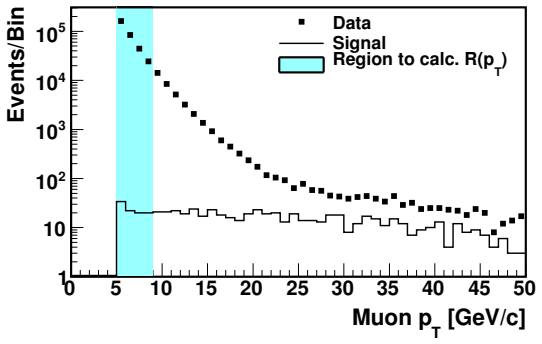

(b) Transverse momentum distributions of signal vs. overall data. While the signal distribution is comparatively flat, data peaks at low p_T, mainly due to QCD multijet background. Shaded in blue is the region where the $R(p_T)$ reweighting is calculated.

Figure 6.1: Kinematic properties of signal vs. data. SUSY parameters used for the signal are $m_0 = 80$ GeV/c^2, $m_{1/2} = 180$ GeV/c^2, $A_0 = 0$, $\tan\beta = 3$ and $\mu > 0$.

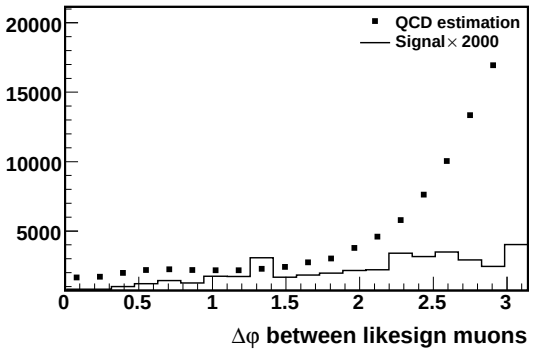

Figure 6.2: $\Delta\varphi$ (angle in the transverse plane) between the two likesign muons, for the QCD estimation, and for signal.

6.1.2 Procedure

The differences in isolation distributions cannot be used to simply cut the QCD background away, but they can be used to get leverage on the background to model it. This is done by the following procedure.

Starting with pairs of good muons as defined in Sec. 5.5, a QCD enriched sample Q is defined. One muon must be tight, and one muon of same sign must fail the loose criterion (non-loose). A signal or selection sample S is defined similarly with one tight muon, and one same sign muon either tight or loose.

With these definitions, the ratio of the number of muons in S over the number of muons in Q is related to the probability for a non-loose muon to gain at least loose isolation, given that the other muon is tight. At least one muon in each event is tightly isolated. The p_T of the other muon is used to parametrize R. Since in the S sample, both muons can be tight, and they cannot

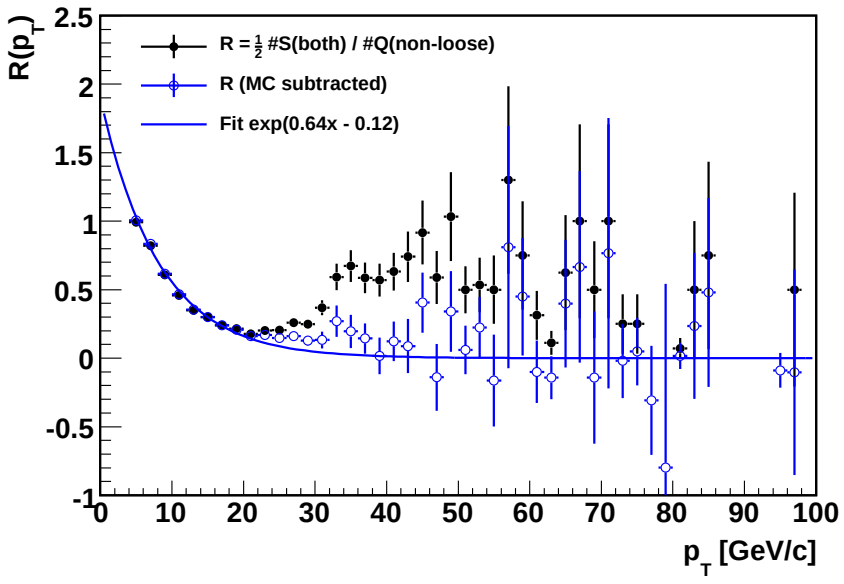

Figure 6.3: Functional form of the reweighting function $R(p_T)$. The ratio R is defined as half the number of muons in the S sample, divided by the number of non-isolated muons in the Q sample. The data points with full circles show $R(p_T)$ calculated from data. These follow an exponential function only below $p_T = 20$ GeV, because above, the multijet background is no longer dominant. For the points with open circles, a Monte Carlo estimation of the other backgrounds (W + jets, Z + jets, diboson and $t\bar{t}$) has been subtracted from the S and Q histograms before calculating the ratio, which agrees better with the exponential form.

always be distinguished, both muons will be counted, and the result divided by two:

$$R(p_T(i)) = \left.\frac{\#\mathrm{S}^{\mathrm{both}}}{2 \cdot \#\mathrm{Q}^{\text{non-}}_{\text{loose}}}\right|_{p_T(i)} \tag{6.1}$$

Here, the muons are histogrammed – both muons of S and the non-loose muon of Q. $\#\mathrm{S}^{\mathrm{both}}$ denotes the number of muons in the S sample in the bin $p_T(i)$, $\#\mathrm{Q}^{\text{non-}}_{\text{loose}}$ the number of non-loose muons in the Q sample in the corresponding bin. The ratio $R(p_T)$ is shown in Fig. 6.3. Since the shape of the multijet momentum distribution is approximately a falling exponential, in absence of other processes the ratio should be an exponential, too. In a kinematic region where other backgrounds than QCD multijet are negligible, the ratio can be fitted with $R(p_T) = \exp(a \cdot p_T + b)$.

The function $R(p_T)$ is used to reweight the Q sample – each event in the Q sample is assigned a weight of $R(p_T)$, depending on the transverse momentum of the non-loose muon. The resulting sample consists mainly of QCD multijet events (like in Q), but with kinematic distributions similar to the S sample. As such, it can serve as an estimation of the QCD multijet background in S. Different $R(p_T)$ curves are derived for different values of the jet multiplicity N_{jets}. This especially improves the agreement of data and background in MET distributions.

The fit must be performed in a region which is later removed from the selection, to avoid bias. In this analysis, it is done in a region of low transverse momentum, between 5 and 8 GeV/c, and then extrapolated to higher p_T. The trigger efficiencies are not known precisely in this region, so it is cut later anyway when comparing data with Monte Carlo. For the determination of $R(p_T)$ this is not an issue, as efficiencies cancel out when calculating the ratio.

N_{Jets}	Slope a	Constant b
0	-0.068 ± 0.009	1.193 ± 0.053
1	-0.085 ± 0.013	-0.081 ± 0.074
2	-0.147 ± 0.023	-0.672 ± 0.141
3	-0.189 ± 0.046	-0.719 ± 0.281
≥ 4	-0.145 ± 0.091	-1.4 ± 0.6

Table 6.1: Parametrization of the reweighting function $R(p_T) = \exp(a \cdot p_T + b)$. The parameters were determined using the selection $p_{T1} < 8$ GeV/c and $p_{T2} < 8$ GeV/c.

Furthermore, a region is needed where the QCD multijet background is dominant – ideally the only source of background – in the Q sample. A higher upper p_T bound quickly increases contributions from electroweak (non-QCD) processes, which were assumed to be negligible.

Figure 6.7 shows plots of the S/Q ratio, and the fitting of $R(p_T)$, for $N = 0, \ldots, 3$ and $N >= 4$ jets. The determined parameters are shown in Tab. 6.1.

6.1.3 Systematic uncertainty

A systematic uncertainty is introduced through the parametrization of the reweighting function $R(p_T)$. Each of the ten parameters (slope and constant for each of the 5 jet multiplicity bins) has an uncertainty (Tab. 6.1) which in approximation is assumed to be Gaussian. In 10000 pseudo-experiments, the parameters are chosen randomly from their Gaussian distributions, and the integral of the resulting multijet background estimation is determined. The distribution of integrals is shown in Fig. 6.4. A Gaussian is fitted to the distribution, and found to have a mean of $\mu = 193.3 \times 10^3 \pm 102$ and a standard deviation of $\sigma = 9973 \pm 72$. This translates into a systematic uncertainty of ±5.16%.

6.1.4 Electroweak Contamination

The QCD estimation procedure described above alone does not provide good agreement between data and background when the Monte Carlo for other processes is included. Figure 6.5(a) shows the leading p_T and missing transverse energy for backgrounds vs. data. A slight overestimation of the background at higher transverse momentum is visible. The reason is that, while the multijet background is dominant in the low p_T region where $R(p_T)$ is calculated, it is not dominant at higher p_T. In this region, there is a significant contribution from other processes. Since the Q sample is defined to have one tightly isolated and one non-isolated muon, this electroweak contamination is especially caused by W+jets. Image 6.5(b) shows a pure electroweak sample from Monte Carlo, to which the selection Q has been applied. The resulting sample Q^{MC} is a model for the electroweak contamination of Q. This sample Q^{MC} is reweighted with $R(p_T)$ as well, and then subtracted from the QCD estimation when building histograms. This results in corrected QCD multijet distributions, as seen in Fig. 6.5(c).

Electroweak subtraction scale factor

The reweighted Q^{MC} sample serves as an estimation for the electroweak contamination in the reweighted Q sample, however as can be seen in Fig. 6.6(a), there is an excess in Q^{MC} over Q. This is due to the fact that the selection efficiencies are different in the S and Q samples with

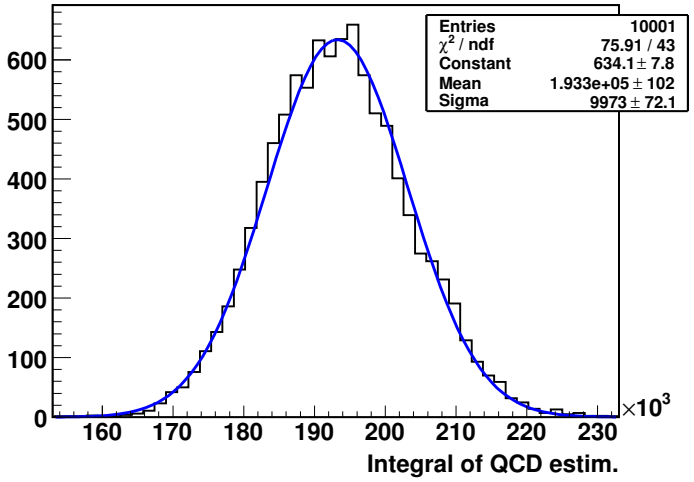

Figure 6.4: Determination of the systematic uncertainty of the QCD multijet background. The parameters a and b of the reweighting function $R(p_T) = \exp(ax + b)$ are chosen randomly from Gaussian distributions, and the integral of the QCD background is calculated. This is repeated 10000 times, and the resulting distribution is fitted with a Gaussian.

their different isolation criteria. To correct the normalization of the electroweak contamination, a scale factor is derived using the leading p_T distribution. The genuine multijet background peaks at low values, and approaches zero towards high p_T, such that W+jets and other electroweak backgrounds are more prevalent at higher values. Since the reweighted Q^{MC} sample is to be subtracted from the reweighted Q sample, it should not exceed the latter (except for fluctuations). In the high p_T region, the difference of both samples should go to zero on average. Figure 6.6(b) shows the ratio of the reweighted Q and Q^{MC} samples. A fit of a constant to the ratio in the region $p_{T1} > 65$ GeV/c yields a scale factor of 0.753 ± 0.085. After scaling the Q^{MC} sample by this factor, the corrected multijet estimation should be positive in most regions. In bins where it is negative due to fluctuations, the count is set to zero.

Although the electroweak subtraction procedure improves the accuracy of the multijet modeling, it introduces a new source of systematic uncertainty. The uncertainty of the electroweak subtraction scale factor is about 12%. At preselection stage ($p_{T1} > 15$ GeV, $p_{T2} > 10$ GeV), there are 653.7 events in the reweighted Q sample, and 227.7 events in the reweighted Q^{MC} sample (scale factor applied). A variation of the scale factor by ±12% changes the corrected QCD estimation by 9%.

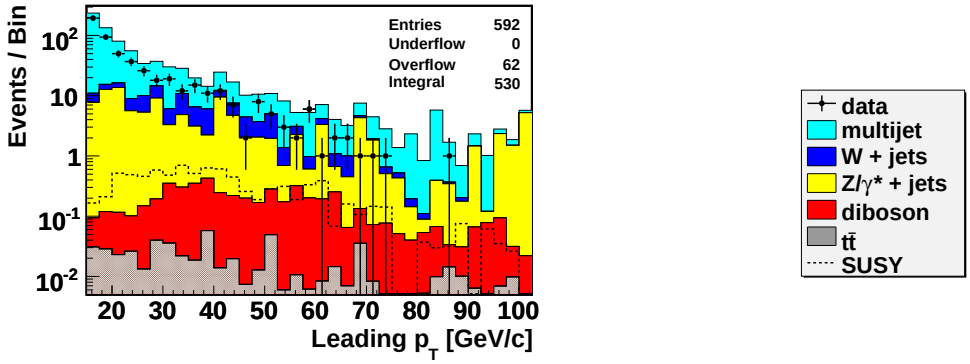

(a) Comparison of data and all backgrounds in the preselection ($p_{T\,1} > 15$ GeV, $p_{T\,2} > 10$ GeV). There is a visible excess of background due to electroweak contamination of the multijet estimation.

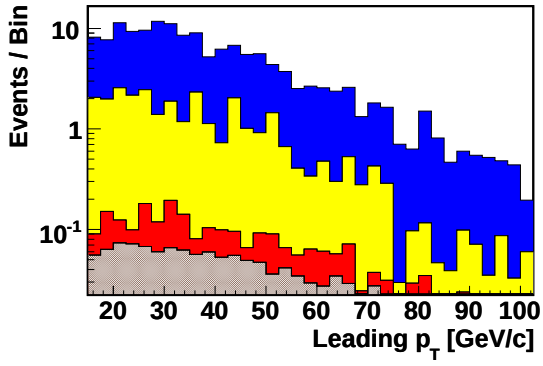

(b) Composition of the sample Q^{MC}. The Q selection is applied to each Monte Carlo sample, and then it is reweighted with $R(p_T)$. The result is an estimation of the electroweak contamination.

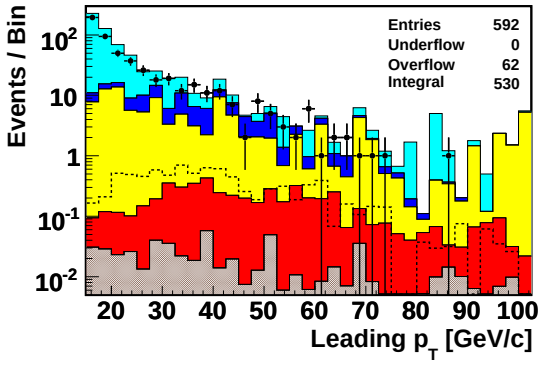

(c) Comparison of data and backgrounds with the corrected multijet estimation (Q^{MC} subtracted). The agreement is much better.

Figure 6.5: Subtraction of electroweak contamination from QCD multijet estimation.

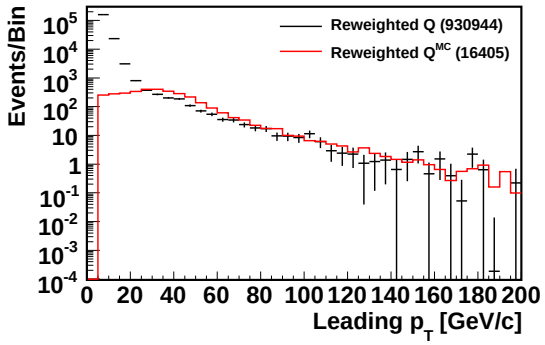

(a) The reweighted Q^{MC} sample which is to be subtracted from the reweighted Q sample exceeds the latter in some regions, leading to a negative multijet estimation.

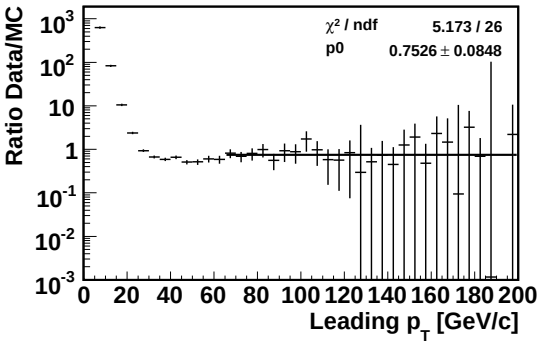

(b) A scale factor is derived from the requirement that in mean Q^{MC} shall not exceed Q, and that for high p_T the amount of multijet background shall approach zero. The determined factor is 0.753 ± 0.085.

Figure 6.6: Determination of the scale factor for electroweak subtraction.

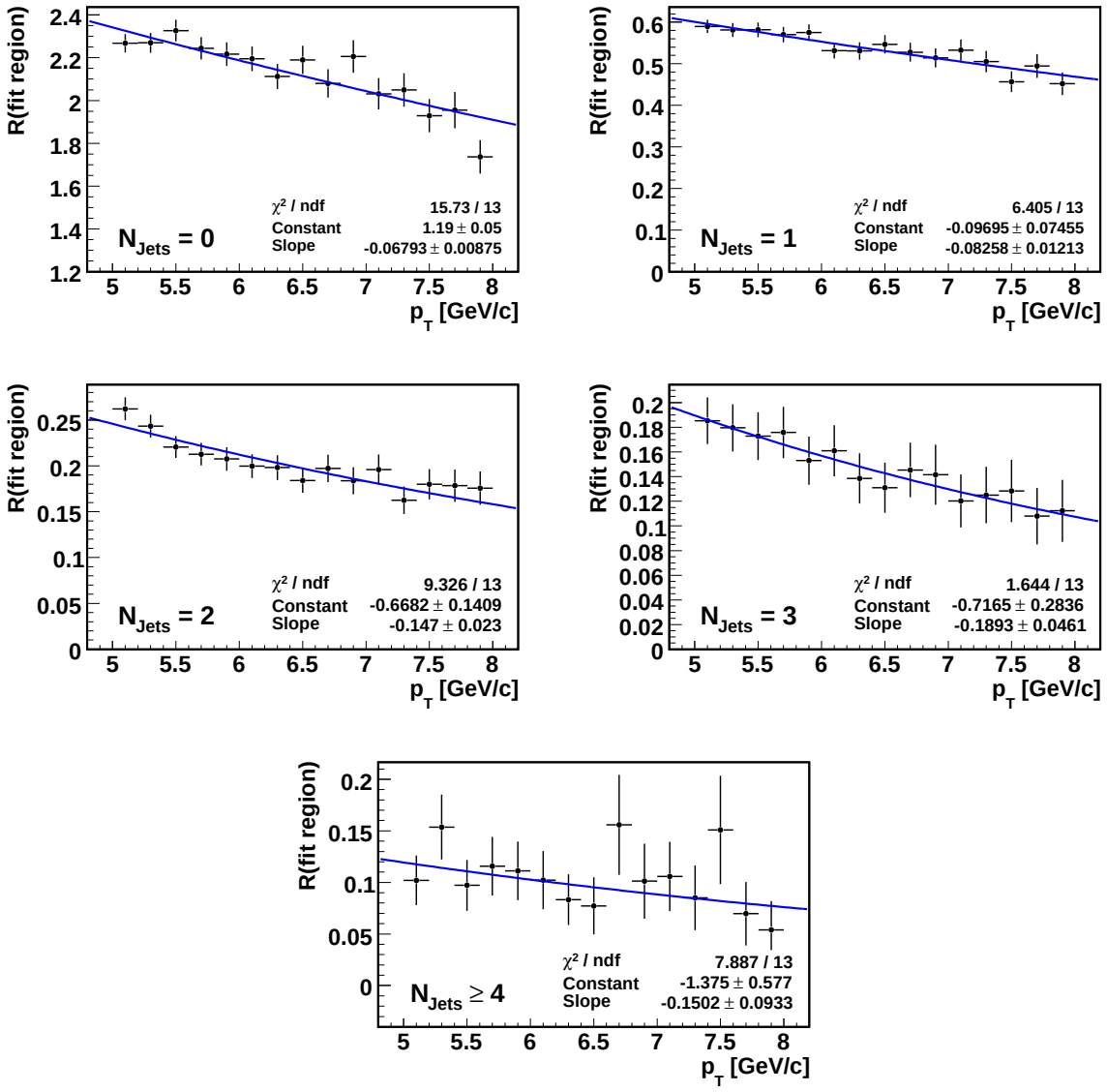

Figure 6.7: Determination of $R(p_T)$. The reweighting function is fit to the ratio R in the region $p_T < 8$ GeV. A different reweighing is derived for each jet multiplicity ($N_{\text{jets}} = 1 \ldots 3$, $N_{\text{jets}} \geq 4$.

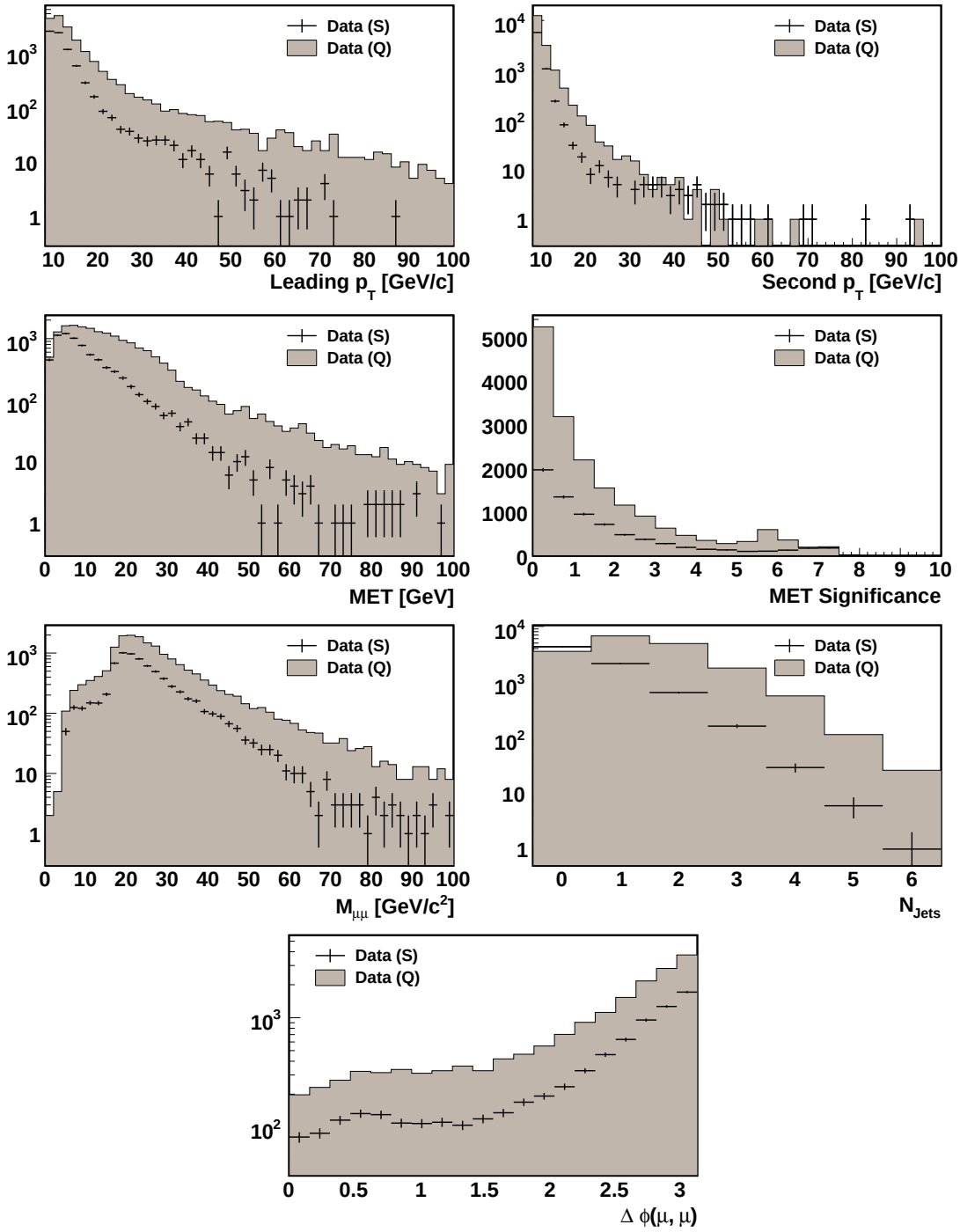

Figure 6.8: Comparison of the S and Q samples in the preselection. Before applying the reweighting to Q, neither the normalization nor the shapes of distributions agree.

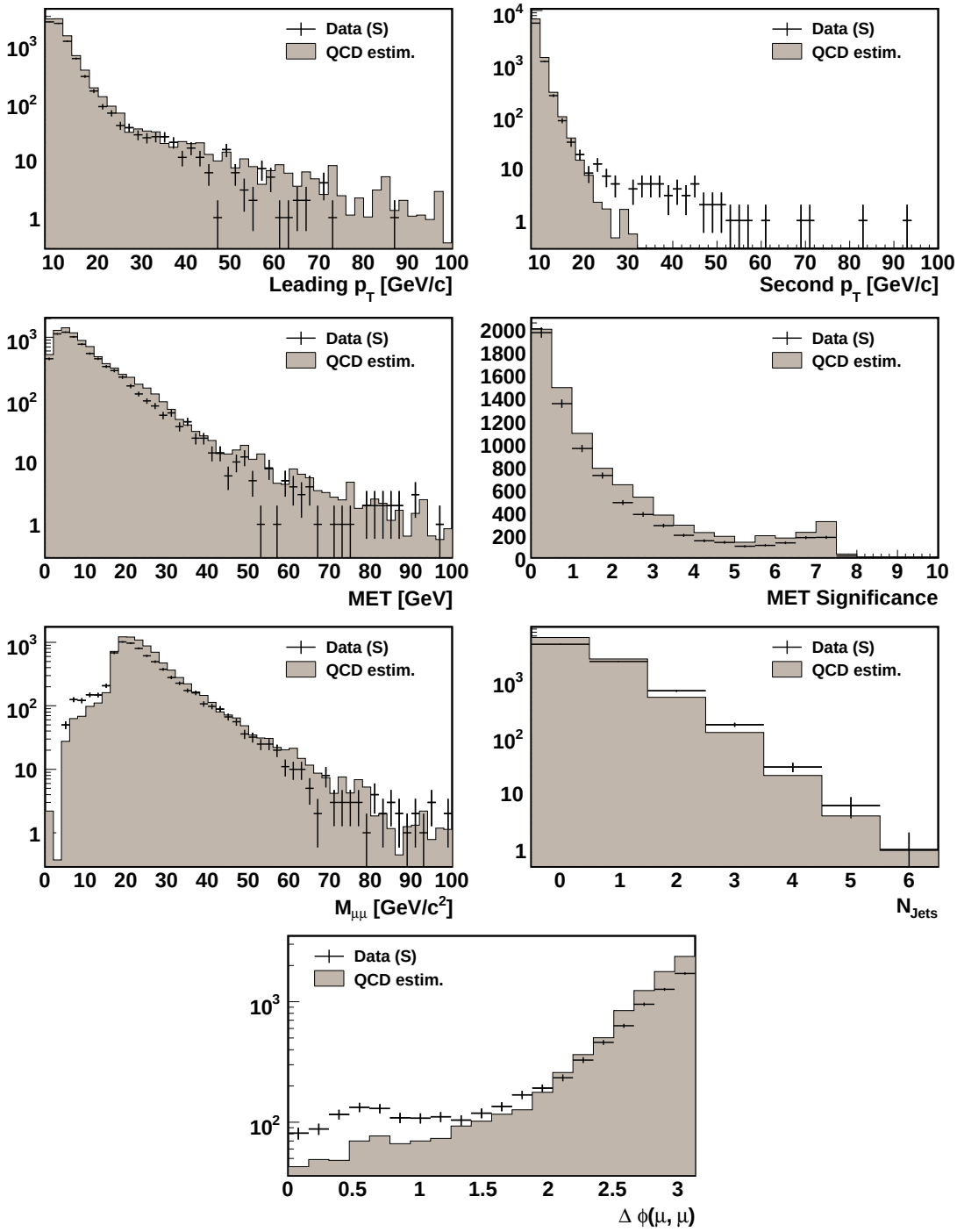

Figure 6.9: Comparison of the S sample and the Q sample with the $R(p_T)$ reweighting applied. The agreement is better than in Fig. 6.8, however the estimation of the multijet background exceeds the data in some regions. This is due to "contamination" of the Q sample from other processes, which is removed in the next step.

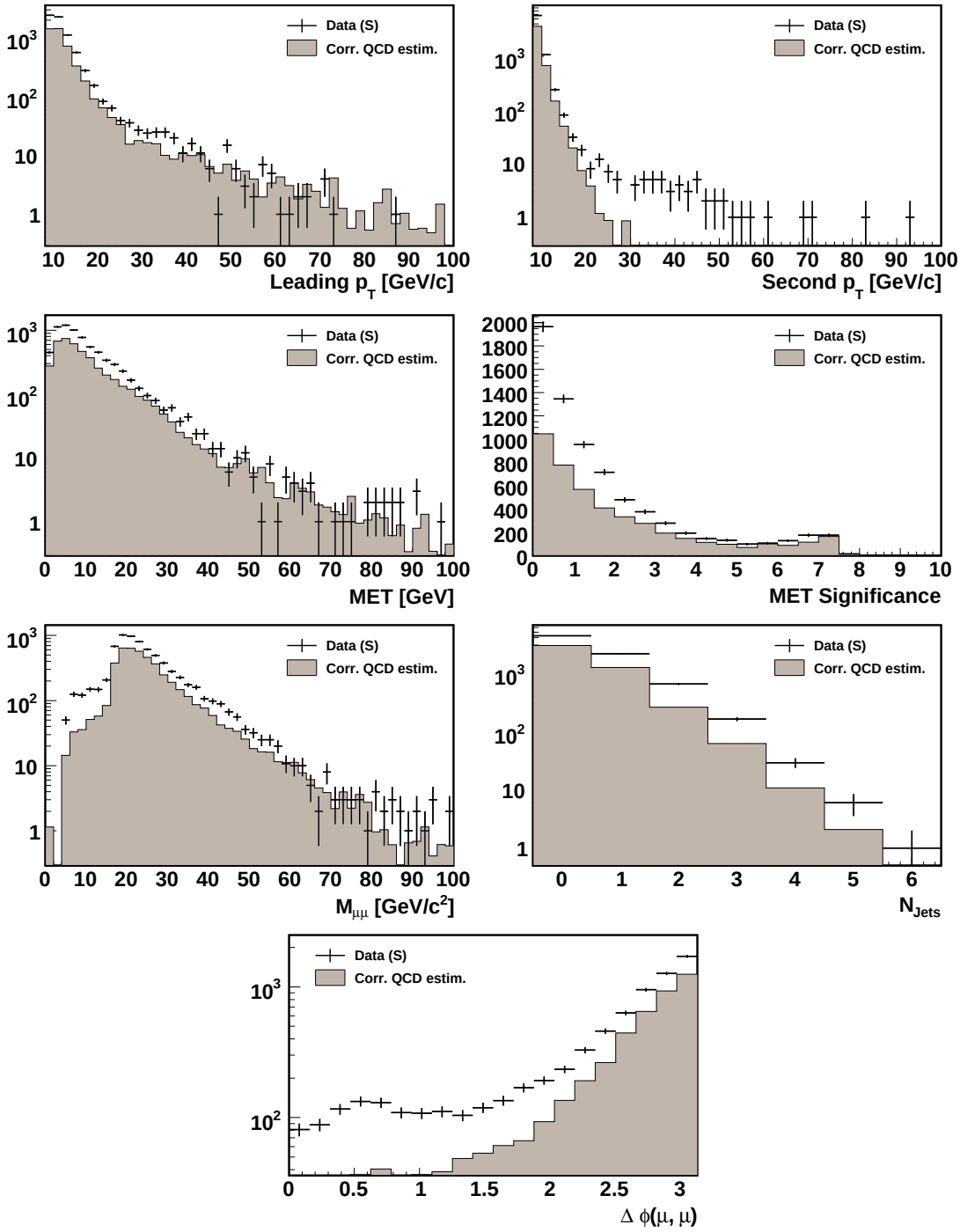

Figure 6.10: Comparison of the S sample and the corrected multijet background estimation. The multijet background is obtained by applying the $R(p_T)$ reweighting to the Q sample, and subtracting the background from electroweak processes (diboson, Z+jets, W+jets, $t\bar{t}$).

6.2 Charge Flip

A major instrumental background is due to the mismeasurement of muon charges, or charge flip (CF), leading to the false identification of opposite sign events as likesign. Two factors contribute to this:

- The probability of a charge mismeasurement increases with higher muon momentum, since the charge is determined from the direction of curvature of the track, $\mathrm{sgn}(1/p_T)$. When the track is nearly straight, $1/p_T \approx 0$, and the uncertainty in the measurement can flip the sign of curvature, and the muon charge.
- Higher instantaneous luminosity also increases the charge flip rate. As the occupancy of the tracker grows, spurious hits can cause track misidentification.

The single biggest source of charge flip background is from the Drell-Yan process, $\gamma/Z \to \mu^+\mu^-$ mismeasured as likesign. Other possible sources are:

- Decay of resonances into opposite sign muon pairs, such as $\Upsilon \to \mu^+\mu^-$. This only plays a role at low p_T, where it is likely to be cut away, and the charge flip rate is low.
- Top quark pair production, leading to two muons and jets ($t\bar{t} \to \mu^+\mu^- + \nu\bar{\nu} + b\bar{b}$), and similar processes. The contribution of this is negligible compared to Drell-Yan.
- W + jets, with one muon from the W Boson and one from a jet, e.g. $W^+ + \mathrm{j} \to \mu^+ + \mu^\pm + \cdots$. An equal number of events are flipped from opposite sign to same sign, and vice-versa. Although charge mismeasurement occurs here, it does not contribute to the background.
- QCD multijet events are also symmetric with regard to charge flip, and do not contribute.

6.2.1 Estimation Method

To estimate the charge flip content of a given sample, a method described in [28] is used. The idea is to compare two independent measurements of the muon charge. The probability that these two measurements disagree can be related to the probability that the charge is mismeasured. The first value Q_{trk} is obtained from the central track. This central charge is the conventionally used measurement, and is meant when simply is referred to the muon "charge". The second measurement Q_{loc} is made with the muon system, and called local charge. It is less reliable than the central charge, because measurements of track curvature have a lower resolution in the muon system than in the tracking system. Both measurements are independent, since the magnetic fields in the central tracker and in the muon system are perpendicular.

The likesign sample consists of two types of events: "true" likesign events, and "flip" events, where one muon of the pair has a mismeasured charge. The numbers of true and flip events, N_{true} and N_{flip} are unknown and to be determined. What can be counted is the number of events where the two measurements give the same result for both muons N_{SS} (same-same), agree for one and disagree for the other, N_{SO} (same-opposite), or disagree for both muons, N_{OO} (opposite-opposite). The probability for an event to appear as SS, SO or OO if it is a true or a flip event is given by P_J^{true} or P_J^{flip}, respectively ($J = \mathrm{SS}, \mathrm{SO}, \mathrm{OO}$). The number of events of each type is given by:

$$\begin{aligned} N_{\mathrm{SS}} &= P_{\mathrm{SS}}^{\mathrm{true}} \cdot N_{\mathrm{true}} + P_{\mathrm{SS}}^{\mathrm{flip}} \cdot N_{\mathrm{flip}} \\ N_{\mathrm{SO}} &= P_{\mathrm{SO}}^{\mathrm{true}} \cdot N_{\mathrm{true}} + P_{\mathrm{SO}}^{\mathrm{flip}} \cdot N_{\mathrm{flip}} \\ N_{\mathrm{OO}} &= P_{\mathrm{OO}}^{\mathrm{true}} \cdot N_{\mathrm{true}} + P_{\mathrm{OO}}^{\mathrm{flip}} \cdot N_{\mathrm{flip}} \end{aligned} \tag{6.2}$$

The case where both muons are mismeasured is rare, and therefore neglected here. The probabilities for the different numbers of (dis)agreements, P_J^{true} and P_J^{flip}, depend on ε_{loc}, the fraction of correct charge measurements of the muon system.

$$\begin{aligned}
P_{\text{SS}}^{\text{flip}} &= \tfrac{1}{2}\left[\varepsilon_1^{\text{true}}(1-\varepsilon_2^{\text{flip}}) + \varepsilon_2^{\text{true}}(1-\varepsilon_1^{\text{flip}})\right] \\
P_{\text{SO}}^{\text{flip}} &= \tfrac{1}{2}\left[\varepsilon_1^{\text{true}}\varepsilon_2^{\text{flip}} + (1-\varepsilon_1^{\text{true}})(1-\varepsilon_2^{\text{flip}}) + \varepsilon_1^{\text{flip}}\varepsilon_2^{\text{true}} + (1-\varepsilon_1^{\text{flip}})(1-\varepsilon_2^{\text{true}})\right] \\
P_{\text{OO}}^{\text{flip}} &= \tfrac{1}{2}\left[\varepsilon_1^{\text{flip}}(1-\varepsilon_2^{\text{true}}) + \varepsilon_2^{\text{flip}}(1-\varepsilon_1^{\text{true}})\right] \\
P_{\text{SS}}^{\text{true}} &= \varepsilon_1^{\text{true}}\varepsilon_2^{\text{true}} \\
P_{\text{SO}}^{\text{true}} &= \varepsilon_1^{\text{true}}(1-\varepsilon_2^{\text{true}}) + \varepsilon_2^{\text{true}}(1-\varepsilon_1^{\text{true}}) \\
P_{\text{OO}}^{\text{true}} &= (1-\varepsilon_1^{\text{true}})(1-\varepsilon_2^{\text{true}})
\end{aligned} \tag{6.3}$$

Here, the lower index on ε distinguishes the two muons. Each can have a different efficiency, since ε_{loc} is parametrized by muon p_T. The upper index gives the precondition: true if the muon charge has been measured correctly by the central tracker, flip otherwise. For example, $\varepsilon_2^{\text{flip}}$ is the fraction of correct local charge measurements at the p_T of the second muon, given that the charge has been mismeasured in the tracker. It is assumed that $\varepsilon_i^{\text{flip}}$ and $\varepsilon_i^{\text{true}}$ are the same.

To determine the number of CF events in the sample, each equation in (6.2) is summed over all events, and divided by the total number of events, $N_{\text{evts}} = N_{\text{true}} + N_{\text{flip}}$:

$$\begin{aligned}
&\frac{1}{N_{\text{evts}}}\sum_{\text{evts}} N_{\text{SS}} = \frac{1}{N_{\text{evts}}}\sum_{\text{evts}}(P_{SS}^{\text{true}}N_{\text{true}} + P_{SS}^{\text{flip}}N_{\text{flip}}) \\
\Rightarrow \quad & N_{\text{SS}} = (1-f_{\text{flip}})\sum_{\text{evts}} P_{SS}^{\text{true}} + f_{\text{flip}}\sum_{\text{evts}} P_{SS}^{\text{flip}}
\end{aligned} \tag{6.4}$$

with the flip fraction $f_{\text{flip}} := N_{\text{flip}}/N_{\text{evts}}$. The probabilities given by equations (6.3) are calculated on an event-by-event basis, and summed up. Now the three equations of type (6.4) are each solved for f_{flip}. Since the system of equations is overdetermined, this yields three solutions, of which the weighted average is taken. The flip fraction determined this way is multiplied with the total number of events to get the number of charge flip events in the analyzed sample.

The efficiency of the local charge measurement, ε_{loc}, is determined from an opposite sign sample with the selection S. Muon pairs in the invariant mass range 75 GeV $< m_{\mu\mu} <$ 105 GeV are selected to get a clean dimuon sample. All muons are required to have a local charge measurement. The fraction of muons with equal local and central charge is determined in dependence of p_T^-1, and fitted with the function $1 - 1/(2 + p_0/p_T)$ (Fig. 6.11). This function was chosen because it approaches 100% efficiency for low p_T, and 50%, meaning the determined charge is arbitrary in the limit of very high p_T. The same procedure was also performed with $\gamma/Z \to \mu\mu$ Monte Carlo, generated with 75 GeV $< m_{\mu\mu} <$ 130 GeV, the same cuts applied as above. The charge measurement efficiency of the muon system is overestimated in Monte Carlo, as can be seen in Fig. 6.11.

Systematic Uncertainty

One source of systematic uncertainty arises from the parametrization of ε_{loc}. This is estimated by varying the parameter p_0 by one standard deviation. The effect on the charge flip estimation at preselection stage is ±2%. A larger effect comes from the fact that the estimations from the three equations (6.2), which are averaged, can vary strongly. This effect is already considered, together with the Poissonian error on the number of events, in the statistical error on the number of charge flips. For the preselection stage, the estimate is 109.6 ± 26.9 charge flip events, which constitutes a 24% uncertainty.

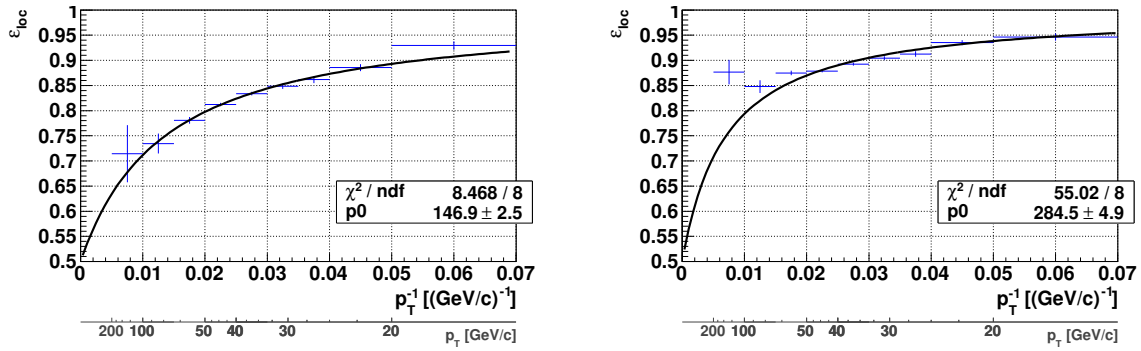

Figure 6.11: Fraction of correct charge measurements in the local muon system for data (left), and $Z \to \mu\mu$ Monte Carlo (right).

7 Cutflow and Results

A series of cuts is applied to the analysis selection to increase the signal over background ratio. In the following, important variables are described:

Leading and next-to leading transverse momentum (p_{T1}, p_{T2}) A lower cut on leading $p_T > 15$ GeV and second $p_T > 10$ GeV is set, because the muon ID efficiencies applied to Monte Carlo are only reliable down to this level. This cut also removes a great deal of QCD multijet background. Upper cuts are applied to remove mainly Z + jets background from signal-free regions.

Missing transverse energy ($\not\!\!E_T$) Signal events are rich in missing E_T, since the final state contains two LSPs and a neutrino. A lower bound serves to reduce the QCD multijet background among others.

Missing E_T significance (Sig($\not\!\!E_T$)) When energy of a jet is mismeasured, this leads to fake missing E_T parallel to the jet. A cut on missing E_T significance is used to distinguish this case from real missing transverse energy. The uncertainty of the jet energy scale projected in the direction of the jet is given by σ_{proj}. The significance of $\not\!\!E_T$ is then:

$$\text{Sig}(\not\!\!E_T) = \frac{E_T}{\sum_{\text{jets}} \sigma^2_{\text{proj}}} \,. \tag{7.1}$$

M_{T1}, M_{T2} These are topological variables which provide a good separation between different processes. M_{T1} is defined as the transverse mass calculated between the leading p_T muon and $\vec{\not\!\!E}_T$. If $\Delta\varphi$ is the angle between $\vec{\not\!\!E}_T$ and the leading p_T muon, then:

$$M_{T1} := \sqrt{2\, \not\!\!E_T\, p_{T1}\, (1 - \cos(\Delta\varphi))} \tag{7.2}$$

M_{T2} is defined with the next-to leading p_T muon, respectively.

$\Delta\varphi$ between both muons For reasons of momentum conservation, muons from the multijet background tend to be back-to-back. Thus a cut $\Delta\varphi < 2.7$ is applied.

$\not\!\!E_T \times p_{T2}$ An upper limit on this variable is effective against background from multijet and W+jets.

The list of applied cuts is given in Tab. 7.1. The following pages show various distributions of data, background and signal for each stage in the cutflow. The shown signal is SUSY point 4, with $m_0 = 80$ GeV/c^2, $m_{1/2} = 180$ GeV/c^2, $A_0 = 0$, $\tan\beta = 3$ and $\mu > 0$. Note that in some distributions, the bin width was chosen variably due to low statistics at high momenta/energies.

The number of data and background events after each cut stage are given in Tab. 7.2, the composition of the background in Tab. 7.3. After applying all cuts, 3 events have been observed in data, which is consistent with $5.4 \pm 4.1(\text{stat}) \pm 0.7(\text{syst})$ events expected from background.

Sel.	Cut
0	$p_{T1} > 15$ GeV and $p_{T2} > 10$ GeV
1	$p_{T1} < 120$ GeV
2	$p_{T2} < 80$ GeV
3	$\not{E}_T > 15$ GeV
4	$M_{T1} > 30$ GeV
5	$\mathrm{Sig}(\not{E}_T) > 6.5$ GeV
6	$\Delta\varphi < 2.7$ GeV
7	$\not{E}_T \times p_{T2} > 700$ GeV
8	$M_{T2} < 85$ GeV

Table 7.1: Succession of cuts applied to data and Monte Carlo samples.

7.1 Systematics

For the calculation of limits, systematic uncertainties from different sources were taken into account. A 6% uncertainty on the luminosity measurement is assumed, as well as a 4% uncertainty from the parton distribution functions (PDFs). The efficiencies for muon identification and track matching have a systematic uncertainty of 3% [22], the jet energy scale one of 1%. The uncertainty from the QCD multijet estimation has been determined by varying the reweighting function in pseudoexperiments, and is taken to 6%. The correction of the multijet estimation through subtraction of the electroweak contamination adds an uncertainty of 9%. The uncertainties of the charge flip estimation are mostly statistical in nature, but there is an additional systematic uncertainty from the parametrization of $\varepsilon_{\mathrm{loc}}$ of 2%. The diboson cross section is known with an uncertainty of 7%, the W+jets cross section with 8.5%. Weighted with their relative contributions to the final selection, this makes an uncertainty of 6.7% for W+jets and 1.6% for diboson.

7.2 Limit Settings

Given the mentioned systematics, the best limits on cross section times branching ratio were calculated for each SUSY point. The expected and observed limits are given in Tab. 7.5. Cross sections above a given observed limit are excluded at 95% CL. The limits are visualized in Fig. 7.1.

Sel.	Data	Background	Signal
0	577.0 ± 24.0	651.0 ± 35.7	13.8 ± 0.9
1	535.0 ± 23.1	613.5 ± 32.5	13.8 ± 0.9
2	534.0 ± 23.1	614.9 ± 32.5	13.8 ± 0.9
3	256.0 ± 16.0	275.3 ± 22.9	12.6 ± 0.8
4	201.0 ± 14.2	197.4 ± 21.0	12.2 ± 0.8
5	64.0 ± 8.0	79.9 ± 13.8	12.2 ± 0.8
6	45.0 ± 6.7	45.4 ± 11.1	10.1 ± 0.7
7	4.0 ± 2.0	6.1 ± 3.5	5.9 ± 0.6
8	3.0 ± 1.7	5.4 ± 4.1	5.7 ± 0.6

Table 7.2: Development of data, background and signal under cuts. The background contains the QCD multijet estimation and the Monte Carlo samples for $Z+$jets, $W+$jets, Diboson and $t\bar{t}$, where the Z sample has been scaled to the charge flip prediction. Sel. 1 to 8 refers to the sequence of cuts as introduced in Tab. 7.1.

Sel.	QCD	$t\bar{t}$	Diboson	$W+$jets	$Z+$jets	Charge Flip
0	445.2 ± 22.8	1.1 ± 0.1	8.0 ± 0.4	87.1 ± 5.3	74.4 ± 6.6	109.6 ± 26.9
1	444.4 ± 22.8	0.9 ± 0.1	7.7 ± 0.4	86.8 ± 5.3	52.9 ± 6.0	73.7 ± 22.5
2	444.4 ± 22.8	0.9 ± 0.1	7.5 ± 0.4	86.8 ± 5.3	52.8 ± 6.0	75.3 ± 22.5
3	128.2 ± 14.1	0.9 ± 0.1	6.7 ± 0.4	78.7 ± 5.1	35.2 ± 5.0	60.9 ± 17.3
4	67.5 ± 13.0	0.7 ± 0.1	6.2 ± 0.4	74.9 ± 5.0	29.6 ± 4.7	48.1 ± 15.7
5	24.1 ± 10.6	0.0 ± 0.0	2.3 ± 0.2	38.5 ± 3.8	8.2 ± 2.6	14.8 ± 8.0
6	6.3 ± 8.2	0.0 ± 0.0	2.0 ± 0.2	32.8 ± 3.6	6.5 ± 2.5	4.3 ± 6.5
7	0.0 ± 0.8	0.0 ± 0.0	1.2 ± 0.2	4.9 ± 1.6	1.3 ± 1.0	0.0 ± 3.1
8	0.0 ± 0.8	0.0 ± 0.0	1.2 ± 0.1	4.3 ± 1.5	0.4 ± 0.3	0.0 ± 3.7

Table 7.3: Composition of the background after each cut, and estimation of the charge flip content in data. The Z+jets distribution is scaled to the number of charge flip events. Sel. 1 to 8 refers to the sequence of cuts as introduced in Tab. 7.1.

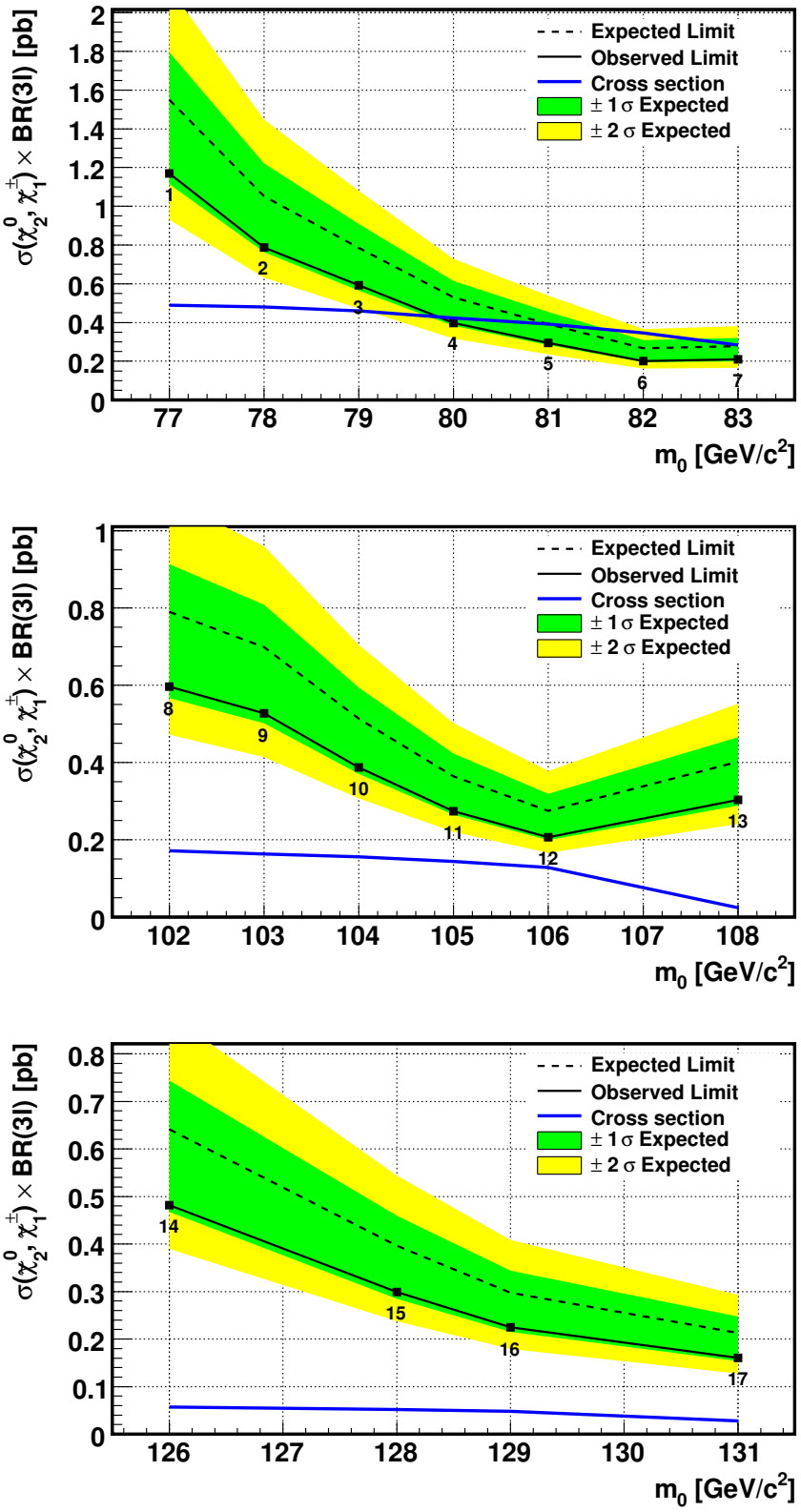

Figure 7.1: Expected and observed limits (cross section times branching ratio) as a function of m_0. The inset numbers refer to the SUSY points as defined in Tab. 5.2. Note that the points are at different values of $m_{1/2}$.

Source	Uncertainty
Luminosity	6%
Jet energy scale	1%
Muon ID and track matching	3%
QCD multijet estimation (Sec. 6.1.2)	6%
Electroweak subtraction (Sec. 6.1.4)	9%
Charge flip estimation (Sec. 6.2.1)	2%
PDF uncertainty	4%
W+jets cross section	6.7%
Diboson cross section	1.6%

Table 7.4: List of systematic uncertainties considered in limit calculation.

Pt.	m_0 [GeV]	$m_{1/2}$ [GeV]	$\sigma \times BR$ [pb]	Exp. [$\sigma \times BR$]	Obs. [$\sigma \times BR$]
1	77	183	0.4891	3.17	2.39
2	78	182	0.4800	2.19	1.64
3	79	181	0.4590	1.71	1.29
4	80	180	0.4232	1.25	0.94
5	81	180	0.3917	1.00	0.75
6	82	179	0.3458	0.77	0.58
7	83	178	0.2826	0.98	0.74
8	102	211	0.1714	4.61	3.48
9	103	210	0.1637	4.27	3.22
10	104	210	0.1556	3.30	2.49
11	105	209	0.1441	2.53	1.90
12	106	208	0.1283	2.14	1.61
13	108	206	0.0245	16.41	12.38
14	126	240	0.0567	11.31	8.50
15	128	239	0.0517	7.67	5.79
16	129	238	0.0482	6.17	4.66
17	131	236	0.0277	7.69	5.78

Table 7.5: Determined expected and observed limits in units of cross section times branching ratio. Cross sections above the stated observed limits are excluded at 95% CL. The points listed are the SUSY points as defined in Tab. 5.2.

Cut 0: $p_{T1} > 15$ GeV and $p_{T2} > 10$ GeV

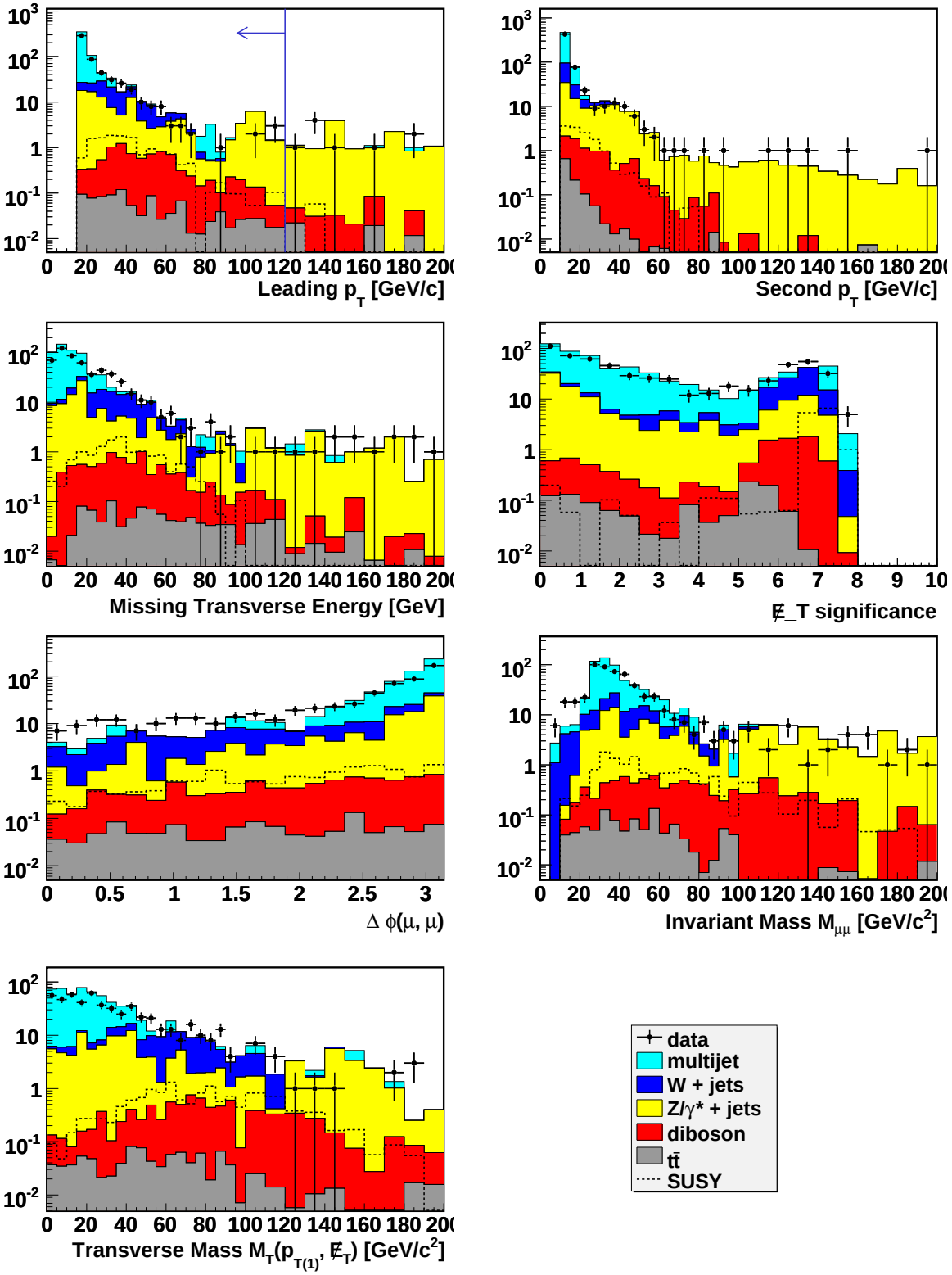

Cut 1: $p_{T1} < 120$ GeV

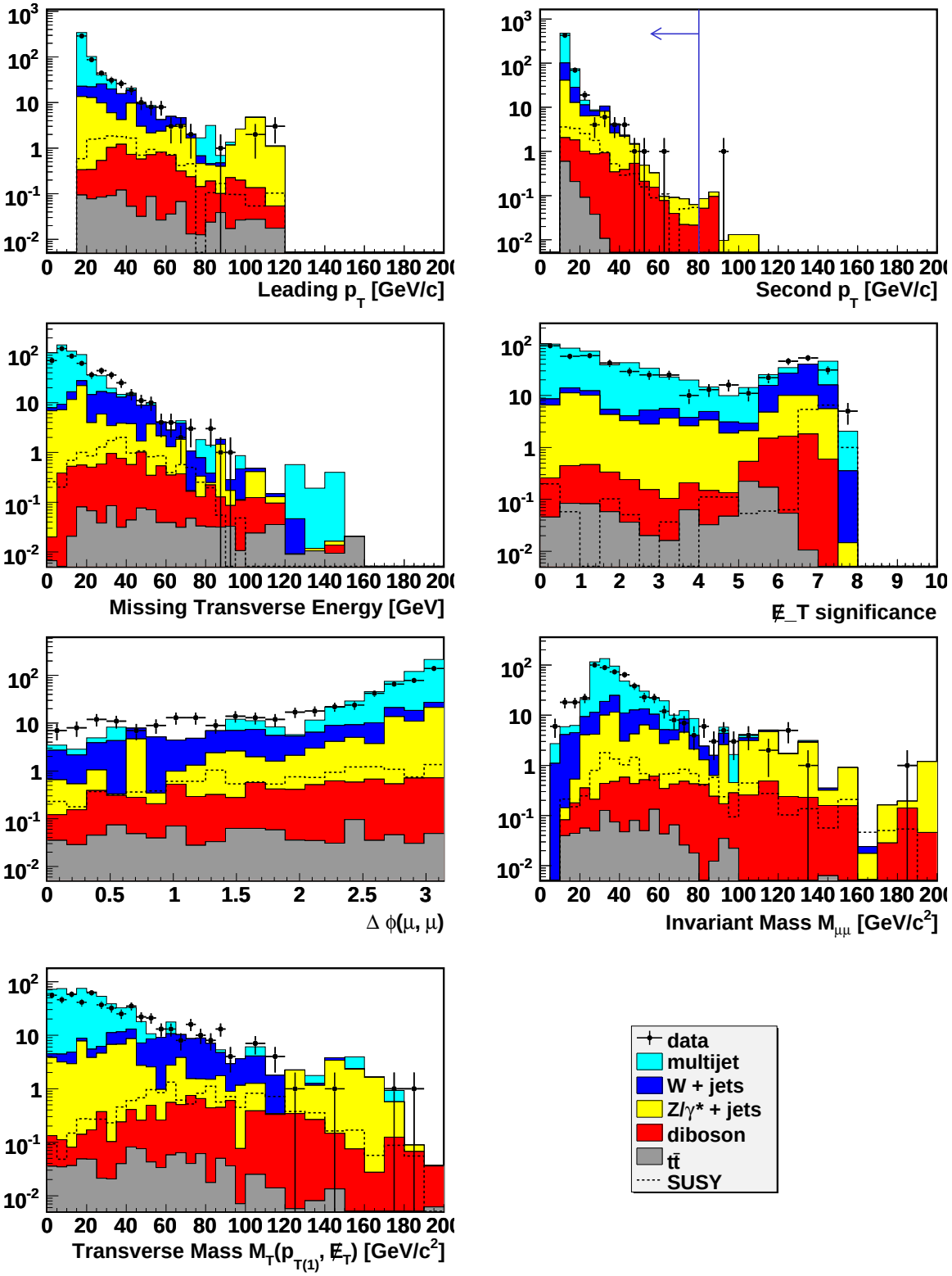

Cut 2: $p_{T2} < 80$ GeV

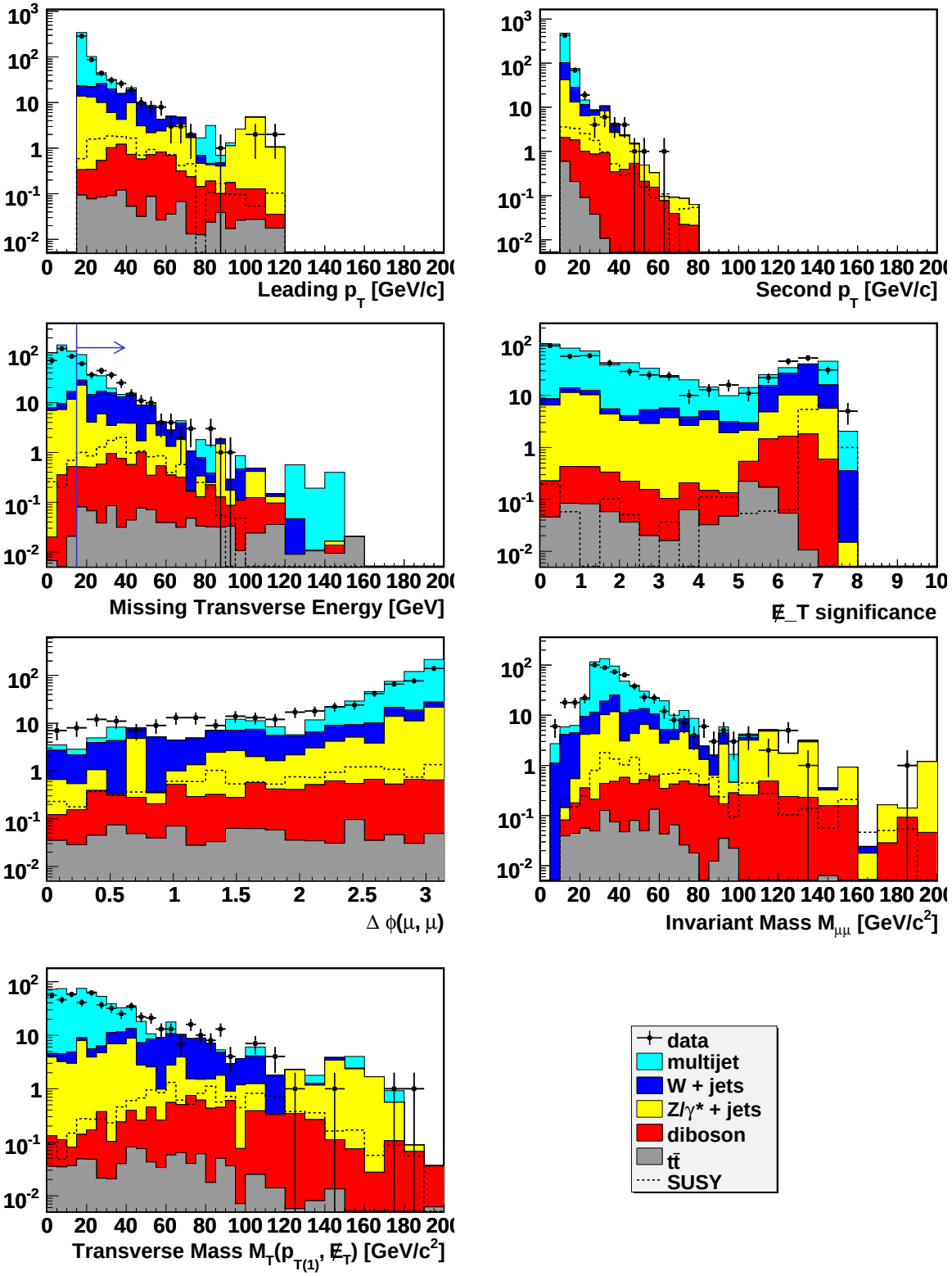

Cut 3: $\not\!\!E_T > 15$ GeV

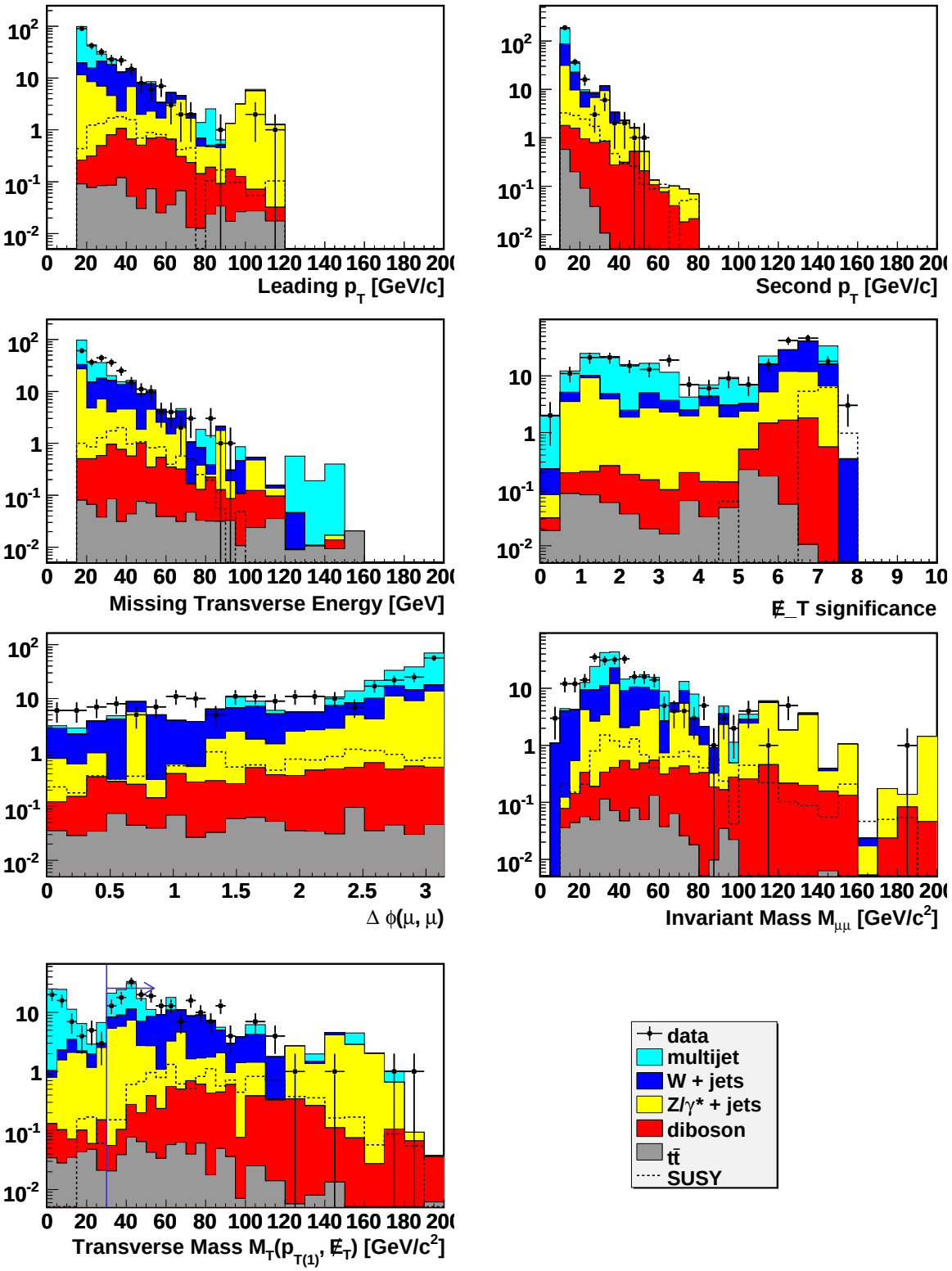

Cut 4: $M_{T1} > 30$ GeV

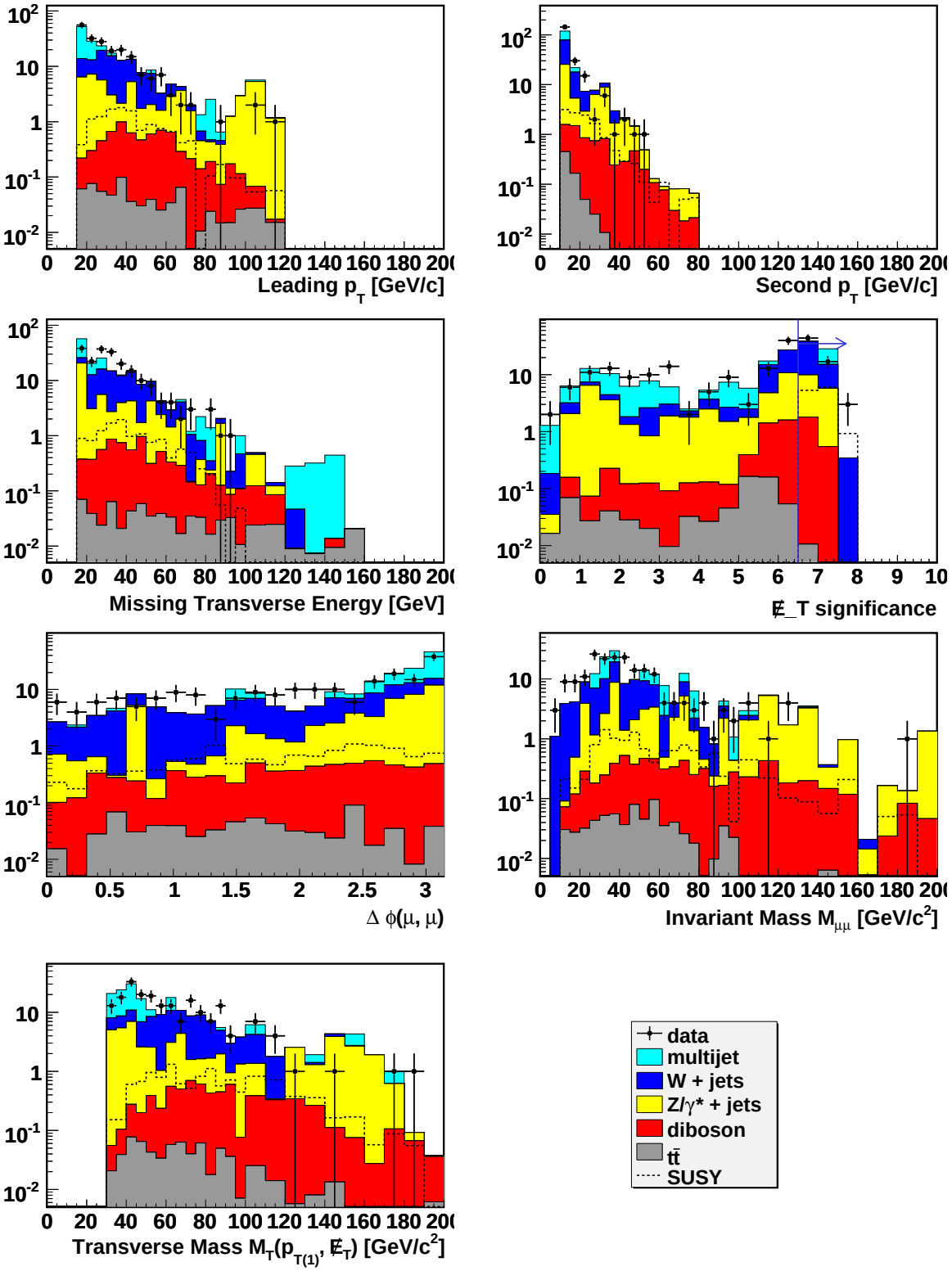

Cut 5: Sig($\not\!\!E_T$) > 6.5 GeV

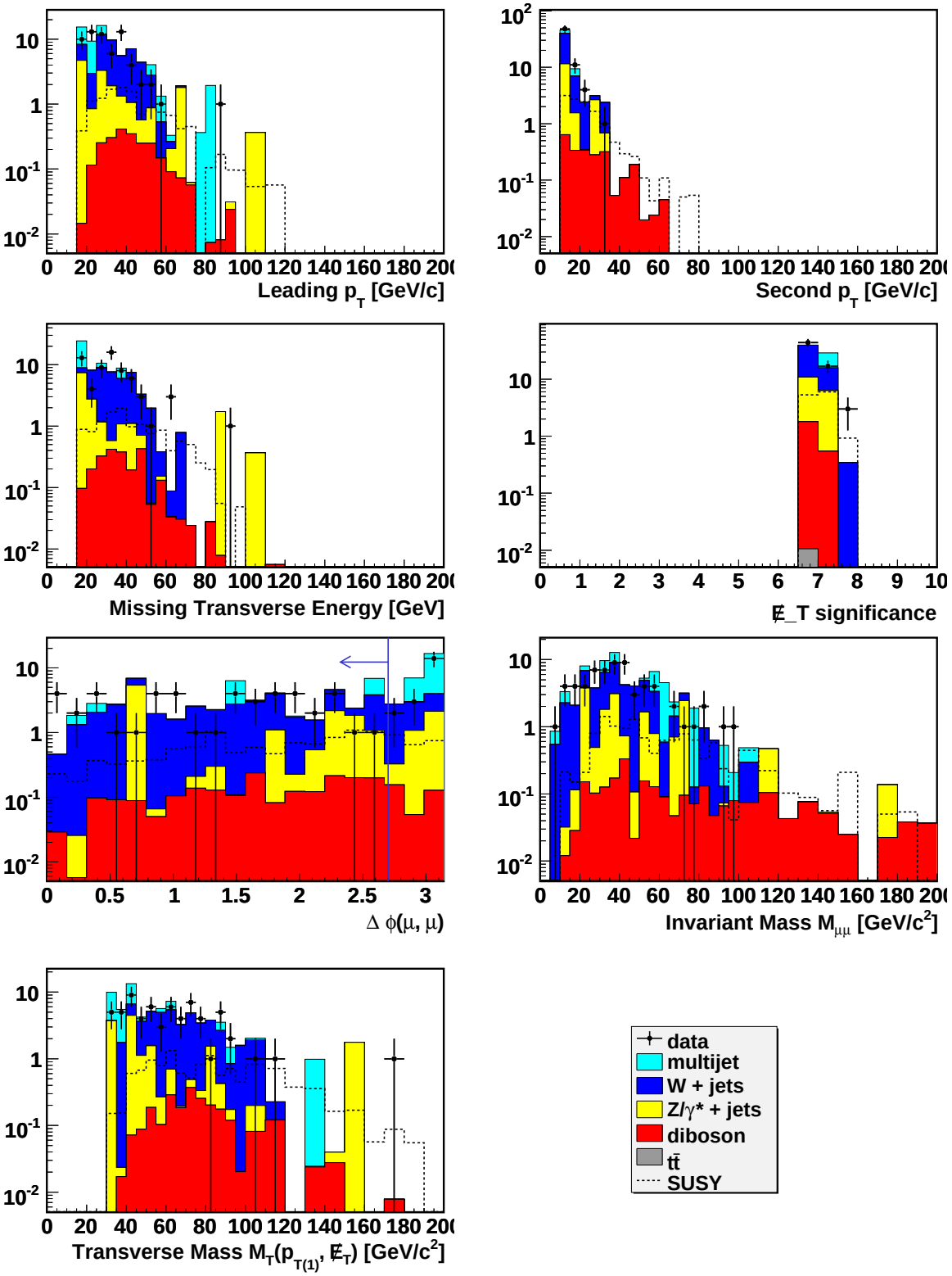

Cut 6: $\Delta\varphi < 2.7$ GeV

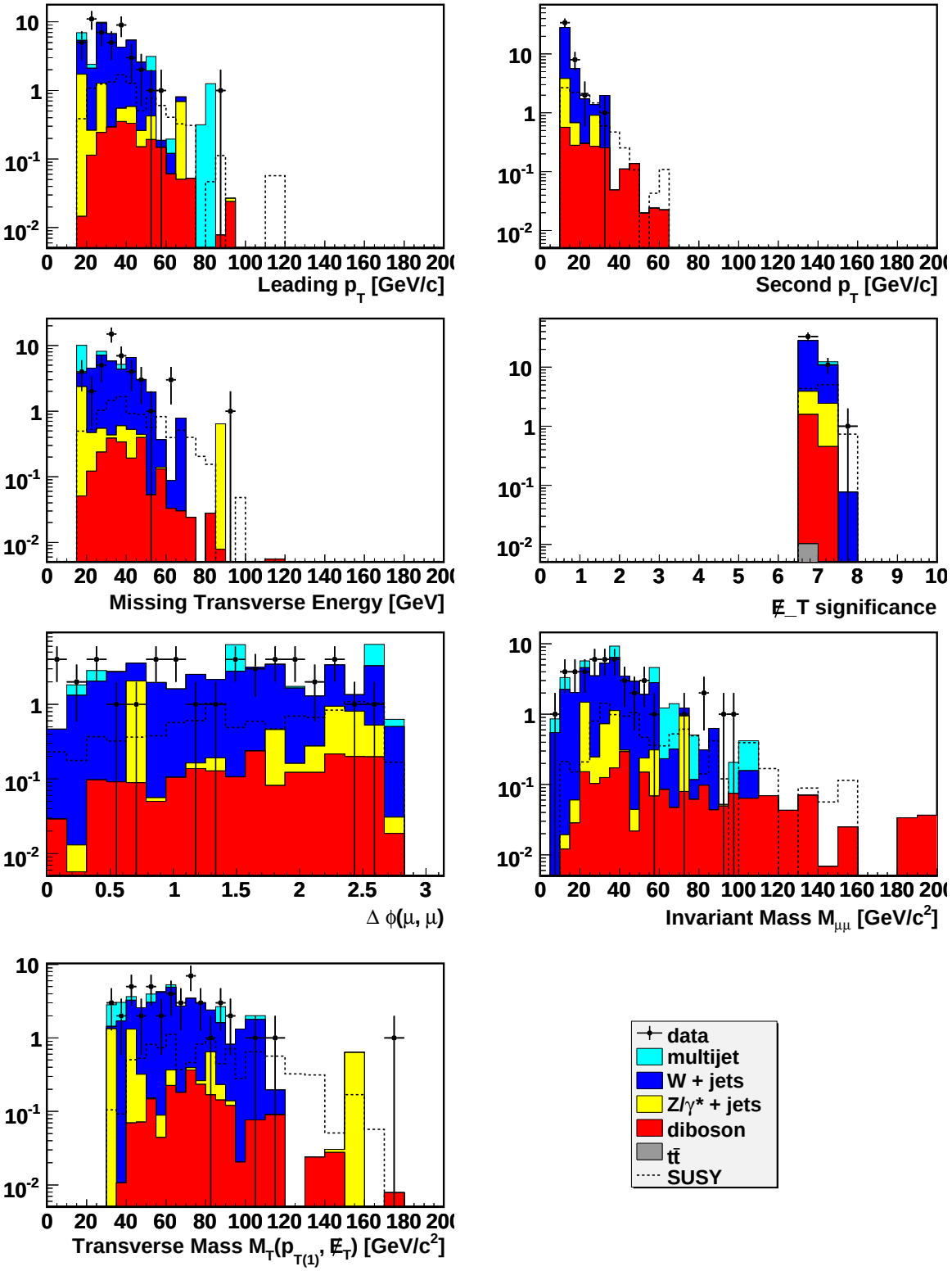

Cut 7: $\not\!\!E_T \times p_{T2} > 700$ GeV

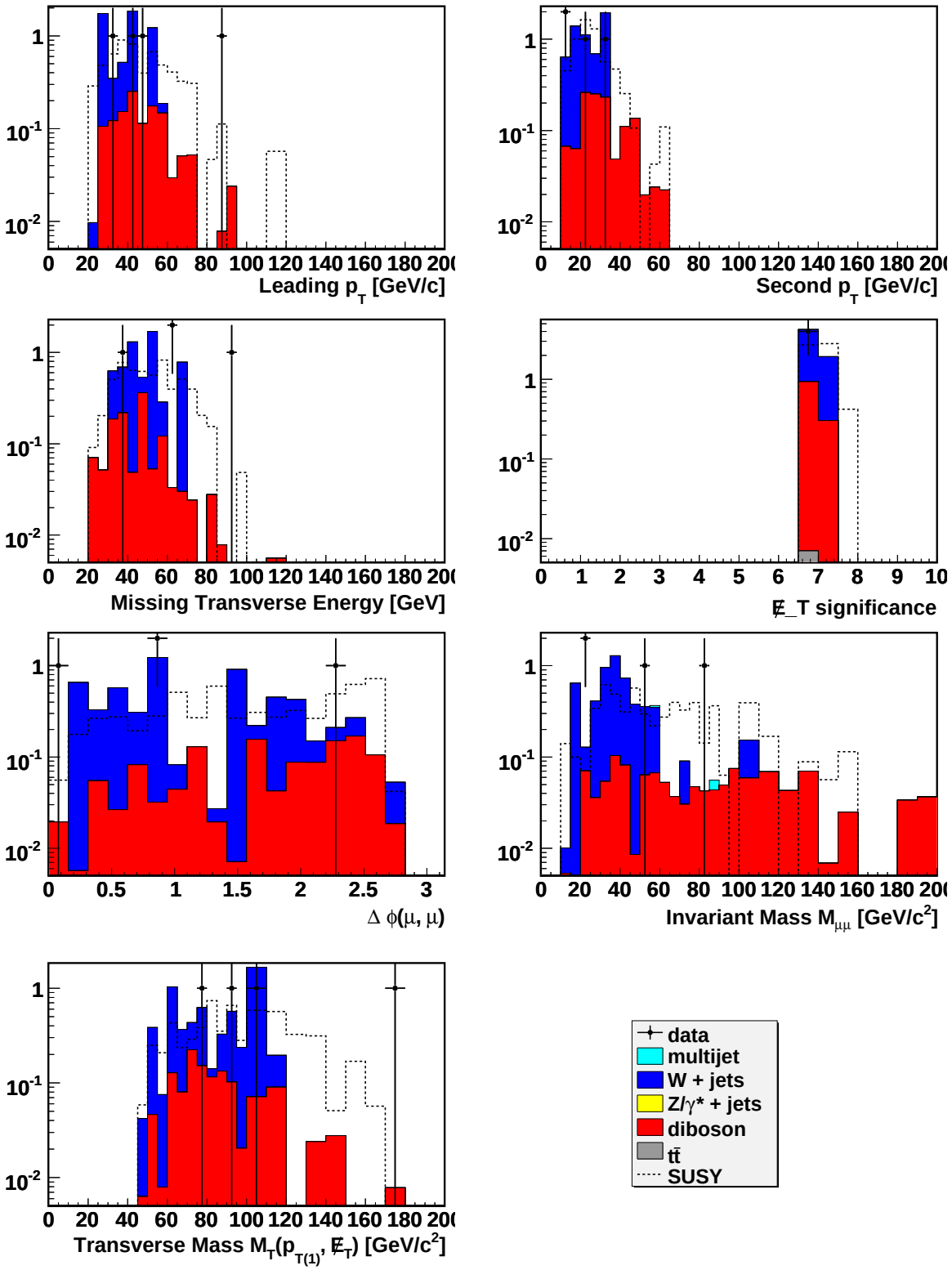

Cut 8: $M_{T2} < 85$ GeV

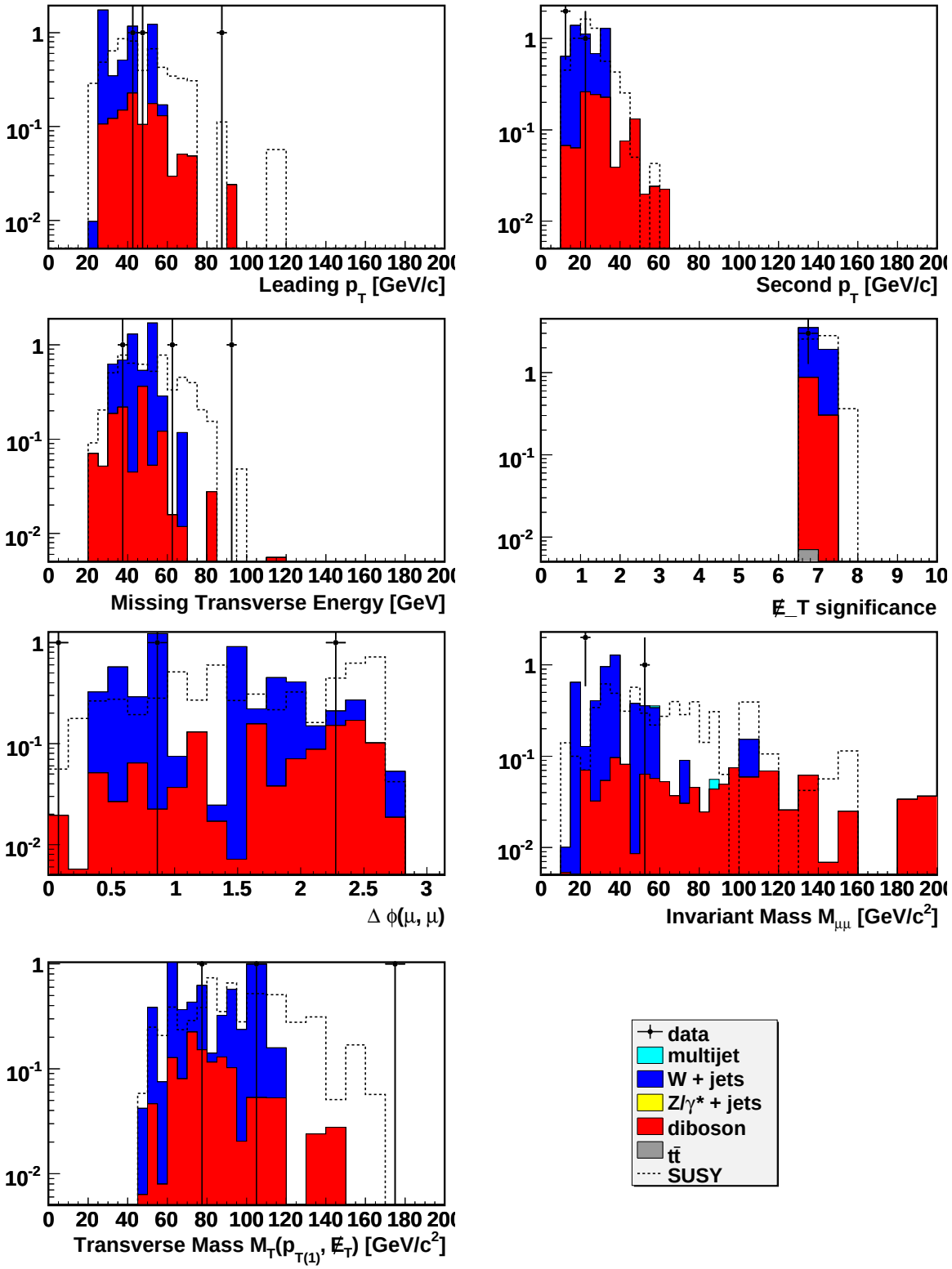

8 Summary & Outlook

This thesis presented a search for supersymmetry in the mSUGRA breaking scenario in the likesign dimuon channel at the DØ experiment. A focus was put on the analysis of the instrumental backgrounds, and the development of methods to improve their estimation. An advanced method for modelling the QCD multijet background by reweighting a QCD enriched sample was developed. Furthermore, a technique for estimating the background from charge mismeasurement in opposite-sign events was described.

The presented methods were applied to a part of the Run2b dataset, corresponding to 4.3 fb^{-1}. After event selection, 3 events were found in data with a background of $5.4 \pm 4.1(\text{stat}) \pm 0.7(\text{syst})$. Since no excess of data was seen, limits on the cross section were set, which improve upon the previously published results [9]. In particular, the SUSY points 4-7, as given by Tab. 5.2, were excluded at 95% CL. These points correspond to values of (m_0, $m_{1/2}$) of (80 GeV, 180 GeV), (81 GeV, 180 GeV), (82 GeV, 179 GeV) and (83 GeV, 178 GeV), respectively; all at $A_0 = 0$, $\tan\beta = 3$ and $\mu > 0$.

In the following, options for further improvements are discussed.

- Since the sensitivity is mainly statistically limited, the addition of more data is likely to lower the limits. A similar analysis is ongoing which includes the Run2a dataset, and uses a total integrated luminosity of 5.3 fb^{-1}. As more luminosity becomes available, points at higher m_0 and $m_{1/2}$ may be excluded.
- The set of cuts applied has not been optimized to achieve the best possible limits. A more optimized selection might improve the results.
- The use of multivariate methods is currently being investigated as an option to increase the sensitivity.
- The result may also be interpreted in the Unified Extra Dimensions (UED) model, which has very similar final states compared to mSUGRA.
- Finally, with the recent advent of the LHC, it will soon be possible to go to even higher sparticle masses and more remote regions of the parameter space, and to make exclusions — or to find evidence for supersymmetry.

Acknowledgements

This thesis wouldn't have been possible without the help of so many people. I'd like to thank Arnulf Quadt and Dimitri Denisov for giving me the opportunity to go to Fermilab, and my advisor Carsten Hensel for his efforts and advice. Furthermore, I'd like to thank Andrey Shchukin, Pedro Mercadante, Ângelo Santos and Alexey Popov for the good collaboration and their contributions, as well as Arnaud Duperrin and Stefan Söldner-Remboldt for their support. I'd like to thank Björn Penning and Yvonne Peters for helping me get started, and for allways having an open ear for my physics and other issues. I owe Oleg Brandt my thanks for his advice and his debugging skills when my selection didn't select what it was supposed to. I thank Leo Bellantoni and Maiko Takahasi for their ideas regarding the charge flip background, and for their patience when I came with questions. Then, I'd like to thank my family for allways supporting and believing in me, and Frauke for her emotional support during the whole time. Last, but not least, I say thank you to all the new friends I met during my stay at Fermilab for making this a really great year.

List of Figures

Bibliography

[1] The DØ Collaboration, V. M. Abazov *et al.*, *Evidence for an anomalous like-sign dimuon charge asymmetry*, hep-ex/1005.2757.

[2] F. Halzen and A. D. Martin, *Quarks and Leptons*, Wiley.

[3] R. Davis, D. S. Harmer, and K. C. Hoffman, *Search for Neutrinos from the Sun*, Phys. Rev. Lett. **20(21)** (May 1968) 1205.

[4] The LSND Collaboration, A. Aguilar *et al.*, *Evidence for neutrino oscillations from the observation of anti-nu/e appearance in a anti-nu/mu beam*, Phys. Rev. **D64** (2001) 112007, hep-ex/0104049.

[5] The Particle Data Group Collaboration, C. Amsler *et al.*, *Review of particle physics*, Phys. Lett. **B667** (2008) 1.

[6] D. I. Kazakov, *Beyond the standard model (in search of supersymmetry)*, hep-ph/0012288.

[7] S. P. Martin, *A Supersymmetry Primer*, hep-ph/9709356.

[8] W. Beenakker *et al.*, *The Production of charginos / neutralinos and sleptons at hadron colliders*, Phys. Rev. Lett. **83** (1999) 3780, hep-ph/9906298.

[9] The D0 Collaboration, V. M. Abazov *et al.*, *Search for associated production of charginos and neutralinos in the trilepton final state using 2.3 fb-1 of data*, Phys. Lett. **B680** (2009) 34, hep-ex/0901.0646.

[10] D. E. Johnson, *Instrumentation Requirements for the Fermilab Main Injector*, Beams-doc 77 v1, Fermilab, (November 2002).

[11] Fermilab Beams Division, *Run II Handbook*, Fermilab Beams Division RunII Webpage, http://www-bd.fnal.gov/lug/.

[12] D. P. McGinnis, *FNAL Tevatron operational status*, Prepared for Particle Accelerator Conference (PAC 05), Knoxville, Tennessee, 16-20 May 2005.

[13] The DØ Collaboration, V. M. Abazov *et al.*, *The Upgraded DØ Detector*, Nucl. Instrum. Meth. **A565** (2006) 463, physics/0507191.

[14] K. Hanagaki, *DØ Layer 0—innermost layer of Silicon Microstrip Tracker*, Nucl. Instrum. Meth. **A569** (2006) 8.

[15] M. Tuts *et al.*, *The D0 Upgrade*, Submitted to the PAC, available at http://www-d0.fnal.gov/hardware/upgrade/pac0495/d0toc.html.

[16] The DØ Collaboration, S. Abachi *et al.*, *Beam tests of the DØ uranium liquid argon end calorimeters*, Nucl. Instrum. Meth. **A324** (1993) 53.

[17] A. Khanov, *HTF: histogramming method for finding tracks. The algorithm description.*, DØ-Note 3778.

[18] P. Hough, *Machine Analysis of Bubble Chamber Pictures*, in: *Proc. Int. Conf. High Energy Accelerators and Instrumentation*, (1959), 1959 .

[19] D. Adams, *Finding Tracks*, DØ-Note 2958.

[20] G. Hesketh, *Central Track Extrapolation Through the DØ Detector*, DØ-Note 4079.

[21] K. Kleinknecht, *Detektoren für Teilchenstrahlung*, Teubner Studienbücher, Teubner, Stuttgart, (1984).

[22] S. Cho *et al.*, *Muon ID Certification for p20 data*, DØ-Note 5824.

[23] G. H. for the DØ Muon Algorithm and I. groups groups groups groups, *Content of the p17 Muon Thumbnail*, DØ-Note 4735.

[24] A. Kumar *et al.*, *Electron Likelihood Study*, DØ-Note 4769.

[25] J. Hays *et al.*, *Single Electron Efficiencies in p17 Data and Monte-Carlo Using d0correct from Release p18.05.00*, DØ-Note 5105.

[26] G. C. Blazey *et al.*, *Run II jet physics*, `hep-ex/0005012`.

[27] J. Hegeman, *Jet energy scale calibration in the D0 experiment*, Journal of Physics: Conference Series **160(1)** (2009) 012024.

[28] L. Bellantoni, A. Khanov, and M. Takahashi, *Search for Associated Higgs Boson Production* $WH \to WWW^* \to \ell^{\pm}\nu\,\ell'^{\pm}\nu' + X$ *in* $p\bar{p}$ *Collisions at* $\sqrt{s} = 1.96$ TeV, DØ-Note 5719.